Characterization of the disk and line-profile variability of the Be star π Aquarii

David Alfonso Enrique Concha Astorga

Supervisor: Dr. Catalina Arcos (UV)
Internal reviewer: Dr. Michel Curé (UV)
External reviewer: Dr. Yanina Cochetti (UNLP)

Tesis para optar al grado de Magíster en Astrofísica
Instituto de Física y Astronomía
Facultad de Ciencias
Universidad de Valparaíso

March,2023
Valparaíso, Chile.

’ In memory of my grandfather and grandmother Angel & Olivia. ’

Esta dedicación es para toda persona que de alguna forma me acompaño durante mi camino, familia, mi pareja Carla, mis amigos en el Magíster.

This thesis is solely my own composition,

except where specifically indicated in the text.

David Concha
March 2023.
Valparaíso. Chile.

Acknowledgements

During this path in my career, I had a wonderful experience working with the group of Massive stars at the Universidad de Valparaíso, especially working under the supervision of my professor Dr. Catalina Arcos, who motivated me every step of this project, who always support me in everything I needed and I will always be grateful to her for all the teaching and for being a great person. I want to thank Dr. Michel Curé for his support since day one in my master's and for his jokes that brightened my day and Dr. Yanina Cochetti for her valuable comments that helped me to improve this thesis.

I want to thank my parents, whom I love very much, Erika and Adolfo, without them, I would not be the person and scientist I am now. They always support me during my Bachelor's and in my Master's. Also, to my beloved girlfriend Carla, who accompanied me every day, supporting me from day one, giving me motivation and extra love to finish my career; I love you; And to my puppy, Pandorita, who came into my life the day I started my master's degree and accompanied me in the cold mornings of online classes, giving me joy these two years. Finally, I want to thank Daniela Turis for her patience and collaboration in running models and explaining all the details about `ZPEKTR` code to me.

This thesis has financial support from FONDECYT 11190945. I thank project FAPESP Nº133541 and the Beca Adelina Gutierrez of SOCHIAS. This work used BeSOS Catalogue, operated by the Instituto de Física y Astronomía, Universidad de Valparaíso, Chile: http://besos.ifa.uv.cl and funded by Fondecyt iniciación 11130702. The page is maintained thanks to FONDECYT 11190945. This work has used the BeSS database, operated at LESIA, Observatoire de Meudon, France: http://basebe.obspm.fr. This work has been possible thanks to the use of AWS-U.Chile-NLHPC credits. Powered@NLHPC: This research was partially supported by the supercomputing infrastructure of the NLHPC (ECM-02).

Abstract

Massive stars have masses roughly greater than 8 $M_{\odot}$ and temperatures bigger than 10000 K, with a luminosity of $10^4 - 10^5 L_{\odot}$. These stars are very important because they end their lives with core-collapse events as supernovae, enriching the interstellar medium, that activates the formation of new stars. They are also important to study stellar and galaxy evolution, the multiplicity and rotation of stars, and the effects of the magnetic field on stars. They can provide studies of evolution at various redshifts and metallicities covering the vast cosmic history, etc. Classical Be stars have thin circumstellar disks at the stellar equator with a flaring shape, confirmed by spectroscopic and interferometric observations. They are rapidly rotating B-type stars, expelling material from their photosphere under a process that to date is not fully understood. Their disks rotate in a quasi-Keplerian motion. They can be detected via Hydrogen lines in emission and infrared excess in the spectral energy distribution, which is attributed to the presence of ionized gas. Several mechanisms are proposed to explain how the material is placed from the star to the disk with these mentioned characteristics. Some possibilities are binarity, rapid rotation, non-radial pulsation, winds, or a combination of these mechanisms.

The main purpose of this thesis is to add new knowledge of Be stars, with a characterization of the variable Be star named π Aquarii. It's a bright, rapidly rotating classical Be star observed more than 100 years, presenting mid- and long-term variability over 50 years in the profile of Hα and Hγ. This star is in a binary system, and over the years, the disk has been active and quiet with respect to the formation and dissipation of the disk. We use spectroscopic data recollected from the BeSS and BeSOS databases to obtain different measurements on the spectral lines. We studied the disk parameters in five phases over the course of 21 years with a 3D NLTE Montecarlo transfer radiative code-named `HDUST`.

The parameters of the disk for the first three phases with low uncertainty, where

for the first, second, four, and fifth phases the range of inclination is between 50-70°, but for the third phase the inclination is lower, around 25-45° which can be the reason for the sudden apparition of FeII emission lines. Some Helium and other lines are also in emission, in different epochs of the star. We were able to confirm the phase-locked V/R variation of 81.14 days, which is the period of the binary star found in the literature.

The method applied in this thesis can help analyze this kind of shape profile, usually observed in Be stars. These results and discussion contribute to the knowledge of the variability observed in Be disks and the connection with the companion.

Contents

CHAPTER 1

Introduction

1.1 Context

It was believed until the 1920s that our galaxy was the only one in the universe that contained all the astronomical objects known to date but after the Great Debate between Harlow Shapley and Heber Doust Curtis (Shapley & Curtis, 1921), and with the confirmation that Andromeda was not within the Milky Way thanks to observations of Cepheid variable stars made by Edwin Hubble, that finally, we were able to confront the reality, that our galaxy was "one in a million".

The Milky Way is a large spiral system composed of 10^{12} stars, planets, dust, gas, etc. One of the many types of stars that exist in our galaxy are massive stars, quite peculiar stars that determine the shape of the arms of our galaxy (Urquhart et al., 2014) among other things; for instance, they end up their life in a supernova explosion or gamma-ray burst, that are unique superb events in the universe, the outer layers are extremely hot and emit photons sufficiently energetic to heat-up, ionize, or trigger chemical reactions in the interstellar medium. Another important reason is that core-collapse supernovae explosions enrich the interstellar medium, yielding in it materials produced in its core and further process elements during their final blast, activating new periods of star formation (Oey & Massey, 1995).

Most stars are in hydrostatic equilibrium, where the relation between the stellar mass, M, and the stellar luminosity, L, is well studied with the following relationship of $L \propto M^{\alpha}$, where α is between 1 and 3 (Kippenhahn & Weigert, 1990). The lifetime of a star, τ, depends on both quantities, and it is defined as a function of M, e.g., $\tau \propto M^{\alpha-1}$. This implies that the more massive an object is, its lifetime is much shorter, compared to the Sun. In more than 90 percent of their total life, the star produces energy by thermonuclear burning hydrogen to helium in their centers in a CNO cycle in which four protons are converted to one helium nucleus.

Massive stars correspond to the O, B, and A spectral types in the Harvard Spectral Classification. They have masses roughly greater than 8 $M_{\odot}$ and temperatures bigger than 10000 K, with a luminosity of $10^4 - 10^5 L_{\odot}$. Their location in the Hertzsprung-Russell diagram (hereafter HR) is on the Main Sequence (MS) or above, as is shown in Fig. 1.1 where they evolve off the MS to lower effective temperature, and this occurs around constant luminosity, as seen in the horizontal shift to the right to the red supergiant region in the figure (Vink, 2000).

1.2 Classical Be stars

Classical Be stars (hereafter CBe) are massive (or not) main sequence B-type stars. They are fast rotators expelling material from their photosphere under a process still not fully understood. The material is placed in a thin equatorial disk in quasi-Keplerian rotation (Meilland et al., 2007), and the disk growing is governed by viscosity (Lee et al., 1991). The first observation of a Be star was made by Secchi (1866) of the Be star γ Cas (B0.5 IV), where he observed the emission profile of Hβ.

Since the discovery of CBe, enormous work on developing new techniques to understand their distinctive characteristics have been made over the years, for instance, high angular interferometric observations of CBe (Quirrenbach et al., 1994, 1997), spectro-polarimetry observations (Wood et al., 1997), space-based photometry (Labadie-Bartz et al., 2022), long-term monitoring spectroscopic campaigns (Marr et al., 2021), among many others authors. (See review of Rivinius et al., 2013, for details). One of the most challenging tasks is to infer the stellar parameters of CBe due to disk interference, which changes the actual value of the parameters as they mask the central star and the rapid stellar rotation. The fraction of CBe in galaxies varies

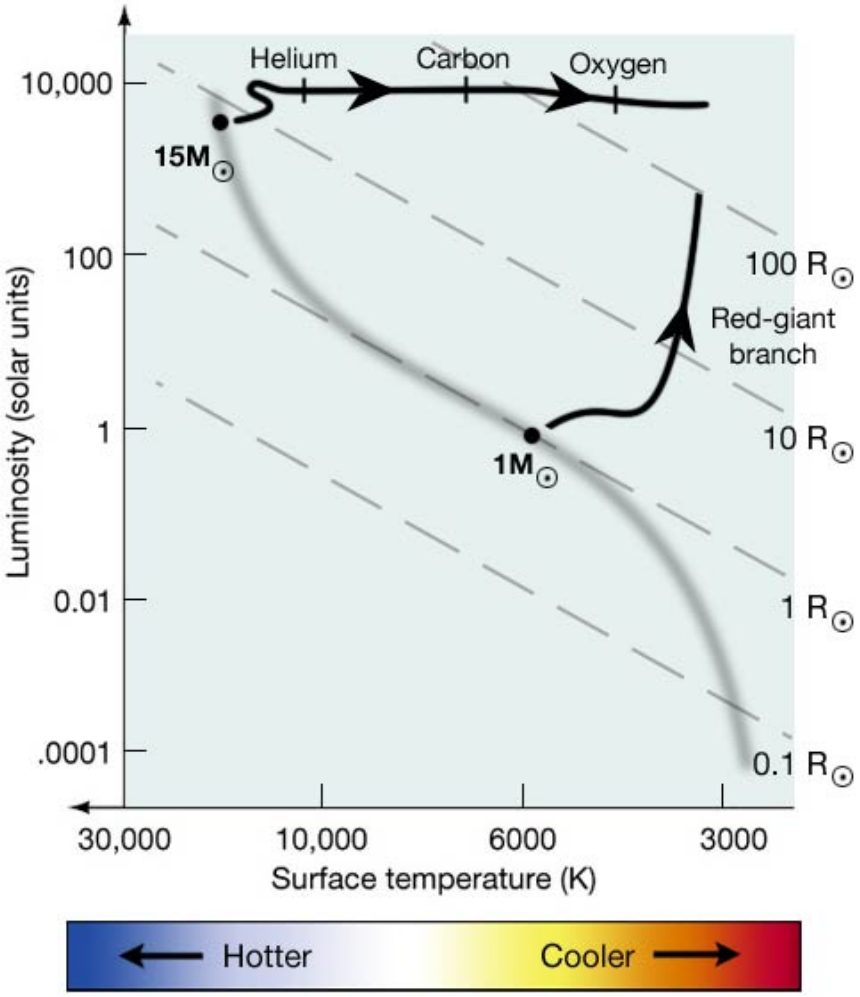

Figure 1.1: HR Diagram that compares the evolutionary track of an O star with a mass of 15 solar masses with a Sun-like star. Credit: Penn State Astronomy & Astrophysics

depending on the metallicity, age, and the distribution of the stellar rotation, ranging from 3 to 50 % (Zorec & Briot, 1997a; Wisniewski & Bjorkman, 2006; Bastian et al., 2017). If we look at our galaxy, the fraction of CBe from the total of MS B stars is around 10 % (Rivinius et al., 2013).

A way to detect and get information about CBe is with their Spectral Energy Distribution (hereafter SED), where the total flux emitted of the system star+disk is a contribution of free-free emission (Gehrz et al., 1974) and absorption process going on in the disk due to the photospheric radiation from the central star. This leads to the peculiar characteristic of IR and radio radiation excess concerning the

photospheric continuum that is observed in the SED (see Fig. 1.2). Waters et al. 1987 studied three different wavelengths of the spectrum, at 12, 25, and 60 μm using the Infrared Astronomical Satellite (IRAS). They found that the excess was due to the fully ionized material, not dust. They also introduce the power-law density model for the disk in the form $\rho \propto r^n$ for their observations. A correlation between the spectral type and the disk's magnitude in excess was caught. Early Be stars have denser disks as they have larger IR excess. It also occurs that the Hα emission and the polarization are larger, giving a sense that all the observables are related. Another feature of CBe is the decrease in the UV and Visible part of the spectrum depending on the system's inclination, which is the angle between the rotation axis of the star and the line of sight from the Earth (see Fig. 1.3).

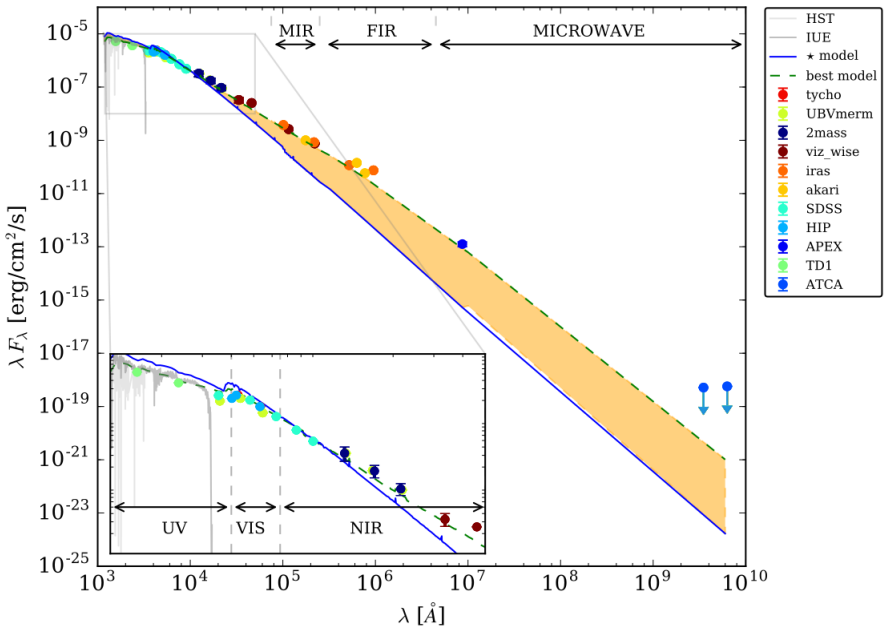

Figure 1.2: Full SED of α Arae. The solid blue line represents the best-fit model for the photosphere, whereas the dashed green line is the best fit for the system star+disk. The yellow shadow represents the IR and radio excess. Credits to Correia Mota 2019.

Information about the inner parts of the disk can be obtained in the IR range, where several hydrogen series are present: Paschen, Brackett, Pfund, and Humphreys

series. On the other hand, the optical range (Balmer series) gives information about the outer part of the disk. A recent study developed by Cochetti et al. (2022) of 22 Be stars studied in the IR part of the spectrum was done. J, H, K, and L bands were observed simultaneously using GNIRS and FIRE spectrographs. In addition, helium and metallic lines were also identified. They found that the FWHM of the Br10, Brδ, and Hu14 lines are correlated with $v \sin i$. Moreover, the separation between the peaks of the Br10 line correlates strongly with $v \sin i$, while the Hu14 line is more feeble. Hence, these lines are valuable to estimate the projected rotational velocity of Be stars. They analyzed the EW ratio between Brα and Brγ and the diagram of the flux ratio, having the following outcome, new criteria to categorize Be stars into Mennickent's groups (see Mennickent et al. (2009) for more details). Final results show that some lines are related to the spectral type of Be stars. HeI lines are observed in early B-type, where Mg II and OI are in emission, furthermore, the OI 3168 Å emission line falls off for late B-type stars.

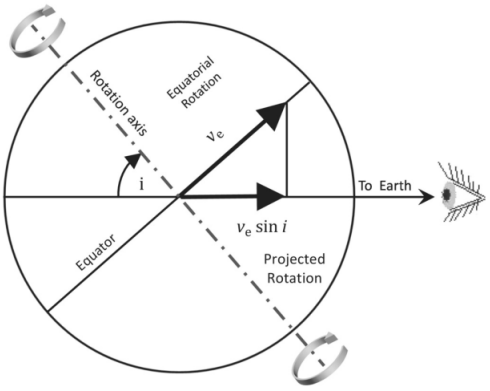

Figure 1.3: Projected rotation velocity of the surface where $v_e \sin i = v \sin i$ for this work. Credits to Trypsteen & Walker (2017).

Besides the SED detection of CBe, intrinsic linear polarization is another characteristic of these stars. This is produced when radiation from the central star is scattered by the ionized gas disk perpendicular to the plane of the disk and can be measured without the problem of dust extinction. In CBes, up to 2% of the radiation in the visible domain is mainly observed to be intrinsically linearly polarized via Thomson scattering. The fact that the polarization is non-zero is a piece of evidence that the circumstellar envelope has a non-spherical shape and instead has a flattened

envelope. The level of polarization and the spectral shape depend on the density of the disk. In Fig. 1.4, a comparison of two regions, a tenuous and a dense disk, is observed. In the vertical axis is the optical depth of the main sources of opacity and the degree of polarization. In the horizontal axis is the wavelength. The observed level of polarization is strongly dependent on the system inclination. For disks seen pole-on, the observed level of polarization will be zero, as the scattering planes are distributed uniformly. The polarization will rise with increasing inclination but attains a maximum at an inclination of 70–80° rather than when observed exactly edge-on.

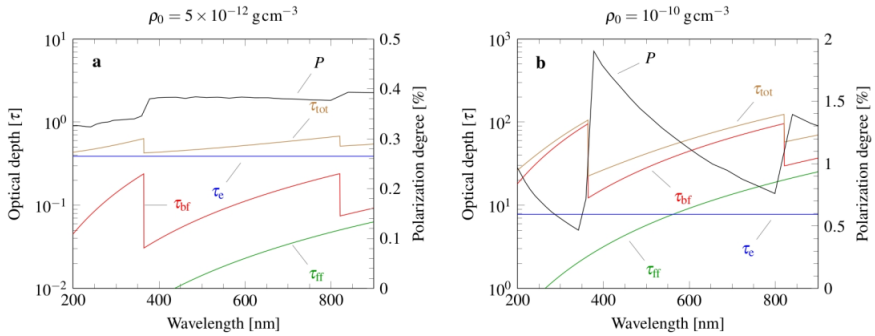

Figure 1.4: Polarized spectrum of two disk densities at 70° of inclination. *left panel:* case for the tenuous disk where the Thomson scattering opacity dominates over the hydrogen opacities. The polarized spectrum is mostly gray, and the polarization level is low. *right panel:* dense gas disk, where the bound-free and free-free opacities prevail over the gray Thomson opacity and, therefore, the polarized spectrum attains a characteristic shape with the spectral slope being negative in the Paschen continuum. Image taken from (Rivinius et al., 2013)

1.3 Variability

A striking fact of CBes is that they present high variability on many timescales ranging from a few minutes to decades. Some come from the star, and others are from the decretion gas disk. Short-term variability is caused by non-radial pulsation (hereafter NRP, Baade et al. (2016); Labadie-Bartz et al. (2020)) that is very common in Be stars. They pulsate primarily in low-order g-modes, where gravity is the restoring force, but also pulsation can be found at large frequencies, driven by p-modes. An example of short-term variability due to a short-lived event of mass ejection is seen in

Fig. 1.5, where between the day 1715 and 1735, the star passes from a disk-less phase (turquoise color) to a formation phase (orange color). See more detail in section 2.1.2

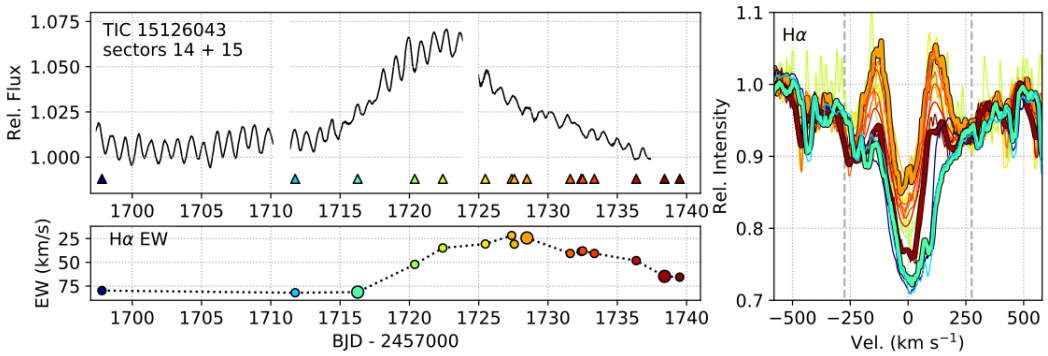

Figure 1.5: A typical flicker of the B3II Be star HD 194779 observed with the TESS program. The top panel is the TESS light curve. The bottom panel shows the EW of the Hα line, and the right panel highlights the evolution of Hα in time, with each color representing the spectroscopic epoch. Credits to Labadie-Bartz et al. 2020

Mid-term variability in CBe is the next in time scale. This is observed in the Violet to Red (hereafter V/R) peak ratio variations, which can be noted in Fig. 1.6. This measurement is the ratio between the heights of the violet and the red component of the double-peaked emission line. These asymmetries are due to over-densities in one part of the disk. They are well described by the one-armed global oscillation model (i.e., m = 1 modes with m equal to the azimuthal wavenumber.) (Okazaki, 1991a, 1997; Carciofi et al., 2009). Particles will tend to align in elliptical orbits leading to the over-density that rotates with the disk. In the work of Papaloizou et al. (1992a), they included the action of a gravitational field containing a quadrupole component to exemplify that elliptical particle presses under this force. Furthermore, Gayley et al. (2001) embraces the possibility of including the radiative force of optically thick lines inside the disk to explain the variability of the V/R ratio. Another possibility is that a binary companion causes these variations because V/R variations show a variation phase locked with the orbital period of the companion. Likely, careful accounting of tidal or/and heating effects from the secondary on the structure of a circumstellar disk can improve the understanding of this phenomenon.

Finally, long-term variability (years to decades) is related to the formation and dissipation of the disk, as well as phases of enhancement mass-loss rates. (Bjorkman

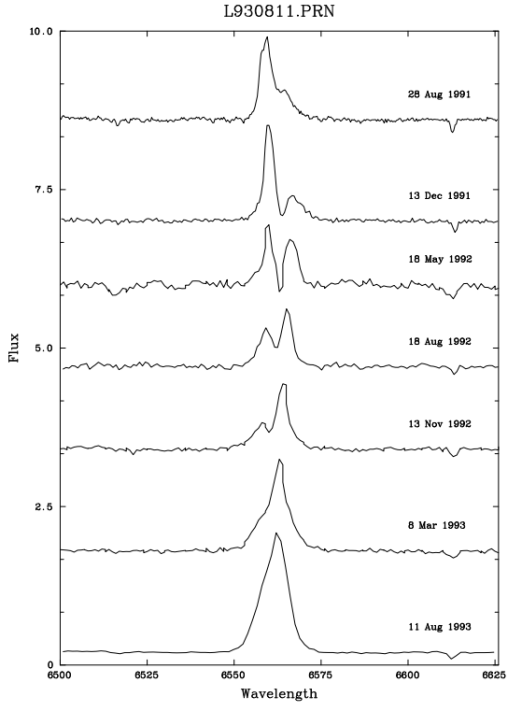

Figure 1.6: Evolution of the Hα profile observed in Be/X binary system LS I +61° 235. The flux is normalized to the continuum, and a constant offset is summed to every spectrum to create the figure. Credits to Reig et al. (1997)

et al., 2002; Rímulo et al., 2018). Fig. 1.7 shows the long-term monitoring of the Hα equivalent width (hereafter EW) of the 28 Tau star from 1953 to 2017, where a maximum in the EW is observed around 38000 and 51000 Modified Julian Days (hereafter MJD), indicating a change between an active and a disk-less phase.

1.3.1 Observables

By looking at the hydrogen lines, in particular, the Hα emission line, preliminary information about the inclination of the disk can be determined since the observed emission line's shape depends on the observer's inclination view. In Fig. 1.8, the observed spectra of Be stars seen under different inclination angles are shown: from close to the pole-on case (HD 5223) to close to the edge-on case (o Aquarii). We see how the morphology of the double-peaked emission lines changes as a function of the inclination angle. While from the A view, we observe a single-peaked Hα profile, from D, the Be-shell star o Aquarii shows a broadened double-peaked Hα profile due to the disk rotation with intense absorption in the core of the line.

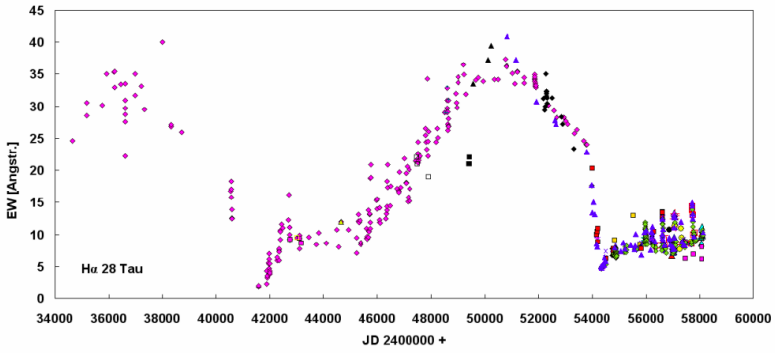

Figure 1.7: Evolution of the Hα EW observed in the binary system Pleione over 60 years. Credits to Pollmann (2018)

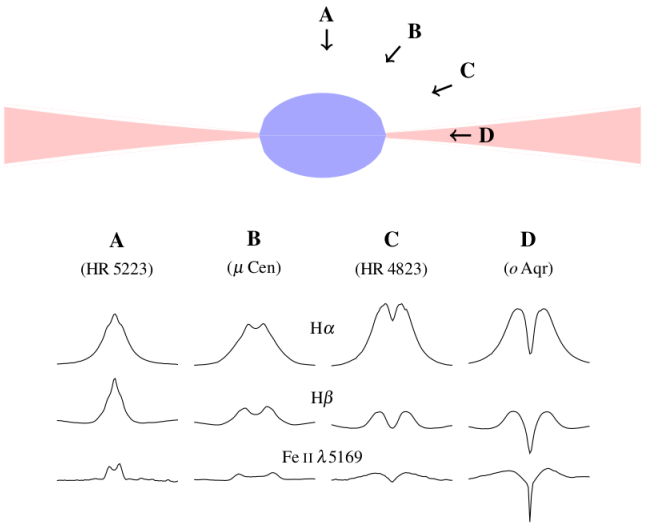

Figure 1.8: Shape of the emission-line for different inclination angles. This is known as Struve's model for Be Stars. Credits to Rivinius et al. (2013)

Several pieces of information can be obtained or inferred using high-resolution spectra. In particular, emission lines give information about the disk, while absorption lines come from the stellar photosphere. The most frequent measurements over the spectral line and their meaning are:

- **EW**: It is defined as:

$$EW = \int_{\lambda_1}^{\lambda_2} \left(1 - \frac{F_\lambda}{F_0}\right) \mathrm{d}\lambda, \tag{1.1}$$

where F_λ represents the flux at the range of interest, and F_0 is the continuum. For emission lines, as a consensus, the EW is negative. The intensity of the line gives us information about the size of the disk. The circumstellar envelope is larger as EW becomes greater (not considering the negative sign).

- **Violet to Red peak variations**: is defined as the ratio between the intensity of the violet and the red peaks of the emission line: $V/R = (I_v - I_c)/(I_r - I_c)$. This variation tells us about over-densities in the disk, which can be explained with one-armed global oscillation modes (Okazaki, 1991b; Papaloizou et al., 1992b) employing tidal forces from a binary companion.

- **Radial velocity**: The radial velocity can be measured using the Doppler effect, and it's related to the presence of a companion star.

- **Double-peak separation**: Hereafter DPS. Due to the Doppler motion of the disk, both violet and a red component of the emission line are observed. This gives us information about the disk rotation and where the lines are emitted.

1.4 Objectives

This thesis aims to study and characterize the behavior of the CBe star π Aquarii over the years and recognize how the active and passive phases of the disk are related to the central star. To accomplish the objective mentioned above, a set of specific objectives need to be fulfilled, which are the following:

- To collect optical observations from the known star catalogs for π Aquarii (BeSS and BeSOS).

- To recognize all the spectral lines present in the spectra.

- To perform the measurements on the line (EW, V/R, DPS, and RV), and apply them to Hα and spectral lines in the visible range where the total spectrum is available.

- To compute the V/R and RV variations period through the Lomb-Scargle periodogram.

- Derive new stellar parameters for π Aquarii using the ZPEKTR code.
- To find correlations between the variability of photospheric and metallic lines with the profile evolution of Hα.
- To study the disk parameters of π Aquarii, by using the 3D Monte Carlo radiative transfer code named HDUST .
- To create a small grid of HDUST models to compare with specific observation dates based on the change of the EW of Hα in time.

CHAPTER 2

Theoretical Framework

Sec. 2.1 resumes the knowledge about stellar rotation, the problem of binarity, and what is known about pulsation, winds, and magnetism. Sec. 2.2 refers to the circumstellar envelope, its shape, and the Viscous Decretion Disk model, which is the most successful model to explain how the material and angular momentum is transported throughout the disk and that is in agreement with the observations.

2.1 Central Star

2.1.1 Stellar rotation

Be stars rotate very fast but are not the fastest rotating stars as was thought years ago. Rotation can be a mechanism that triggers the Be phenomenon. An important parameter to describe the rotation of Be star is the critical or break-up velocity of a star, which is used to express when the gravitational force is the same as the centrifugal force at the equator. The star configuration is stable as long the equatorial rotational velocity remains below this quantity. Zorec et al. (2016) conclude, based on an exhaustive analysis of rotational velocities in a sample of 233 Be stars, that the mean ratio concerning the critical velocity is $v/v_c \approx 0.65$, with a wide distribution ranging from 0.3 to 0.95, meaning that Be star are not critical rotators. The critical velocity is written as:

$$v_{crit} = \sqrt{\frac{2}{3}\frac{GM}{R_p}};\ \Omega_{crit} = \sqrt{\frac{8}{27}\frac{GM}{R_p^3}}, \tag{2.1}$$

where M is the stellar mass, and the R_p is the pole radius, the $2/3$ factor is derived from the oblateness of the star, meaning that $R_{eq} = \frac{2R_p}{3}$ for critical solid body rotation, the equations are only valid in the Roche approximation. It is also possible to define a Keplerian circular orbital linear and angular velocity that are powerful tools to scale the disk rotation and are independent of the rotation type (i.e., differential or solid),

$$v_{orb} = \sqrt{\frac{GM}{R_p}};\ \Omega_{orb} = \sqrt{\frac{GM}{R_p^3}}. \tag{2.2}$$

These definitions can be grouped as a function of the angular and linear velocities and is given by,

$$\gamma = \frac{v_{rot}}{v_{crit}};\ \omega = \frac{\Omega_{rot}}{\Omega_{crit}}. \tag{2.3}$$

Another definition often used is W, which physically defines "what velocity boost is required for a given star to launch material into the closest possible orbit", i.e., just above the photosphere at the equator (Rivinius et al., 2013). W is defined as:

$$W = \frac{v_{rot}}{v_{orb}}. \tag{2.4}$$

Many studies (e.g., Cranmer, 2005; Ekström et al., 2008; Granada et al., 2013) reflect the importance of rotation in Be stars. High rotation rates are expected to be more frequent in early spectral types than late-type stars (Cranmer, 2005). One of the most drastic effects of their rotation is stellar oblateness (Maeder, 2009): Given the velocity at the equator, gravity shrinks as the equator grows, originating an oblate shape. Another important effect to consider is gravity darkening, where the equator is darkened concerning the poles, which is an effect that the emitted flux is proportional to the local gravity (von Zeipel, 1924), resulting in a decrease of the effective temperature T_{eff} as we move to the stellar equator. This is expressed via the following relation:

$$T_{eff} \propto g_{eff}^{\beta}, \tag{2.5}$$

where the exponent β for a pure radiative envelope (i.e., a black body) is set to 0.25, but at present is a function of the rotation rate W (Espinosa Lara & Rieutord, 2011). The oblateness shape of the star is related to the rotation rate W in the Roche approximation by,

$$\frac{R_{eq}}{R_{pole}} = \frac{W^2}{2} + 1. \tag{2.6}$$

Fig 2.1 shows the gravity-darkening effect on the Be star Achernar. Considering these elements, together with the fact that Be stars rotate very rapidly, would make their evolution in the MS similar to a less massive star, leading to a lower burning rate of hydrogen over a longer period (Maeder & Meynet, 2000).

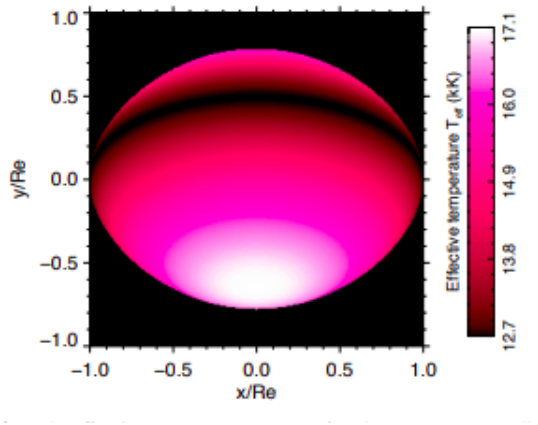

Figure 2.1: Temperature map of the Be star Achernar. The star is viewed at an inclination of 60 °, with $\beta = 0.166$ and $W \cong 0.84$. The star's oblateness is also observed with $R_{eq}/R_p = 1.352$. Credits to (Domiciano de Souza et al., 2014)

.

How Be Stars acquired their fast rotation is still an open question. Some authors study the possibility that Be stars were born as fast rotators (Zorec & Briot, 1997a; Klement et al., 2019). Another possibility is that Be stars spin up during the MS: models of stellar evolution predict the acceleration of the star's outer layers due to the contraction core. This distributes the angular momentum in all directions of the star, causing the outer layers to increase the angular rotation (Ekström et al., 2008; Granada et al., 2013). This scenario requires the star to be a fast rotator from the begging of its life, as well as an effective transport of the angular momentum in the star, and after the MS, the Be phenomenon may not longer be present in the star (Rímulo et al., 2018).

A further explanation for the fast rotation of Be stars is binarity. The work of Pols et al. (1991) contemplates that Be stars are formed through the evolution of mass-

transfer close binaries. In this scheme, a B star receives mass and angular momentum from its companion, who is on its way to becoming a Helium star (or sub-dwarf O) or a compact star. The main problem is to discover the binary companion of the Be star. Pols et al. (1991) found indications that less than 60% of Be stars are formed in this way. Other works from different authors found a different percentage of this issue. van Bever & Vanbeveren (1997) encounter a maximum of 20% and Zorec & Briot (1997b) a superior limit of 30%. Two works from Klement et al. (2017) and Klement et al. (2019) take this limit close to 100%, looking at the outer part (radio wavelengths) of the disk where hidden companions can truncate the disk, and this is revealed by a turndown in the radio part of the SED.

2.1.2 Pulsation

Pulsation is a key ingredient to understanding the Be phenomenon, and the work from the last decades has been to decipher if the variability with periods between 0.5 and 2 days is own to pulsation or fast rotation. To study pulsation, photometry is a very useful tool. Rivinius et al. (2003) estimated that low non-radial order g-mode pulsation (where gravity is the restoring force), with grouped multi-periodicity including modes with higher mode number **L**, is observed mainly in early Be stars. Higher-frequency p-modes (i.e., pressure is now the restoring force) with common frequencies between 6 and 15 days^{-1} are observed in Be stars but at a lower rate than stars that pulsate with g-mode pulsation. The development of space photometry has been beneficial to make progress in the field, and thanks to high cadence, it is possible to study the initial mass ejection of bright Be stars into the circumstellar envelope. Labadie-Bartz et al. (2022) studied 430 Be stars observed with the NASA TESS mission in the first year of the mission, where it was found that 97% of the stars show variability above the noise level. Also, almost every object observed presented a multi-period signal in the range between 0.5 and 4 day^{-1} (see Fig. 2.2), frequencies bigger than six days^{-1} were found at a fraction of 18 percent. In that figure (panel B), flickers can be observed, where the largest amplitude increases and brightness decreases are seen.

Besides photometry and time-series spectroscopy, it is essential to discriminate events that are occurring in the star itself as stellar pulsation, discrete or continuous

mass ejection episodes, and non-radial pulsation (hereafter NRP), among other processes that can happen simultaneously. So multiple observations with both techniques are necessary to capture a vast sample of disk build-up events to link it with NRP.

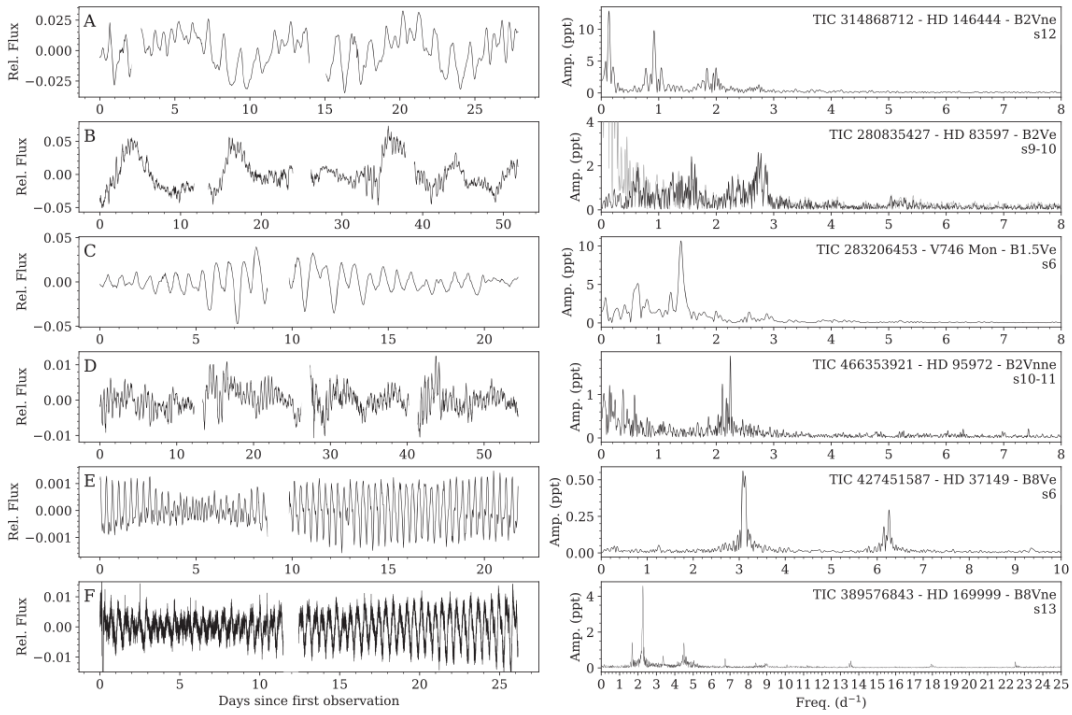

Figure 2.2: TESS light curves and frequency spectra for a representative selection of Be stars that show certain characteristics. The characteristic features that Labadie-Bartz et al. (2022) found are groups of close frequencies. Panel A shows three well-defined groups. Panel B shows two frequency groups and panel C is more difficult to observe, but there are also two frequency groups. In panel D, there is one group of frequency plus stochastic variations at lower frequencies.

.

2.1.3 CBes in binary systems.

The majority of massive stars are found in multiple systems. The fraction of multiple systems is found to be 90%, and the fraction of companions, which is defined as the average number of companions per central object, is greater than two (Sana, 2017). An investigation of the multiplicity properties, Dunstall et al. (2015) observed 408

B-type stars in the 30 Doradus region of the Large Magellanic Cloud (hereafter LMC), where a fraction of spectroscopic binaries [1] of 0.58 ± 0.11 was determined for this sample, therefore Be stars can be predicted to lodge in binary systems.

In addition, gravitation interaction between the Be star and the companion can be the responsibility of the cyclical variations of the V/R and cause ellipsoidal precession of the disk (Panoglou et al., 2018). The companion may irradiate the outer part of the disk and cause a tidal effect on it (Peters et al., 2016). Klement et al. (2019) proposed that the observed decay in the SED slope in the radio range corresponds to a truncation due to the companion. Long-baseline interferometry is the most potent technique with high-resolution radial velocity to detect new binary systems (Chini et al., 2012). Multiple Be stars are known to be in a binary system,e.g., π Aquarii, γ Cas, η Tau, ψ Per, κ Dra, Achernar, 66 Oph, etc.

2.1.4 Winds

High-velocity stellar winds can be observed in early and late Be stars, unlike B-type stars, where these winds are more common in early than late-type objects. This is seen in the broad short ward shifted UV lines of super ionized elements (C IV, Si IV, and N V) (Prinja, 1989). A solution to the built-up of the disk in CBe can be the radiation-driven winds plus the star's rotation that gives the circumstellar envelope's flaring shape structure. Regarding this, a hydrodynamic solution named Ω-slow (Curé, 2004; Araya et al., 2017) have been tested to describe an outflowing disk-like wind at the star's equator.

This is a new hydrodynamical solution to the standard radiation-driven winds theory (Castor et al., 1975; Friend & Abbott, 1986) for rapidly rotating stars with $v_{rot}/v_{crit} \gtrsim 0.75$, the main results of this solution are high mass-loss rate and slow wind, but one problem is that the terminal velocity is too fast to describe how are formed Be disk. A possible answer to this problem is to use the $\Omega-$slow solution with a treatment for the radiative force, decaying at larger distances in the radial direction and being larger near the star's surface. Following the procedure of de Araujo (1995):

[1] these are defined by their periods $< 10^{3.5}$ days and their mass ratio > 0.1

$$V_\phi = \Omega \sqrt{\frac{GM(1-\Gamma)}{R}} \left(\frac{R}{r}\right)^{\gamma_{visc}}, \tag{2.7}$$

where Γ is the mean opacity of the total flux, V_ϕ is the rotational velocity component of the wind in the equatorial plane, and γ_{visc} is a viscosity mimicking parameter, that if is settled to 0.5, representing a Keplerian orbit. To compute the radiative transfer calculations, the 3D code `HDUST` was used with a height scale defined by Eq. 2.20 and using Kurucz (1994) models that do not consider the deformation of the star. Theoretical SED and the Hα lines were performed to make a comparison between the Ω-slow solution and the VDD model (which is defined at Sec. 2.2.1).

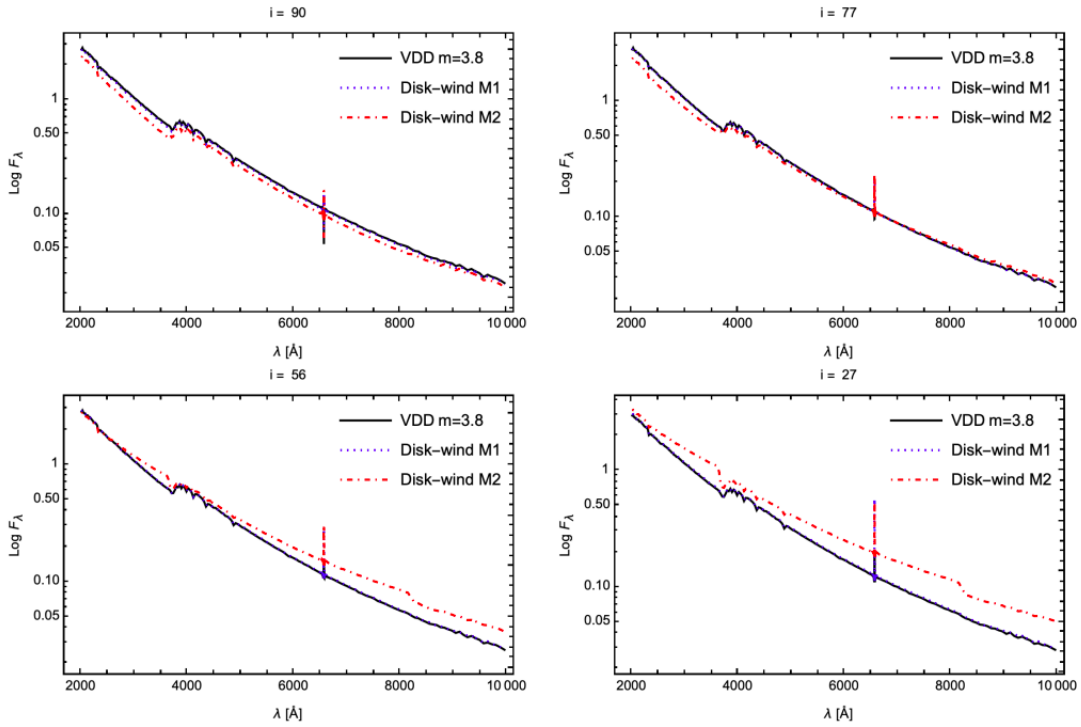

Figure 2.3: VDD models and disk wind SED computed with `HDUST`. VDD models are plotted with solid black lines. The mass-loss rate for models M1 and M2, respectively is 1.17 and $4.98 \times 10^{-8} M_\odot/yr$ and v_∞ for M1 and M2: 101 - 131 km/s. Credits to my professor C. Arcos.

In Fig. 2.3 two wind density distributions of a B2V star, with $T_{eff} = 21000$ K, $\log g = 4.00$ dex and $R_\star = 4.5\ R_\odot$, the base density is fixed to $\rho_0 = 5 \times 10^{11}$ gcm^{-3} are compared. These two models: M1 (dotted blue line) and M2 (dotted-dashed red line), have different values for the α_w factor (which is the ratio between the line force

Model	α	k	γ_{vis}	$\dot{M}$ ($10^{-8}\,M_\odot/yr$)	v_∞ (km/s)
M1	0.50	0.2	0.51	1.17	101
M2	0.62	0.2	0.51	4.98	131

Table 2.1: Wind density description. Models were generated with δ=0, Ω=0.99 and a base density ρ_0=5×10^{-11} g/cm^3. The stellar parameters are those for a typical B2V star, with T_{eff}=21000 K, log g = 4.00 and $R_\star$=4.5 $R_\odot$.

from optically thick lines and the total line force), the mass-loss rate and the v_∞ (see Table 2.1.

The preliminary results successfully reproduce a similar theoretical line-emission shape for a typical B2Ve star. Still, more work needs to be done to obtain clearer conclusions, and also, its needs to be compared with observations of Be stars.

2.1.5 Magnetic Fields in Be Stars

Massive stars are laboratories to study magnetism, as they affect the rotation rates of these stars, also the dynamics, structures, and the heating of the radiative winds of OB stars. One problem is that the detection of magnetism is small. Magnetism and stellar winds can explain angular momentum transport through the disk. That is why many campaigns have been created to fill this void. The Magnetism in Massive Stars (MiMeS) Project (Wade et al., 2009), the BOB (B Fields in OB Stars), and the LIFE project (Large Impact of Magnetic Fields on the Evolution of hot stars) are examples of this. They directly measure the magnetic fields on the surfaces of massive stars using Zeeman Doppler imaging techniques (Augustson, 2020). Regarding Be stars, the MiMeS project observed 350 OB hot, massive stars, of which 100 were Be stars, and no evidence of magnetic field was found (Wade et al., 2012). Other studies using low-resolution spectropolarimetry have been made to detect magnetic fields, but weak fields lower than 150 G have been reported (Yudin et al., 2011). Up to date, further conclusions about the role of magnetism in the formation of Be star disk have not been reached.

2.2 Disk of Be stars

The disk of CBe is the most peculiar characteristic of these objects; it is not inherited from the birth of these stars and can be observed with different observational techniques. The shape of the circumstellar envelope was known not to have spherical symmetry with the polarimetric and optical interferometric observations (McLean & Brown, 1978; Quirrenbach et al., 1997). Recent observations of Be stars have strongly confirmed this scenario with the number of opening half-angles of disks found between 0.15° and 4° in thin disks and increasing for thicker disks, going from 3.7° to 14° (Cyr et al., 2015).

Via the detection of FeII lines, Hanuschik et al. (1996) establish that the envelope of Be stars had to be thin and axis-symmetric. With the shape of the circumstellar envelope confirmed, the new question was how the disk supports it. This was debated in the 90s with the theory that satisfactorily explained all the observations, e.g., linear polarization, IR excess, and the emission of lines in the Viscous Decretion Disk (VDD) model.

2.2.1 The Viscous Decretion Disk model.

First submitted by Lee et al. (1991), then developed over the years by Bjorkman (1997); Okazaki (2001), Bjorkman & Carciofi (2005) and Curé et al. (2022), is the most successful theory to the date that has not been refused yet with any observations. It is very similar to the theory surrounding the accretion disk of Young stellar objects (hereafter YSO), but in this case, the mass loss flows outward from the central object. This theory does not explain how the mass is ejected from the star, but employing the action of viscous torques, close to 1% of the material that acquired sufficient angular momentum is placed in a thin equatorial disk (Haubois et al., 2012). This process keeps going as long as the mass enhancement of the material from the central star reaches a near-steady state. Finally, with a mechanism still not understood, the Be star became passive, in the sense that the build-up process is off and the inner disk re-accrete to the central star, following a slow dissipation of the outer part of the disk.

Since the VDD model follows the "α-prescription" developed by Shakura & Sunyaev (1973) where the kinematic viscosity coefficient ν can be characterized in terms

of a dimensionless α parameter:

$$\nu = \alpha H c_s, \tag{2.8}$$

where $\alpha \leq 1$, and that the disk is in vertical hydrostatic equilibrium and axis-symmetric, thin, and rotating in a quasi-Keplerian way, with the material outflowing out in the radial direction. Following the prescription of Bjorkman & Carciofi (2005) in the case of a steady disk in cylindrical coordinates (r, ρ, z) :

$$\frac{1}{r}\frac{\partial(r\rho v_r)}{\partial r} + \frac{1}{r}\frac{\partial(\rho v_\phi)}{\partial \phi} + \frac{\partial(\rho v_z)}{\partial z} = 0. \tag{2.9}$$

Assuming Keplerian rotation, $v_\phi \propto r^{-1/2}$ and no motion in the z-axis direction, $v_z = 0$, the continuity equation above mentioned takes the form of

$$\frac{\partial\left(2\pi r \Sigma v_r\right)}{\partial r} = 0. \tag{2.10}$$

From this equation, we can derive the matter per unit of time flowing out of the central star as $\dot{M} = 2\pi r \Sigma v_r$ where the radial velocity is given by

$$v_r = \frac{\dot{M}}{2\pi r \Sigma}. \tag{2.11}$$

If we consider the momentum equation in the ϕ direction

$$v_r\frac{\partial v_\phi}{\partial r} + \frac{v_\phi}{r}\frac{\partial v_\phi}{\partial \phi} + v_z\frac{\partial v_\phi}{\partial z} + \frac{v_r v_\phi}{r} = \frac{1}{\rho r}\frac{\partial P}{\partial \phi} + f_\phi, \tag{2.12}$$

where f_ϕ denotes all the external forces acting on the flowing material. This equation becomes more difficult to work if a viscous torque is added, considering $\frac{\partial v_\phi}{\partial \phi}$ and $\frac{\partial v_\phi}{\partial z}$ equals 0, the ϕ-momentum equation becomes

$$v_r\frac{\partial v_\phi}{\partial r} + \frac{v_r v_\phi}{r} = \frac{1}{r\rho^2}\frac{\partial\left(r^2\sigma_{r\phi}\right)}{\partial r}, \tag{2.13}$$

where $\sigma_{r\phi}$ is the viscous shear stress tensor and can be calculated by

$$\sigma_{r\phi} = (\alpha c_s H)\rho r\frac{\partial(v_\phi/r)}{\partial r}. \tag{2.14}$$

Multiplying Eq. 2.13 by ρr^2 and integrating all over ϕ and z, an expression for the torque is found, namely

$$\dot{M}\frac{\partial(v_\phi r)}{\partial r} = \frac{\partial \mathcal{T}}{\partial r}, \tag{2.15}$$

where

$$\mathcal{T} = \int_{-\infty}^{+\infty} r\sigma_{r\phi} 2\pi r dz = -3\pi\alpha c_s^2 r^2 \Sigma, \tag{2.16}$$

is the viscous torque. Taking a closer look at Eq. 2.15, it can be noted that the change in the angular momentum flux $j = rv_\phi$ is constrained by the gradient of the viscous torque. Since the $\dot{M}$ is constant from Eq. 2.10 it is possible to integrate Eq. 2.15 over r to get the final result, namely

$$\mathcal{T} = \dot{M} V_{crit} \sqrt{r R_\star} + c, \tag{2.17}$$

where the constant c determines the "disk truncation". Substituting Eq. 2.16 in the above equation it can be obtained a formula for the surface density

$$\Sigma(r) = \frac{\dot{M} v_{orb} R_\star^{1/2}}{3\pi\alpha c_s^2 r^{3/2}} \left[\left(\frac{R_0}{r} \right)^{1/2} - 1 \right]. \tag{2.18}$$

A reliable approximation of the VDD model, which is often used because it is in agreement with the observations, is that the density distribution falls off as a power law radially (r) and a Gaussian distribution in hydrostatic equilibrium axisymmetric respect to the mid-plane of the disk in the vertical direction (z). So in this approximation, the volumetric density distribution can be written as:

$$\rho(r, z) = \rho_0 \left(\frac{r}{R_\star} \right)^{-m} \exp\left(\frac{-z^2}{2H^2} \right), \tag{2.19}$$

where ρ_0 is the disk base density, $R_\star$ is the stellar radius, and H is the height scale that sets the flaring of Be stars and is given by

$$H = H_0 \left(\frac{r}{R_\star} \right)^{\beta}. \tag{2.20}$$

For an isothermal disk, β=3/2 and the constant H_0 is defined as

$$H_0 = \left(\frac{2\, R_\star^3\, k\, T_0}{G\, M\, \mu_0\, m_H} \right)^{1/2}, \tag{2.21}$$

where M is the stellar mass, G is the gravitational constant, m_H is the mass of a hydrogen atom, k is the Boltzmann constant, μ_0 is the mean molecular weight of the gas and T_0 is an isothermal temperature used only to fix the vertical structure of the disk initially.

Although this basis is for a steady state of the circumstellar envelope, this is not always true in reality due to the variability of CBes and the nature of the mass-injection rate of the disk, so a true steady state is never reachable at 100% (Okazaki, 2007), but a quasi-steady state for the density is more probably (Haubois et al., 2012).

CHAPTER 3

π Aquarii

π Aquarii (HD 22571, HIP 110672) is a bright, rapidly rotating classical Be star observed for over 100 years, presenting mid- and long-term variability. McLaughlin (1962) reported variations over 50 years in the line profile of Hα and Hγ, where more of the profiles were observed in double-peaked line-emission indicating probably the active phase of the disk of π Aquarii. He also noted a significant change, from 0.5 to 4.0 units in the V/R ratio, pointing out a signal of asymmetries in the disk. This was the first attempt to study the disk's activity in π Aquarii even though the stellar and disk parameters were not determined.

Several authors: Nordh & Olofsson (1974), Underhill et al. (1979), Snow (1981), Theodossiou (1985), Goraya (1985), Fabregat & Reglero (1990) and Zorec & Briot (1991) studied this star over the years trying to establish the fundamental parameters by using different techniques of observations, such as multi-color, photometry, interferometry, polarimetry, and high-resolution spectroscopy. Their results are summarized in Table 3.1.

McDavid (1986) used polarimetric data and found that the previous active phase started approximately in 1950, reaching its maximum around 1985, where the polarization level was greater than 1%. After that, the emission line decreased, and the brightness of the central star began to decrease, reaching its minimum value in

Table 3.1: Stellar and wind parameters from the literature.

T_{eff}	22500 to 30000 K
log g	3.3 to 4.0
D	331 to 435 pc
M_V	-3.00 to -3.83 ^{mag}
V	4.53 to 4.93 ^{mag}
A_V	0.25 - 0.69 ^{mag}
v_∞	1450 km s^{-1}
$\dot{M}$	2.61×10^{-9} $M_\odot$ yr^{-1}

1996. This behavior was extended up to 2002 in a quasi-normal phase of the star. Hanuschik et al. (1996) proposed that π Aquarii has a companion due to the broad and complex Hα line profile observed.

Bjorkman et al. (2002) performed long-term observations of the star, obtaining information about the behavior of the disk phases of π Aquarii. They calculated new parameters of the binary system for the first time by fitting the photometric data with Kurucz stellar atmospheres models [1] (Kurucz, 1994) in a wavelength range of 0.36 to 2.2 μm obtained in 1998, together with an 8.28 μm Midcourse Space Experiment (MSX) flux and International Ultraviolet Explorer (IUE) fluxes from 0.12 to 0.31 μm from 1995. With all these data, the best-fit atmosphere model has the following values: $T_{eff} = (24000 \pm 1000)$ K and for the interstellar reddening $A_V = (0.15 \pm 0.03)$ mag, using a distance of 340^{+105}_{-70} pc from HIPPARCOS(Esa, 1997) to derive $\log(L_{bol}/L_\odot) = (4.1 \pm 0.3)$ dex and $R_\star = (6.1 \pm 2.5)\, R_\odot$.

Making a comparison with theoretical evolutionary tracks of Schaerer et al. (1993), the estimated mass of π Aquarii is $M = (11 \pm 1.5)\, M_\odot$, $v_{crit} = 585^{185}_{-95}$ and $\log g = (3.9 \pm 0.1)$ dex. They also suggested an inclination angle $50^\circ \leq i \leq 75^\circ$, based on previous studies on the FeII 5317 Å double-peaked emission line, and taking into account that the central depression observed in Balmer lines between 1989 and 1995, is not as deep as if we look at it at edge-on.

[1] models in local thermodynamic equilibrium (LTE), with plane-parallel geometry, hydrostatic atmospheres for a broad range of metallicities

By examining the periodical RV variations of a Hα weak emission line in the quiet phase (1996-2001), with a semi-amplitude of 101.4 kms^{-1}, they obtained an anti-phased RV variation with the photospheric absorption (semi-amplitude of 16.7 kms^{-1} with a period of 84.1 days, which they suggested is the period of the binary companion. They concluded that if π Aquarii is a spectroscopic binary, the companion should be surrounded by a gas envelope and probably an A-F main-sequence star. Considering this, they derived the binary parameters: $M_1 \sin^3 i = 12.4\, M_\odot$, $M_2 \sin^3 i = 2.0\, M_\odot$, $a = 0.96\ \sin^{-1} i\, [AU]$ and $M_2 = 0.16\, M_1$.

Zharikov et al. (2013) recollected data over 40 orbital cycles from 2004 to 2013, analyzing variations of double peak asymmetric Hα profiles. They looked for a periodicity in the V/R ratio, finding 84.1 days, which agrees with the orbital period of the binary companion of π Aquarii found by Bjorkman et al. (2002). Also, they used evolutionary models to calculate the stellar parameters of the binary system, which are presented in Table 3.2. They studied the disk's structure employing a Doppler tomography showing a non-uniform structure. A bright hot spot inside the disk, with a one-armed spiral density pattern structure, was found in phase with the secondary. Moreover, the computation of the disk radius of $\sim 65\, R_\odot$ (corresponding to $\sim 0.33\, AU$) was estimated assuming Keplerian motion of a particle in a circular orbit at the outer disk.

Nazé et al. (2019) performed a new analysis of π Aquarii, classifying it as a γ-Cas type, wherein the star presented a bright and hard X-ray emission. They collected data between 2013 and 2019 from the BeSS database[2] (Neiner et al., 2011; Neiner, 2018) finding that the emission line profile seen at Hα almost disappears in January 2014. Then, the emission resembled the active phase seen from 1950 to 1990. Zharikov et al. (2013) used a similar technique. They implemented a tomographic analysis of all lines in the spectra. A striking result was that the spot found by Zharikov et al. (2013) is no longer present after 2016, proving a change in the behavior of the disk. In addition, the disk's inner edge was closer to the central star, suggesting an increased disk size.

After all these studies, what is interesting to characterize is the behavior of the central star and the disk of π Aquarii after 2014. This can be done using spectroscopy

[2]http://basebe.obspm.fr/basebe/

Table 3.2: Adopted parameters of π Aquarii from Zharikov et al. (2013)

Period	84.1 days
M_1	$14 \pm 1\ M_\odot$
T_{eff}	$24\,000 \pm 1000$ K
$\log L/L_\odot$	4.7 ± 1
R_1	$13 \pm 1.4\ R_\odot$
v_c	453 km/s
M_V	-4.64 $\pm$ 25
q mass ratio	≥ 0.165
i	$65^o - 85^o$
M_2	$2.31 \pm 16\ M_\odot$
a	0.96 AU
Distance	740 ± 90 pc

data from known catalogs BeSS and BeSOS, described in the next chapter.

CHAPTER 4

Sample

In this chapter, I describe the data acquisition used in this thesis. Information about the wavelength range, spectral resolution, observation dates, and reduction steps are given in the text. Mainly, two databases were used: BeSOS, which is described in Sec. 4.1, and BeSS, which the information is provided in Sec. 4.2. A general description of the spectral variability, accompanied by an image showing the line profiles, is also given in Sec. 6.2.

4.1 BeSOS database

The Be Stars Observation Survey (BeSOS)[1] is a catalog of high-resolution spectra in the visible range, obtained using the Pontificia Universidad Católica High Echelle Resolution Optical Spectrograph PUCHEROS, developed at the Center of AstroEngineering of Pontificia Universidad Católica de Chile. The instrument is installed at the 50-cm telescope of the Observatory Universidad Católica Santa Martina, near Santiago, Chile. The design is a basic echelle spectrograph, with 1024 x 1024 pixels of 24 μm. BeSOS also can be used to corroborate and detect new Be stars by combining photometric data from the literature (i.e., IR excess) with spectroscopic data (e.g., Arcos et al. 2018). Data from the database are already reduced by usual reduction

[1] http://besos.ifa.uv.cl/

steps with IRAF (details are available in Arcos et al. 2018). More information about the instrument can be found in Vanzi et al. (2012); details about the main characteristics are given in Table 4.1.

Table 4.1: PUCHEROS spectrograph

Spectral resolution $\lambda/\Delta\lambda$ (average)	18000
Spectral coverage (single shot)	$3900 - 7390$ Å
Orders	41
Aperture on the sky (diameter)	3.5″
Limiting visual magnitude	$V = 9$
Spectral sampling	2.4–3.4 pixel

A total of 7 spectra of π Aquarii are available from the BeSOS database, where two were observed on Nov 14, 2012; three on Jul 24, 2013; and the last two on Oct 24, 2015. The spectra were averaged for each night, obtaining three spectra with an effective wavelength range from 4200 to 7200 Å.

4.2 BeSS

The Be Star Spectra BeSS[2] database (Neiner et al., 2011; Neiner, 2018) contains a catalog of classical Be stars, Herbig Ae/Be stars and B[e] supergiants. The catalog is complete up to magnitude V$\sim$11. For each star, the catalog gathers information on its parameters, such as coordinates, magnitude, temperature, gravity, projected rotation velocity, spectral type, etc.

A total of 16 echelle spectra of π Aquarii were obtained from the BeSS database in the visual region, one spectrum in 2001, from 2008 onward, at least one spectrum per year up to 2022 (the wavelength range differs for each spectrum, see Table A.1 for more details). To normalize to the continuum the spectra from BeSS, I used the python tool *specutils*[3].

Regarding Hα, we recollected 516 spectra from 1996 to 2022 from the BeSS catalog,

[2] `http://basebe.obspm.fr/basebe/`

[3] `https://specutils.readthedocs.io/en/stable/index.html`

where only this spectral line is available. It is important to note that not all data have the same instrument and resolution. Observations with the lowest resolution are in the order of ~ 5800, and observations with the highest resolution are around ~ 20000. See Table A.2 for more information on the instruments and resolution.

We have 19 spectra considering the visible region's BeSS and the BeSOS sample. For Hα a total of 535 data were used and analyzed for this thesis considering the three spectra from BeSOS and the 16 echelle spectra from BeSS. The Hα emission line profiles are plotted in Sec. B to appreciate the variation over the years.

CHAPTER 5

Methods

This chapter discusses the measurements and the best models. The chapter is separated into two sections. Sec. 5.1 describes the method to obtain the EWs, V/R, DPS, and RVs of several spectral lines and how I compute the error for each measurement. It is also shown how the periods of the RV and V/R of Hα were obtained. Sec. 5.2 describes the main features of the 3D geometry radiative transfer code `HDUST`, which was used to study the disk parameters of π Aquarii. A study of how the influence of input parameters affects the theoretical line profile is also shown at the end of this chapter.

5.1 Description of the parameters estimation in π Aquarii

First, to improve the smoothness of the signal in the several spectral lines of π Aquarii, a Savitzky-Golay (Savitzky & Golay, 1964) filter is used to eliminate the noise in all lines except Hα. An open Python source [1] is utilized to compute the filter that calculates a polynomial fit of order 3 for each window of size 20, on this thesis. An example of the result after applying this filter is shown in the bottom panel of Fig. D.1.

[1] `https://docs.scipy.org/doc/scipy/reference/generated/scipy.signal.savgol_filter.html`

5.1.1 Equivalent width

We calculated the EW of the spectral lines presented in Table 6.3. We used different methods depending on if the observed line is in emission or absorption. In the case of emission lines, i.e., Balmer, the HeI lines $\lambda\lambda$ 5015 Å, 5047 Å, 5875 Å, and 6678 Å and the FeII lines $\lambda\lambda$ 4232 Å, 4584 Å, 5169 Å, 5198 Å, 5235 Å, 5276 Å, 5316 Å, and 5363 Å, it was subtracted the contribution of the stellar photosphere. This step was made by fitting a stellar atmosphere model to the deepest HeI 4471 Å line available in our sample, with an EW of 1.03 Å. The spectrum presenting this characteristic was for the observation date on Jul 23, 2013. In this way, we are considering this date as the spectrum representing the stellar photosphere. The stellar atmosphere model was obtained with the code `ZPEKTR` (Levenhagen, 2014), which employs `TLUSTY` (Hubeny & Lanz, 1995a) stellar atmosphere models but for rapidly rotating stars, and then, considers the effects of gravity darkening, limb darkening and oblateness of the star. This analysis was performed by Daniela Turis, a master's student at the Universidad de Valparaíso. The best-fit model for Hα is shown in Fig. 5.1 and is represented with a solid blue line. After removing the stellar photosphere contribution, the EW was computed considering the zero moments (see Eq. 5.1). Regarding absorption lines, the EW was calculated using the Eq. 5.2.

$$M_0 = -\sum_{i=1}^{N} F_i \Delta x_i, \tag{5.1}$$

$$M_0 = \sum_{i=1}^{N} (1 - F_i) \Delta x_i, \tag{5.2}$$

where F_i is the normalized flux and Δx_i is the difference between two consecutive wavelengths.

To estimate the error of the EW, the Bootstrap re-sampling method (Efron, 1979) was implemented. The method constructs hypothetical data sets derived from the observed data, picking random points with replacement. Any data points may occur one or more times or maybe not be selected. The data points have size N, the size of the observed data. The EWs are computed using Eq. 5.2 with the new bootstrapped data set. The process was repeated 1000 times. The final value is given in the form: EW $\pm\,\sigma^*$, where σ^* is the standard deviation of the entire bootstrapped data set and the final error estimation for the EW.

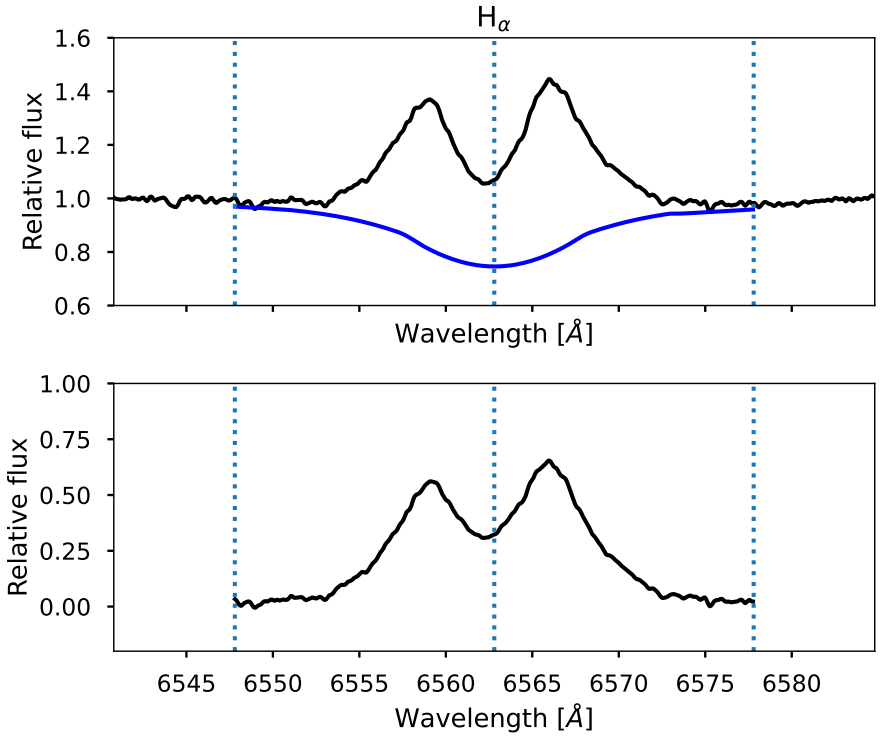

Figure 5.1: Measurements of EW for spectral emission lines (solid black line) of the night Jul 23, 2013. *Top :* the best stellar atmosphere model from ZPEKTR is shown with a solid blue line. *Bottom:* subtracted stellar photosphere contribution. Dashed blue lines indicate the spectral window where the EW was calculated. The central dashed line indicates the theoretical rest wavelength of Hα line.

5.1.2 Violet to Red peak intensity ratio and double-peak separation

For all emission lines in Table 6.3, we calculated the V/R and the DPS. These values are directly related. We can obtain the wavelength for the red and violet peaks to calculate the DPS, the distance between these points in wavelength or velocity units.

Most of the emission lines presented in π Aquarii show a clear DPS, so the calculations of V/R and DPS are performed with Case 1, described below. For Hα emission lines, where its profiles present a complex geometry over time, we classified the observed emission lines in three different shapes (cases), described as follows:

- **Case 1**: This case is for double-peaked emission lines distinguished. In the case

of Hα line, from 2004 to 2014, approximately, we have these kinds of profiles. The method was to fit two Gaussian profiles, one for each peak. The center of each Gaussian gives the violet and red peak value, respectively (see Fig. 5.2).

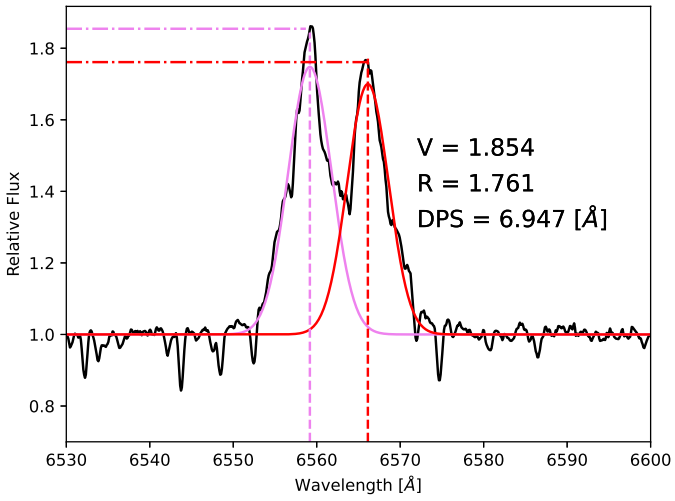

Figure 5.2: Case 1: V/R measurements for a distinguished DPS profile. The Gaussian fits are represented in pink and red for the violet and red peaks, respectively. The observation is represented as a solid black line. The dashed lines indicate the Gaussian fit's center and the values for both peak intensities. Values for this example are shown as a legend in the plot.

- **Case 2**: Unlike Case 1, in this profile, the central absorption is not seen clearly, and it looks more like a third peak, but still with the violet and red peak distinguished on each side. These kinds of Hα emission lines are observed from 2014 to 2022. The method used here was to locate the geometrical center of the line and the maximum emission at this center. The code then looks for the maximum intensities from each side of the center. Fig. 5.3 shows an example of this method.

- **Case 3**: similar to Case 2, but with a flat emission line, making it difficult for the code to distinguish between the two peaks. The intensity peaks were selected by visual inspection between the extremes from each side of the geometrical center of the line. The intensity peaks were selected by visual inspection between the peaks from each side of the geometrical center of the line (see Fig. 5.4).

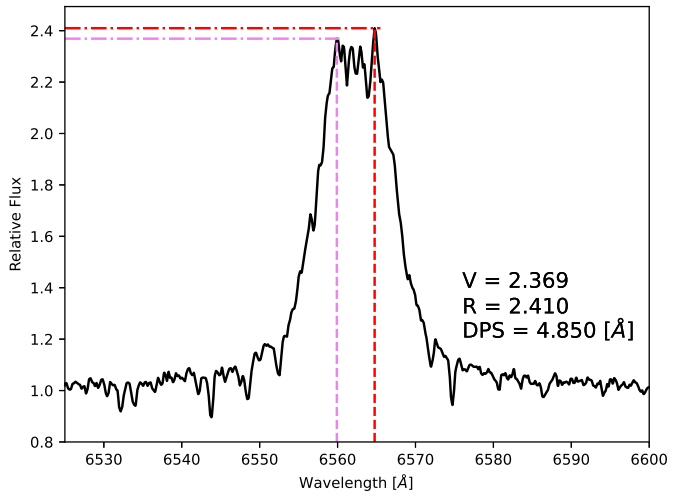

Figure 5.3: Case 2: V/R measurements for prominent emission profiles. The geometrical center of the observed line determines the maximum intensity in the middle of the line. The code selects the maximum intensities from each side of the center (dashed vertical lines).

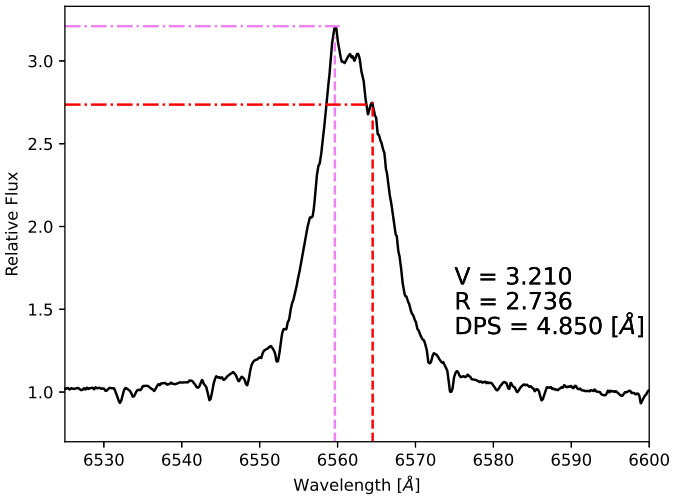

Figure 5.4: Case 3: V/R measurements made by visual inspection. For these cases, the peaks were selected by visual inspection from each side of the geometrical center of the line (dashed vertical lines).

5.1.3 Radial velocity

For all spectral lines in Table 6.3, we calculated the RV. The RV is not computed in the case of dates where a continuum profile is observed. Spectra from BeSS were corrected by barycentric velocity before measuring the RV. For the absorption and emission lines, we first convert the wavelength to velocity units by using the theoretical values from the National Institute of Standards and Technology (hereafter NIST) database[2] (see Table C.1 for more details). Then, we used the center of the full-width at half maximum (FWHM) of the line to measure the RV (see Fig. 5.5). We followed the Doppler formula to obtain the values:

$$v = \frac{\lambda - \lambda_0}{\lambda_0} c, \tag{5.3}$$

where λ_0 and λ are the theoretical rest wavelength and the observed wavelength, respectively, and c is the speed of light.

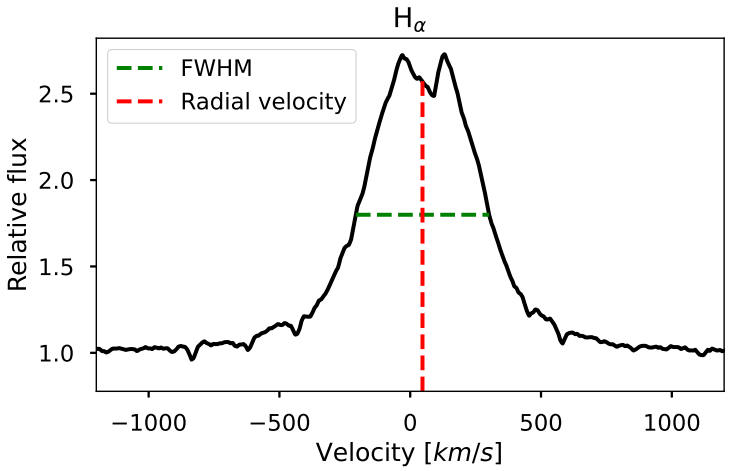

Figure 5.5: Method used to measure the radial velocity in emission lines. The horizontal dashed green line indicates the FWHM of the line, while the vertical dashed red line indicates the center of the FWHM used to obtain the RV.

[2] https://physics.nist.gov/PhysRefData/ASD/lines_form.html

5.1.4 Errors

The spectra used in this work come from different instruments with different spectral resolutions. To account for the fitting errors on the measurements of the V/R, DPS, and RVs, considering the different spectral resolutions, we used an open module from `Python`[3] to degrade a line profile to a lower spectral resolution. The Tables A.1, A.2, and 4.1 contain a list of all instruments and spectral resolutions for the available data. We chose a spectrum with R=20000, the highest resolution in our sample, to degrade it to the lowest resolution available in our data, R=5800. Then, we measured the EW, V/R, and DPS in both profiles and calculated the percentage error in Case 1 (and 2) for V/R and DPS, errors are 3% (and 2%) and 12% (and 4%), respectively. For case 3, we are considering the maximum error estimation found between both cases. We applied the same procedure for the RVs to evaluate the error, getting a value around 5%. In summary, percentage errors are 3%, 12%, and 5%, respectively, for V/R, DPS, and RV.

Fig. 5.6 shows how is performed the error estimation for case 1 for the V/R and the DPS; it is observed how the degrading of the profile affects the outcome of these parameters.

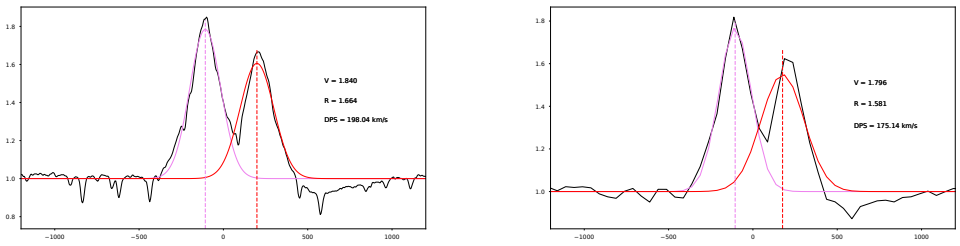

Figure 5.6: Calculation of V/R and DPS for the case 1 in a spectra of R=20000 (Left) and R=6000 (Right).

5.1.5 Periods

As was previously mentioned in this thesis, there are a high number of data covering the Hα line-emission for π Aquarii, also with a high cadence. We have calculated the

[3] `https://coronagraph.readthedocs.io/en/latest/index.html`

period of the V/R and RV shift variations using a program developed by Nikutta (2021), that uses a tool from the open source `Python`[4]. This program implements the Lomb-Scargle (hereafter LS) periodogram (Lomb, 1976; Scargle, 1982), an algorithm that detects and characterizes periodic signals. One of the benefits of using the LS periodogram is the severe reduction of the frequency aliasing. (i.e., higher frequency signal appearing lower after sampling at a rate that is too small), so it is possible to recognize periodic components with a higher frequency than the *Nyquist frequency*(Vio et al., 2013).

Given a set of data measurements x_n, $n = 1, ..., N$ observed at time t_n, the LS periodogram at frequency f is constructed as follows: the data mean, and variance are computed by:

$$\bar{x} \equiv \frac{1}{N}\sum_{i=1}^{N} x_i, \qquad \sigma^2 \equiv \frac{1}{N-1}\sum_{i=1}^{N} (x_i - \bar{x})^2, \tag{5.4}$$

then, the LS periodogram is computed by:

$$P_{LS}(f) = \frac{1}{2}\left\{ \frac{(\sum_n g_n \cos(2\pi f[t_n - \tau]))^2}{\sum_n \cos^2(2\pi f[t_n - \tau])} + \frac{(\sum_n g_n \sin(2\pi f[t_n - \tau]))^2}{\sum_n \sin^2(2\pi f[t_n - \tau])} \right\}, \tag{5.5}$$

where f is the frequency, the term g_n depends on the mean and the variance of the sample, and the time offset is defined by:

$$\tau = \frac{1}{4\pi f} \tan^{-1}\left(\frac{\sum_n \sin(4\pi f t_n)}{\sum_n \cos(4\pi f t_n)} \right). \tag{5.6}$$

The periodogram reduces to the classical form in the case of equally-spaced observations. The τ constant is useful to make $P_{LS}(f)$ invariant to shifting in t_n by any constant. A remarkable feature of the LS periodogram is that it is analogous to the equation obtained if it is estimated the harmonic content of a data set at a given f by linear least-squares fitting to the model $x(t) = A\cos(2\pi f t) + B\sin(2\pi f t)$ (Press & Rybicki, 1989).

[4] `https://docs.astropy.org/en/stable/timeseries/lombscargle.html`

5.2 Measurement of the disk parameters of π Aquarii

In the second part of this thesis, the disk parameters of π Aquarii are investigated. A code that solves the radiative transfer equation in a gas medium, such as for Be stars, is required to accomplish this task. In this context, the 3D geometry, Non-LTE Monte Carlo radiative transfer code, `HDUST`, can reproduce theoretical Balmer lines, among other spectral series for hydrogen, and the spectral energy distribution, images, and polarization. We use this code to reproduce the Hα, Hβ, Hγ, and Hδ line profiles.

5.2.1 HDUST

`HDUST` (Carciofi & Bjorkman, 2006; Carciofi & Bjorkman, 2008) is a code written in `FORTRAN` able to solve the radiative transfer equations in arbitrarily shaped 3D media, using a Monte Carlo technique. `HDUST` implements gravity darkening and rotational flattening since Be stars rotate very fast and also take into consideration opacity sources such as Thomson scattering and limb darkening.

A given number N of photons packets (hereafter PPs) with energy $E_\gamma = L\Delta t/N_\gamma$, randomly propagates through the interaction medium in which the radiation propagates. They can be scattered, absorbed, and re-emitted until they finally depart the interaction region. The PPs are defined to be monochromatic and have the same energy when they leave the star to ensure flux conservation.

Because the disks of Be stars are massive, a large sample of PPs emitted from the star is simulated to establish the gas disk state variables (density, kinetic temperature, and level populations). `HDUST` divides the disk into n_r cells in the radial direction, each divided in the latitude direction and, if necessary, in azimuthal cells. The simulations begin with estimating the state variables and the radiative rates. The heating rates of the gas are sampled while the Monte Carlo simulation of the photons is performed through the cells. New simulations are carried out until the state variables converge to equilibrium values for every cell. After the simulation, it updates the level populations, gas temperature, and disk density. Between 10^6 and 10^9 iterations are done to obtain the convergence of the simulation. The code's output consists of flux, images, and polarization for any desired spectral interval (Rubio, 2019).

This work uses the steady-state power-law approximation for the disk density, i.e., Eq. 2.19. A source for the central star needs to be defined. One option is the self-consistent rigid rotator model in the Roche approximation where three parameters as input are supplied: M, W, and t/t_{MS}, where t_{MS} is the age in the main sequence of the star. With these parameters as input, the photospheric parameters (R_p and L) are calculated from the Geneva models (Ekström et al., 2008; Georgy et al., 2013; Granada et al., 2013), that computes the stellar evolution and structure of fast-rotating massive stars. The other option available is the parametric rigid rotator, where all the following parameters must be provided: M, R_p, R_e/R_p, L, $\log g$, V_{rot} and T_{eff}. For the stellar spectrum, the stellar atmosphere models of Kurucz (1994) is used. The limb darkening models from Claret (2000) are adopted to outline the photospheric specific intensity as a function of direction. The code takes as input three disk parameters: the number density n_0[5], the radial exponent n and the disk truncation radius R_d. The isothermal temperature was fixed at $T_0 = 0.72\ T_{eff}$, the mean molecular weight of hydrogen $\mu = 0.6$ and the gravity darkening exponent $\beta_{GD} = 0.25$ for all the models.

To find the best-fit model with HDUST first, I search in the literature for the stellar and disk parameters available for π Aquarii (see Bjorkman et al., 2002; Zharikov et al., 2013; Arcos et al., 2017, 2018; Cochetti et al., 2019), among other author described in Chapter 3. Table 5.1 displays the complete grid of parameters used in this thesis, where the combination between these was utilized to create the models, for each model, a total of 10 inclinations were used as input. The National Laboratory for High-Performance Computing Chile (hereafter NLHPC) and the servers belonging to the Universidad de Valparaíso were used for running these computationally extensive simulations.

5.2.2 Study of HDUST

An initial study of the code was performed to understand how the input parameters affect the theoretical lines computed with HDUST. We create a model with the stellar parameters fixed in the self-consistent parametric option of the code, which will be used as a reference for the study of the code: $M = 11.8\ [M_\odot]$, $R_p = 5.2\ [R_\odot]$, W$= 0.8$,

[5]The volumetric base density can be calculated as $\rho_0 = n_0 \mu m_H$ where m_H is the hydrogen mass and μ is the mean molecular weight of the gas.

L= 11913 $[L_\odot]$. We started with $n_0 = 5.0 \times 10^{11}$ [cm^{-3}], n= 2.5, $R_d = 30$ $[R_{eq}]$ and $T_0 = 0.72\ T_{eff}$ for the disk parameters, $\mu = 0.6$ and the gravity darkening exponent $\beta_{GD} = 0.25$ are fixed for all the models. This model is shown with a gray solid line in Fig. 5.7 and 5.8.

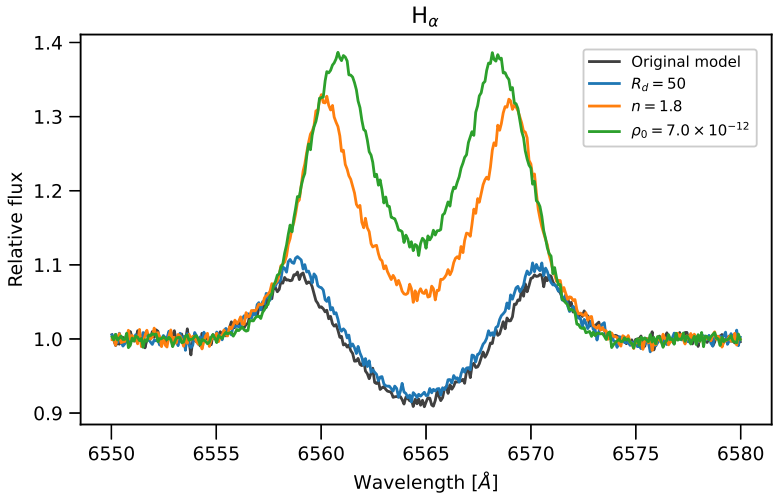

Figure 5.7: Hα synthetic line computed with `HDUST`. The disk parameters (R_d, n, and n_0) are varied concerning the reference model. The same inclination 52° is fixed for all models. See the text for discussion.

For each model, one was changed to only one parameter, and the others are the same concerning the original model (gray solid line). In Fig. 5.7, the solid blue line represents a model with $R_d = 50\,R_{eq}$, the solid orange line was computed with a lower $n = 1.8$ and the solid green line represents a model with a larger number density $n_0 = 7.0 \times 10^{12}$ $[cm^{-3}]$, which is a lower base density, concerning the original model.

From this example, we can see that the double peak in emission is not affected by changing the disk truncation (see blue and gray lines), so it can be deduced that the emission of Hα ends at a lower radius. By changing the value of n to a lower value (orange color), a narrower central absorption and a higher intensity are observed. The disk density (green color) increases directly affect the line emission. Finally, changing the number density affects similarly to lowering the exponent n, i.e., the intensity increases, and the central absorption becomes thinner (because of the presence of a

denser disk). This can be explained as well by looking the Fig. 5.9, where the behavior of the density distribution is closely dependent on the parameter m, where for larger values of n, the density decays steeper, so we have a decreasing in the intensity of the line.

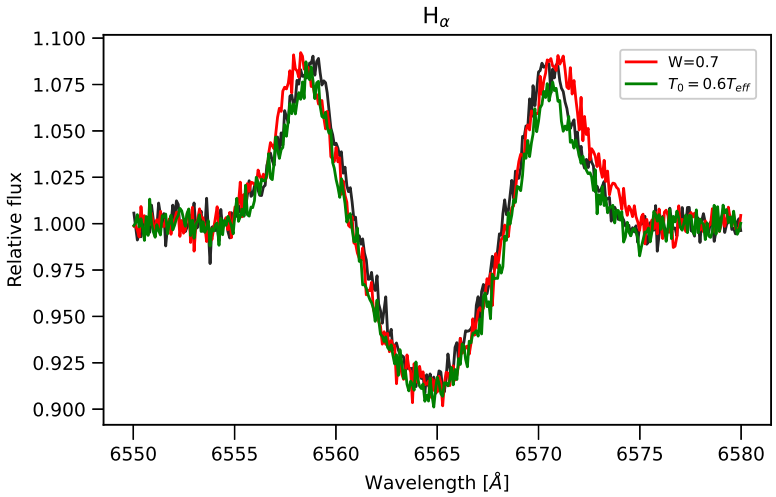

Figure 5.8: Same as Fig. 5.7 but for different values W and T_0. See the text for discussion.

Fig. 5.8 shows another comparison with the reference model. First, the rotation rate W is reduced. At this point, it is important to note that by changing the rotation rate, other parameters are also altered, such as the γ, ω, and v_{rot}, the solid red line represents a value of $W = 0.7$, where not relevant differences are appreciated in the plot. The solid green line represents a change in the initial temperature of the disk with a value of $T_0 = 0.6\ T_{eff}$, and it is noted widening in the wings concerning the solid gray line.

In conclusion, for our models, we have to consider that by decreasing the n exponent or increasing the n_0 parameters, a similar outcome for the synthetic models of `HDUST` is observed. The emission for Hα is up to 30 R_{eq} for this code, and a $W > 0.7$ produce similar results.

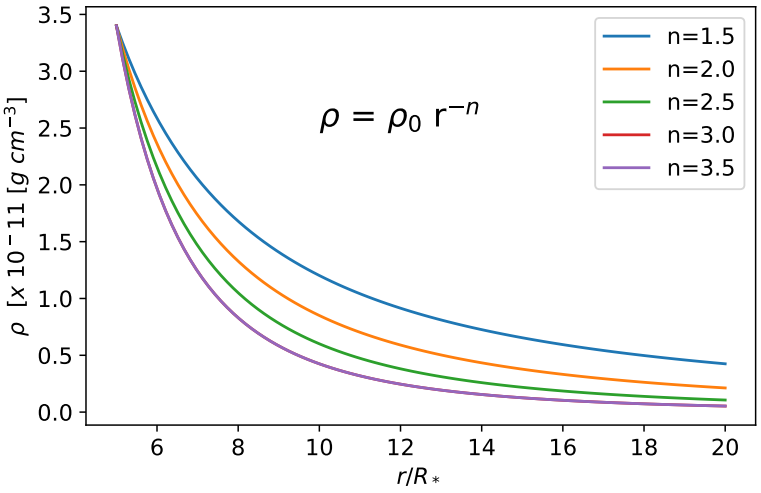

Figure 5.9: The gas density distribution in the disk considered in HDUST . The volumetric density falls off radially as a power law with an exponent m.

Table 5.1: Grid of π Aquarii parameters used in HDUST

Parameters	Values
M [$M_\odot$]	10.3 - 11.5 - 11.8 - 13.2 - 14
R_{eq}/R_{pole}	1 - 1.15 - 1.28 - 1.29 - 1.30 - 1.31 - 1.32
log ρ_0	-12, -11.3, -11.26, -11.12, -11, -10.7, -10.63
	-10.54, -10.52, -10.41, -10.4, -10.3, -10.22, -10.15
n	1.5 - 1.8 - 2 - 2.4 - 2.5 - 2.8 - 3 - 3.1
R_d [R_{eq}]	12.5 - 20 - 25 - 30 - 35 - 40 -50
i $^\circ$	18 - 27 -32 - 41 - 43 - 48 - 49 - 50 - 51
	52 - 53 - 54 - 57 - 58 - 59 - 60 -61
	62 - 63 - 66 - 68 - 70 - 76 - 81 - 87

CHAPTER 6

Results

This chapter presents and describes all results obtained in this thesis. Sec. 6.1 described the stellar parameters found using the ZPEKTR code. Sec. 6.3 contains the spectral variability associated with changes in the star and disk. The results of EW, RV, V/R, and DPS of Balmer, Iron, and Helium lines are presented. This section also includes other spectral lines present in the spectra. Finally, sec. 6.4 studies the disk parameters of π Aquarii employing HDUST.

6.1 Stellar Parameters of π Aquarii

The stellar parameters of π Aquarii were estimated by using a small grid of approximately 1000 models, which were created with the code ZPEKTR using the gravity darkening law of Espinosa Lara & Rieutord (2011) and based on the stellar parameters available in the literature (see Table 6.1). We looked for the best models from this grid to determine an average value for each stellar parameter and their corresponding errors. To select the range of best models, we use a figure-of-merit $\mathcal{F} = \chi^2_{i+1}/\chi^2_0$ to obtain a distribution of the best representative models on which the average results are based, χ^2_0 is the smallest value for χ^2 and "i" goes from 0 to 150. The χ^2 is calculated between the stellar atmosphere model and the observed spectrum in the region covering the spectral line HeI 4471 Å. As mentioned previously, we selected the spectra representing the strongest absorption spectra of HeI 4471 Å available,

this corresponding to the observation taken on Jul 23, 2013. The best model and the observed spectral line are displayed in Fig. 6.1.

Table 6.1: Grid of π Aquarii parameters used in ZPEKTR, all the models were carried out using limb darkening lineal.

Parameters	Values
M $[M_\odot]$	10 - 14
R_{eq}/R_{pole}	1.154 - 1.1992 - 1.2444 - 1.2896 - 1.3348 - 1.38
R_{pole} $[R_\odot]$	6 - 13
i $^\circ$	30 - 35 - 40 - 45 - 50 - 55 - 60 - 65 - 70
T_{pole} [K]	24500- 25000 - 25500 - 26000

We selected 56 models to compute the average and errors of the parameters based on a change in the slope of the left figure in 6.1, where the blue points represent the 56 models used in this work, and the black points blue points are the first 150 models ordered by χ^2. More studies need to be done to create a reliable criterion for choosing the final models, where most of the models by visual inspection are very similar.

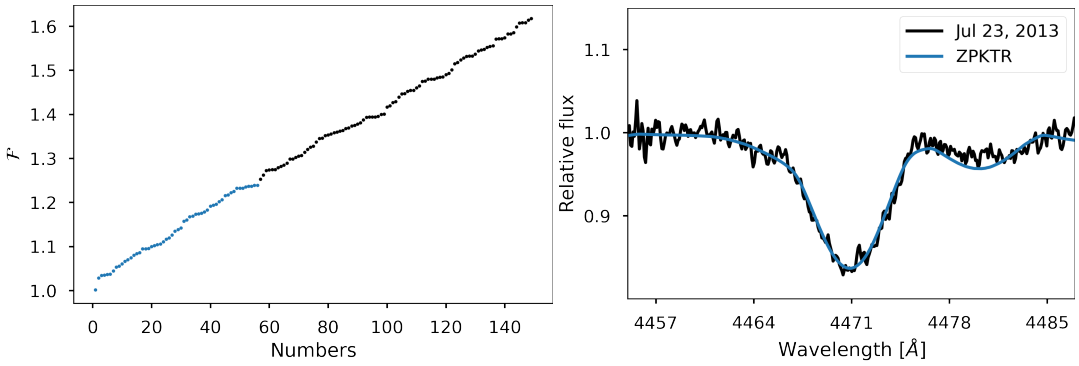

Figure 6.1: *Left Panel:* Figure of merit for all the models created with ZPEKTR. In blue, 56 models were selected to estimate the stellar parameters and their corresponding errors with a $\mathcal{F} <$ 1.25. *Right panel:* The best model with the minimum χ^2 calculated from the HeI 4471 Å line.

Table 6.2 shows the final averaged parameters and the error estimation calculated with ZPEKTR. The information displayed in this table considers all models with a $\mathcal{F} < 1.25$ and therefore represents the best models computed with ZPEKTR.

$< R >$ parameters is an average radius value, considering the stars' oblateness.

Table 6.2: Averaged of the Stellar Parameters obtained with ZPEKTR

M [$M_\odot$]	12.8 ± 1.3
log g	3.90 ± 0.04
$< R >$ [$R_\odot$]	6.74 ± 0.22
R_{pole} [$R_\odot$]	6 ± 1
$T_{\rm eff}$ [K]	23382 ± 616
L [$L_\odot$]	12217 ± 802
T_{pole} [K]	25428 ± 405
R_{eq}/R_{pole}	1.275 ± 0.088
$v \sin i$ [km/s]	282 ± 13
i°	44 ± 6
γ	0.79 ± 0.10
ω	0.93 ± 0.06

The rotation rate W, which is not in the final outcome of ZPEKTR, can be computed with the Eq. (11) from (Rivinius et al., 2013):

$$W = \sqrt{\frac{\gamma^3}{\omega}}, \tag{6.1}$$

and the error associated with W is given by

$$\delta W = \left|\frac{\partial W}{\partial \gamma}\right| \delta\gamma + \left|\frac{\partial W}{\partial \omega}\right| \delta\omega = \frac{3}{2}\sqrt{\frac{\gamma}{\omega}}\delta\gamma + \frac{1}{2}\sqrt{\frac{\gamma^3}{\omega^3}}\delta\omega, \tag{6.2}$$

obtaining a final value for $W = 0.73 \pm 0.16$.

6.2 Overview of the spectral variability

A list of all spectral lines identified in π Aquarii at least in one observation night is presented in Table 6.3. A detailed description of the observed spectral variability from the line list is given.

- **Balmer Lines**:
  Fig. D.3 shows the evolution in time for Hδ. Only four spectra are available covering the wavelength range of Hδ. In 2001, the line presented a deep absorption and non-presence of emission. From 2020 to 2022, a shell-type asymmetric profile appears (i.e., the flux emission arises below the continuum level). We notice

the dominance of the red peak over the violet one. Fig. D.2 shows the evolution in time for Hγ. This spectral line transitions from a deep absorption profile in the first observation that slowly evolves to a Be-shell-type profile over the years. This transition occurred in 2014 at the lowest flux emission of the Hγ line. A double peak emission profile in the last year is observed, with a high asymmetry in the peaks like Hβ. Fig. D.1 shows the evolution in time for Hβ. This line evolved from an absorption profile to a Be-shell type from 2001 to 2008. A fragile Be-shell type is also observed the following year, increasing in intensity towards 2012. From a very low flux, the Be-shell spectral line in 2013 developed a double emission profile over the years with a remarkable asymmetry in the line between 2020 and 2022. While in 2021, V $\gg$ R, in 2022, this changes to V $\ll$ R. Similar behavior to the one described above is also seen in Iron lines. In the case of Hα, a more detailed description is possible thanks to the larger number of spectra. A classic double peak emission profile of a Be star is observed increasing until 2012 when it reaches a maximum and then decreases to its lowest emission in 2014. After that, an increasing emission is observed, but more as a single emission with some peaks, and sometimes also, a third peak is observed in the spectra.

- **Fe II**:
  Fe II lines that come from the multiplet 49: $\lambda\lambda$ FeII 5198 Å, 5235 Å, 5276 Å and 5363 Å, and FeII 5169 Å (multiplet 42) are not present in the spectra of π Aquarii until 2015. After that, a double-peaked emission profile appears in all lines with a V/R $\ll$ 1 in 2022, similar to HeI 5875 Å. The most prominent in terms of intensity, compared to the rest, is the FeII 5316 Å line. FeII 4584 Å line presents an analogous behavior as other lines from the multiple 49, but the double-peaked emission profile is observed in the previous years. FeII 5018 Å line presents a kind of double-peaked emission profile, but it is compromised with the HeI 5015 Å line making it difficult to distinguish. Other FeII lines show low variability in their profiles.

- **He I**:
  The HeI 4388 Å line presents a low variation, usually as a shell-type profile. HeI 4471 Å and MgII 4481 Å always appear in absorption, HeI being stronger than MgII. The HeI 4713 Å line is seen in most dates as an absorption profile, but in some years (2014 to 2106), there is no signal of this line. After this starts to appear again with a small emission in the core of the absorption. HeI 4921 Å

is seen as an absorption line with a variation since 2016, where the line shape is altered compared to the previous years, and emission is arising in the absorption center similar to a DPS profile. The HeI 5047 Å line is difficult to study because of the complex absorption and DPS structure and because its overlaps with the FeII 5018 Å line and can be viewed on all dates. HeI 5875 Å line presents a shell-type profile regularly, with an eye-catching reduction in the V/R ratio originating in 2021 and more clearly seen in 2022. It contributes to the right wing of doublet NaI D2 lines at 5889 Å and 5895 Å. The HeI 6678 Å line is observed until 2014 but then disappears up to 2022, where a slight double-peaked emission profile manifests again. Finally, the HeI 7065 Å line is very similar to the HeI 6678 Å line but in the last years, a more prominent double-peaked emission profile has been seen, with a higher red peak intensity.

- **Other lines**
  Absorption lines always observed in the spectra are MgII 4481 Å and OII 4416 Å lines. Also, OII? 4676 Å line is observed. Other non-identified lines that are strong and in absorption are found around 4650 Å, which could be OII, CIII, or FeII. Silicium lines present low intensity, and 6347 Å presents a double-peaked emission profile in some years.

6.3 Variability on the several lines in π Aquarii

6.3.1 Balmer lines

This section covers getting the final results of the EW, V/R, DPS, and RVs on the Balmer, Iron, Helium, and other lines, which can be found at `https://besos.ifa.uv.cl` in HD 212571 section or directly at online excel file.

EW variability

Several figures (B.1, B.2, B.3, B.4 and B.5) were generated and sorted by observation date to display the intensity changes over the years using the Hα spectral line, that give us information about the formation and dissipation of the disk of π Aquarii. The figures show the wavelength rest as a vertical red dashed line. By looking in detail at the first six profiles (see Fig. B.1), since the emission in 1995, two consecutive

Table 6.3: Observed spectral lines and their variation in π Aquarii spectra

HeI		FeII		Balmer Lines		Other lines	
Line [Å]	Description	Line [Å]	Description	Line [Å]	Description	Line [Å]	Description
4388	⧫	4233	◯	Hδ = 4102	▲	OII = 4253[?]	⧫
4471	⧫	4549[a]	⊗	Hγ = 4340	▲	OII = 4416	⧫
4713	⧫	4584	◯	Hβ = 4861	▲	MgII = 4481	⧫
4921	⧫	4629	⊗	Hα = 6563	•	SiIII = 4552[a]	⊗
5015[a]	•	4667	⊗			SiIII = 4567	⊗
5047	⧫	5018[a]	•			CIII/OII = 4650[?]	⧫
5875	•	5169	◯			TiI/OII = 4675[?]	⧫
6678	○	5198	◯			SiII = 6347[a]	⊗
7065	○	5235	◯			SiII = 6371[a]	⊗
		5276	◯				
		5316	◯				
		5363	◯				
		6249	⊗				
		6369[a]	⊗				
		6385	⊗				

[?] Uncertainty about the element.

[a] Overlapping lines.

Description of each line, ⊗: No signal or sometimes very weak transition between emission and absorption lines, •: Double line emission with variations over the years, ⧫: Line in absorption over the years with some variations, ○: Double peaked the first years (2001-2014), disappeared and formation of the line again in the final years, ▲: Transition between shell-type and double-peaked line emission, ◯: Formation of the double peak line in emission in the final years (2014-2022).

absorption profiles appeared in 2001. Then in August and October of 2001, a Be-shell profile is observed, evolving into a lower flux Be-shell profile the next month. These observations have a low spectral resolution, making it difficult to distinguish the variation in this figure. After this, the following data is from 2004 with a clear double-peaked line profile. The behavior, varying its flux, is observed in the Hα profile for most of the years. Around 2018 (see Fig. B.3, B.4 and B.5)) the shape changed, with a higher intensity in the emission, forming a single emission line where violet and red peaks are not distinguishable, and sometimes a third-like peak appears in the emission. The EW values were obtained for all Hα spectral lines shown in these figures, taking into account the photospheric absorption correction with the synthetic

spectra from the code ZPEKTR.

Fig. 6.2 shows the evolution of the Balmer lines EW in modified Julian Days (hereafter MJD), corresponding from 1995 to 2022. The high increment towards the final years can be related to episodes of enhancement mass-loss rates or outflows. Based on the EW noticeable changes of the Hα line-emission, we chose five specific dates to study with HDUST: Nov 27, 2001 (52230 MJD); Sep 02, 2011 (55790 MJD); Jan 01, 2014 (56650 MJD); Sep 29, 2018 (58380 MJD); and Oct 06, 2022 (59850 MJD). These dates marked a specific change in the size of the emitting region and were used to quantify the disk phases in this work. Table E.1 shows the spectral windows where the EW was measured for Balmer lines.

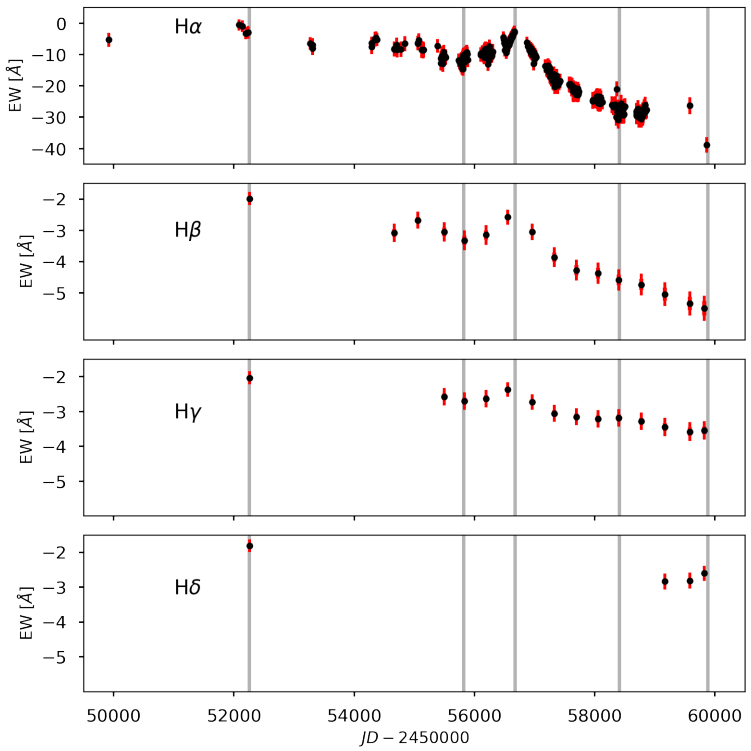

Figure 6.2: EW for all the Balmer lines in units of Å. The bottom axis is in MJD. The red bars represent the measurement error calculated using the Bootstrap method. The vertical gray lines indicate the five disk phases studied with HDUST. Note: The EW y-axis range is larger for Hα than the other lines.

From the plot, the initial value of the EW in Hα is -5.29 Å, then jumps to a lower

intensity profile, with an EW of -0.56 Å. After this, the EW increases to -3 Å, which can be noticed in the first vertical gray line in Fig. 6.2, the first specific date to study with `HDUST`, due to the lack of data before this date in this work, no claims can be made about the growth or dissipation of the disk. Still, in the work of Bjorkman et al. (2002), they reported the lowest brightness level observed in π Aquarii during 1998 and weak emission in Hα , which they refer to as a "quasi-normal star" phase between 1996-2001. The following change that defines the second remarkable date could be associated with a feeding process (since 52000 MJD) of the disk reaching an EW of -14.58 Å, distinguished by the second vertical gray line. Then, the emission decreases monotonically over the following years, reaching an EW value around -3 Å, indicated by a third vertical gray line. This represents a change from the previous phase of the disk that could mean that the mechanism that supplements the mass to the disk is switched off. After this, the emission intensity increased to ~ -40 Å around 60000 MJD in a consistent manner, in which the growth activity of the circumstellar envelope has not stopped during the last few years, reaching more than 13 times the anterior maximum value (-3 Å). This is marked as four and five, respectively, vertical gray lines in the figure. The fourth date was also chosen based on having more information between a low-intensity profile in Hα and a high emission intensity. Furthermore, around this time, a third peak appears in the profile.

On the other hand, the variability of the EW of Hβ and Hγ spectral lines shows a similitude to Hα in all phases. For Hβ, from the third specific date (third gray vertical line), the emission increases monotonically from EW $= -2.6$ to EW $= -5.5$ Å, similar to Hγ but the slope decays slowly in a range between -2.4 to -3.5 Å. For Hδ, we have a few observations in the last three years, and we can observe that the intensity is decreasing in these years from EW = -2.83 Å to -2.6 Å.

Table 6.4 shows the EW of the Hα line for each phase and the ratio regarding the other Balmer lines. It is observed that the ratio amplitude is increasing towards the Hδ line and that the behavior of EW is similar for all the Balmer lines.

RV variability

The RVs for the Balmer lines are plotted in Fig. 6.3. Values range from $\sim$ -80 to 95 km/s for Hα and seem to have a periodical variation. Hβ has its lowest RV = 162

Table 6.4: Comparison between Balmer lines EW for five observation dates. These dates are marked with a vertical gray line in Fig. 6.2. The first row contains the approximate values of Hα EW. The other rows show the ratio between Hα EW and the other Balmer lines.

Dates [MJD]	52230	55790	56650	58380	59850
EW Hα [Å]	-3	-14.8	-2.7	-28	-38
EW Hα/Hβ	1.5	4.48	1.04	6.09	6.91
EW Hα/Hγ	1.5	5.48	1.13	8.75	10.86
EW Hα/Hδ	1.67	-	-	-	14.61

km/s on the 54668 MJD. Then its value rises to 14 km/s, which is observed in the second gray vertical line in the figure. From the second to the fifth gray vertical line, the RV remains almost constant, with an RV deviated from this behavior, with a value of -77 km/s. For Hγ, the RV remains almost constant from the first to the third phase, varying from 2 to 15 km/s. Since then, the RV has changed its behavior, fluctuating between -123 and 183 km/s. For Hδ in the last phase, the RV is always positive and shifts its value from 47 to 19 km/s.

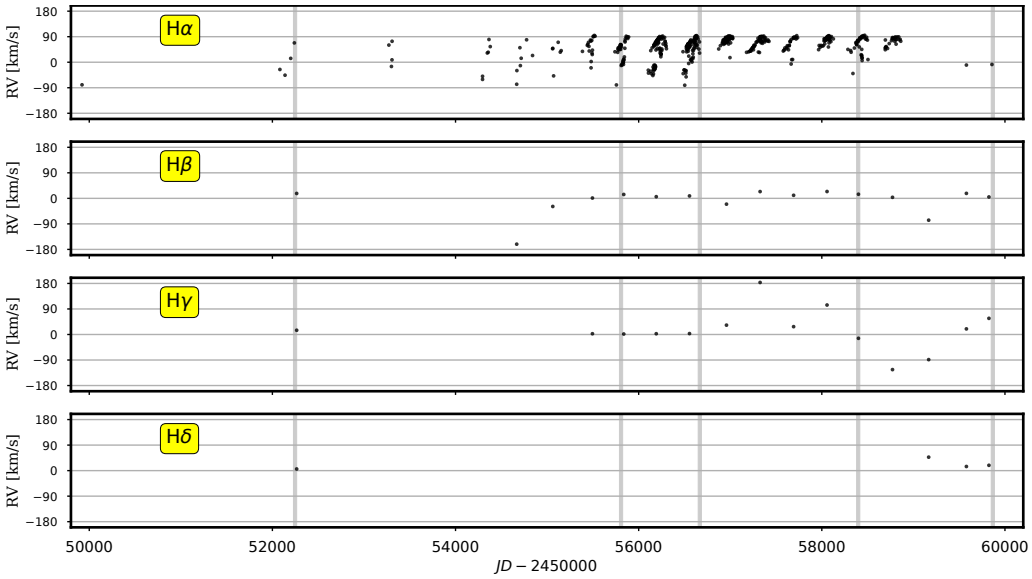

Figure 6.3: RV for the Balmer lines. As described in the methods section, the absorption component of the Hα line is used to compute the RV concerning the wavelength rest. Errors are within five percent of accuracy. Note: The vertical lines represent the five dates selected for the study with `HDUST`, horizontal lines are shown for better discussion of the variability of RV.

V/R variability

The V/R variation for Balmer lines is presented in Fig. 6.4. For Hα and Hβ, the V/R ratio varies from 0.8 to 1.2 approximately. Hγ fluctuates from 0.9 to 1.1 and for Hδ, its ranges from 0.9 to 1.0 (just three data points). In the case of Hβ, Hγ, and Hδ, the data up to the last three observations do not present high variability having an average close to 1.0. For the V/R of Hα, the second and third phases (vertical gray lines) have a symmetrical double peak emission. This is changing from the third vertical line, and the V/R ratio tends to be higher than one up to the last two observations, where this pattern changes drastically to a V/R $<$ 1. Interestingly, the most significant change in the V/R ratio for the other Balmer lines also arises in the final three observations. It changes quickly from a V/R $>$ 1 to a V/R $<$ 1 in two years (see Fig. 6.5).

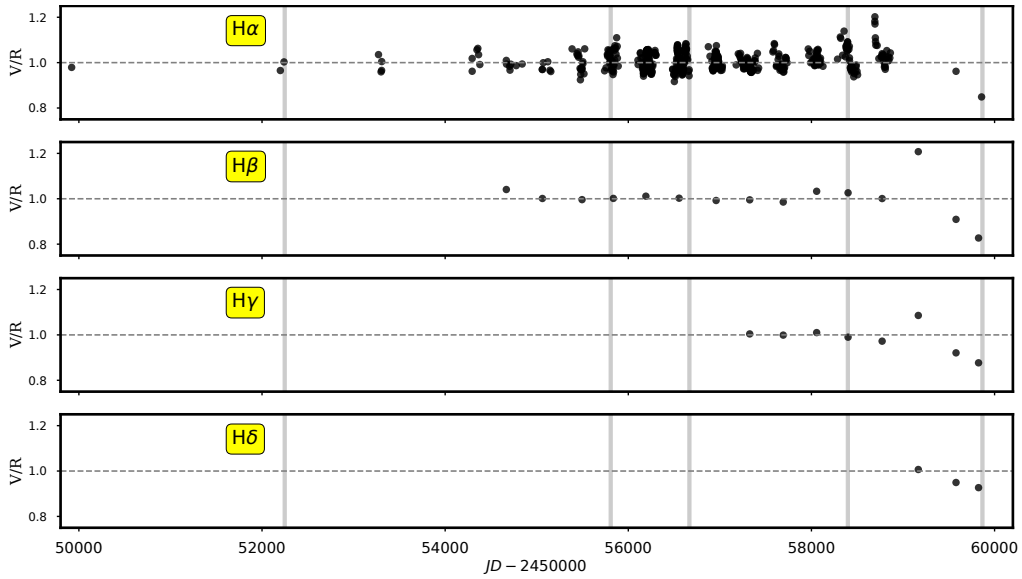

Figure 6.4: V/R ratio for Balmer lines. The horizontal dashed gray line corresponds to a V/R = 1. The error estimation for this measurement is 3%.

DPS variability

The DPS for Balmer lines is displayed in Fig. 6.6. The first DPS is 300 km/s for Hα. The following point is the maximum observed for the Hα line with a value of 555 km/s. After this, the DPS continuously decreases its value until the second phase. From the second to the third phase, the emission of Hα decreases again, and the DPS

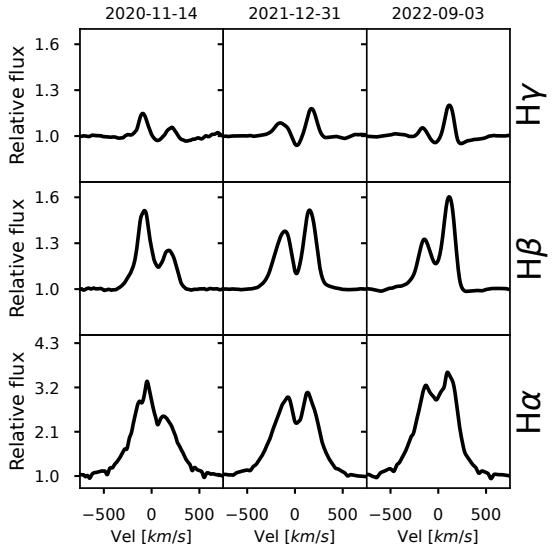

Figure 6.5: V/R ratio for Hα, Hβ and Hγ for the last three years.

remains almost constant at around 300 km/s. The DPS from this phase to the last decays faster, up to its minimum of 102 km/s in the 58440 MJD. The average DPS after this point is 164 km/s. Due to the disk's quasi-Keplerian rotation, higher DPS values are linked to small emitting sizes and vice-versa (Huang, 1972). Therefore, based on Hα measurements, from the third to the last phase, the disk size increased by almost fourteen times its flux and decreased by nearly three times its rotational velocity because of its rotation in a quasi-Keplerian form.

For the other Balmer lines, the maximum DPS encountered is 543 km/s for Hβ in the 56555 MJD, which is very close to the third vertical line, which can be an evolution of the disk, related to a fall in the mass-loss enhancement of the star to the disk. If it is compared for the same date with Hα, with a DPS of 317 km/s, its velocity is about 40 % higher, and the trend after this is downwards up to the last observation, with the last three DPS remains almost constant around 256 km/s. Hγ and Hδ do not share similarly with Hα and Hβ. Hγ remains roughly constant, varying from 280 to 330 km/s, and for Hγ, the DPS is between 319 and 355 km/s in the last three observations. Also, these last points do not show any particular correlation with the last three V/R variations of the Balmer lines.

If the same day is compared for all the lines (59579 MJD), where most of the

spectral lines present a double peak in emission, it is possible to be aware of where the emitting regions are located in the disk for each line. If the DPS is sorted from highest to lowest, the final order is $H\delta > H\gamma > H\beta > H\alpha$, resulting in H$\alpha$ located in the outer part of the circumstellar envelope.

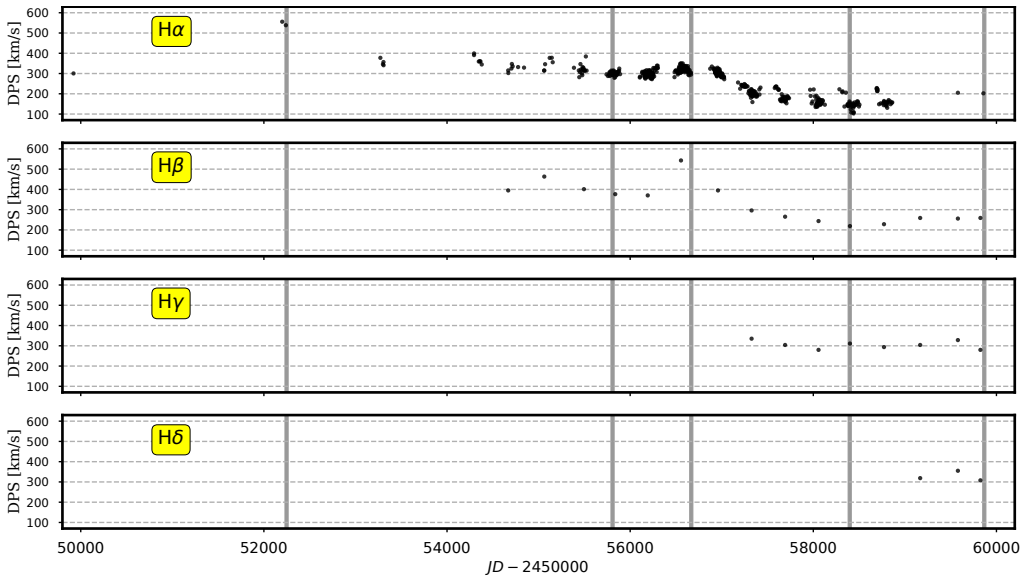

Figure 6.6: DPS for Balmer lines. These values were computed as the difference between the wavelength location at the red and violet peaks. The error estimation for the DPS is within the 12% of accuracy, and the DPS is in km/s units.

LS periodograms of RV and V/R

The LS for the RV of Hα is shown in Fig. 6.7. The higher amplitudes are located at the frequencies 0.00276, 0.0055, and 0.0119 cycles/day, respectively, which gives periods of $\sim$ 361.4, 183.0, and 84.1 days, respectively. It can be noted that the first two correspond to harmonic frequencies, the first one being almost twice the second period. This is observed in the vertical black lines in the left bottom panel of the figure.

The LS periodogram for the V/R ratio of Hα is shown in Fig. 6.8. The left top panel shows the V/R for Hα, while the right top panel displays the power spectrum with the frequency of cycles per day, finding a maximum amplitude of 0.012 cycles/days. The left panel shows the P $= 1/$f , where the best period corresponds to 81.14 days. The other maximum amplitudes are at 0.0092 and 0.015 cycles/days, giving periods

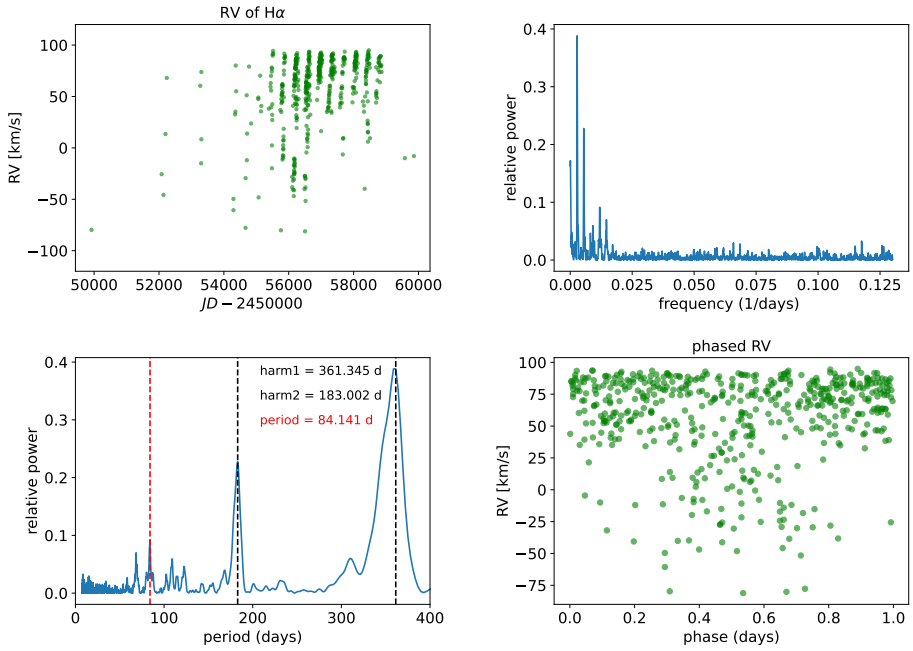

Figure 6.7: *Left top panel:* Evolution of RV with time for Hα. *Top right panel:* Power spectrum in terms of frequency for the RV values. *Left bottom panel:* Power spectrum in terms of days. The vertical red line indicates 84.1 days, while the two harmonics are indicated with a vertical black line. *Right bottom panel:* The phase of the RV computed with the period of 84.1 days.

of $\sim$ 109.1 and 69.7 days, respectively. In the right panel, the phase of the V/R ratio is displayed, calculated with the best period of 81.14 days, viewing a clear sinusoidal form. Zharikov et al. (2013) searched the period of the V/R ratio of Hα using a Discrete Fourier Transform method. The dominant frequency they found in the power spectrum was 0.0119 cycles/days, corresponding to 84.2 days, which agrees with our results. Both results in this thesis, the period of the RV and V/R, concord with the orbital system period of 84.1 days found by Bjorkman et al. (2002).

6.3.2 Iron lines

Due to many Iron lines, all measurements are divided into three groups to discuss the results better. There is no criteria for this choice. Only every five Iron lines a group is

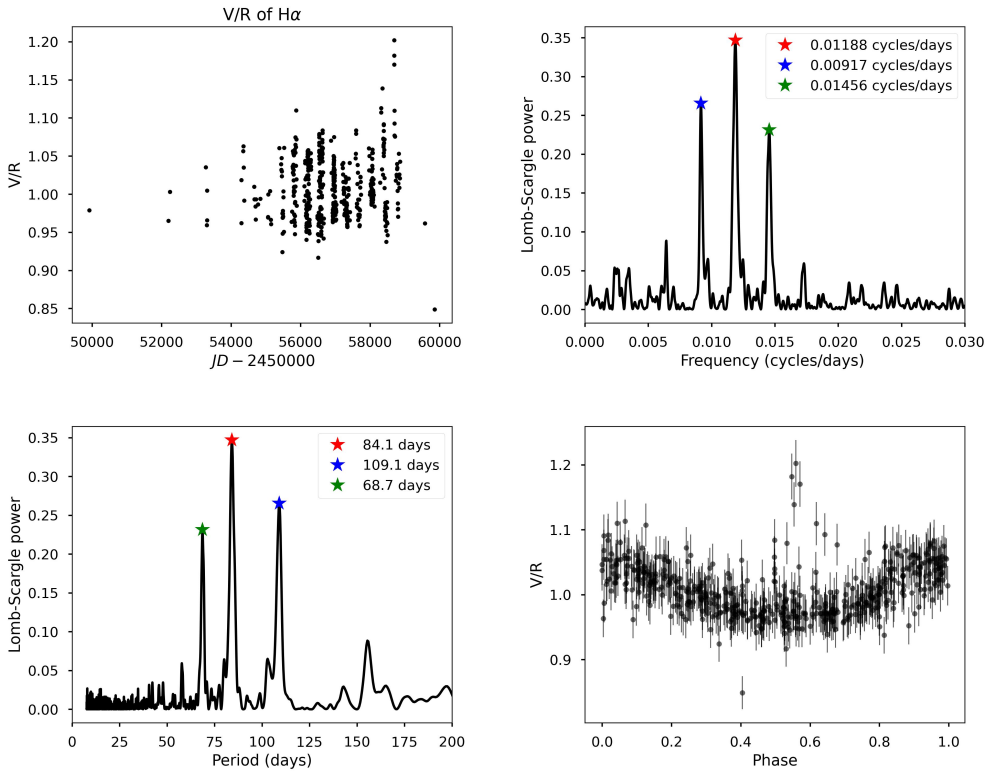

Figure 6.8: *Left top panel:* Evolution of V/R with time for Hα. *Top right panel:* Power spectrum for the V/R ratio variation in units of frequencies. *Left bottom panel:* Periodogram of the V/R variation. The vertical red line indicates 84.1 days. *Bottom right panel:* The phase of the V/R computed with the period of 84.1 days.

formed.

First group

The evolution in time for the spectral profile of the first group of Iron lines is shown in Fig. D.12, D.13, D.14, D.15 and D.16. The spectral windows where the EW is computed for each spectral line are in Table E.2.

The EW range for the first group is between -0.5 and 0.4 Å and is shown in Fig. 6.9. FeII 4242 Å is very noisy for some dates, and a continuum is observed for the first date, indicating an EW close to 0 Å, after this, the EW always remains negative,

indicating the presence of emission in the line. For FeII 4549 Å, the EW is always positive. It makes a transition between a continuum and a small absorption. The highest EW is 0.36 Å, with the most prominent absorption. FeII 4584 Å shows the formation of an emission profile close to the third vertical line, increasing its EW in magnitude to the last observations, very similar to other Iron lines that are described in the second group. FeII 4629 Å and FeII 4667 Å are very weak lines. They do not present either emission or absorption in their profile for some dates, having EW close to 0 Å.

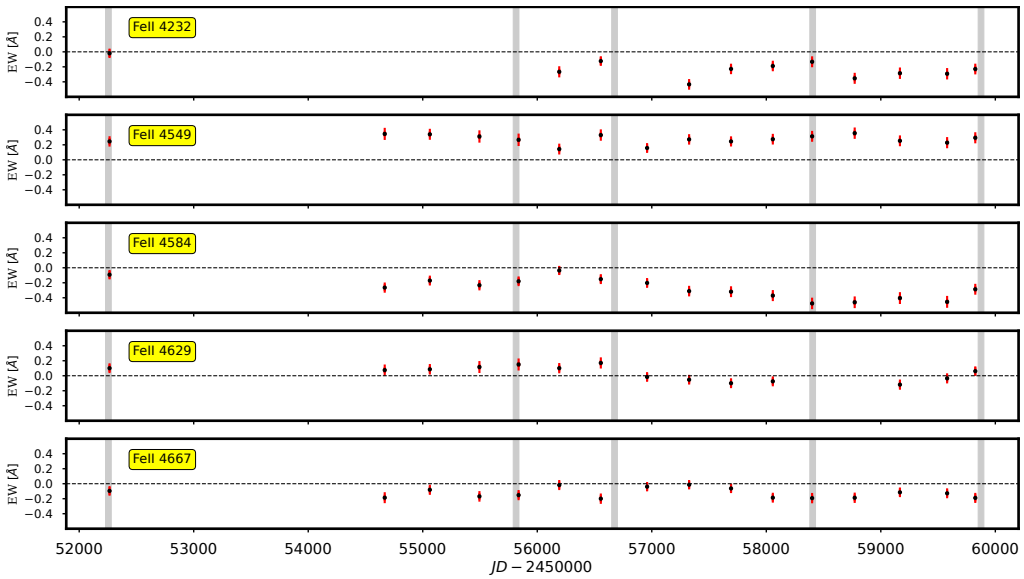

Figure 6.9: EW of the FeII lines. The yellow boxes indicate the wavelength of the analyzed line in Angstrom. Vertical gray lines represent the same dates studied with HDUST for the Balmer lines, and the horizontal dash line represents the transition between absorption and emission profile. We note that not all the Iron lines have the same amount of observations.

Not all the Iron lines exhibited V/R ratio variations over the years. In some lines, a continuum profile or an absorption scheme is observed. In Fig. 6.10, the V/R ratio for the first set of Iron lines is presented. A small variability for the first two lines can be noted, where the values constantly vary around 1 with a maximum amplitude of ~ 0.03. Still, from the half between the third and fourth vertical lines, V/R turns to a lower value of 1. For FeII 4629 and FeII 4667, the V/R is very close to 1. For FeII 5018, the variability is higher. Before the third phase, the V/R is less than 1, and the symmetry of the line begins to change to a V/R > 1 in the last observation.

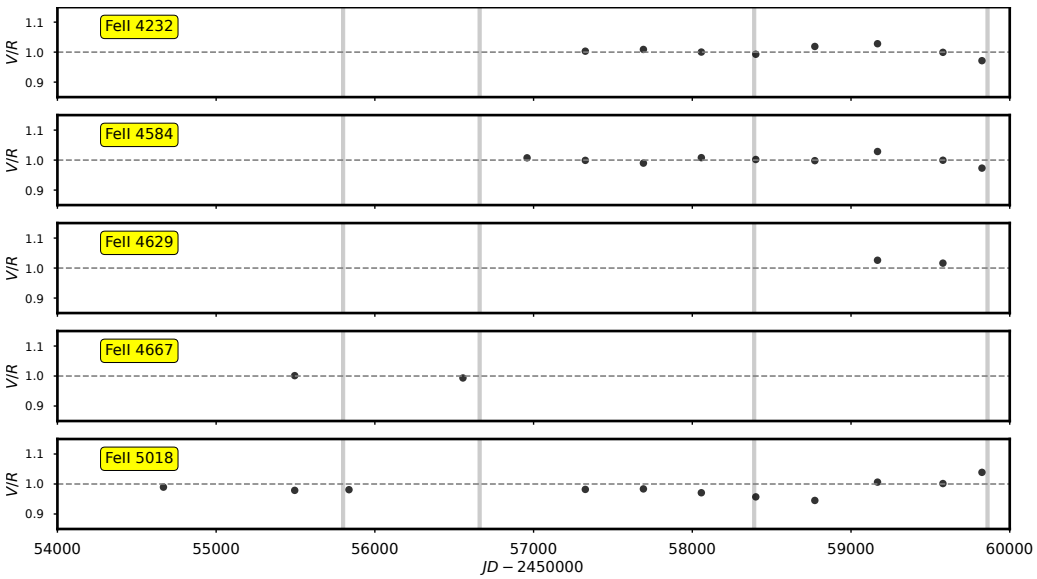

Figure 6.10: Evolution in time of the V/R ratio for the first Iron lines. The yellow boxes indicate the wavelength of the analyzed line in Angstrom. Vertical gray lines represent the same dates studied with `HDUST` for the Balmer lines, but we note this plot only contains from the second to the fifth disk phases.

The DPS for the first group of Iron lines is displayed in Fig. 6.11, where for the first four lines, the DPS varies between 205 and 365 km/s. The more significant difference is encountered for FeII 5018 Å, where the highest DPS is 585 km/s at 55495 MJD, just before the second vertical line. Compared with Hα on the same day, it is almost twice larger. Following this, the DPS continuously drops its value to its minimum of 152 km/s. For FeII 4232 Å and 4584 Å, the DPS decreases since the third phase, and from the fourth vertical line, it remains almost constant with a dispersion of 26 and 20 km/s, respectively.

The RV is shown in Fig. 6.12. The amplitude of velocities is between -25 and 25 km/s for all the lines. For FeII 4232 Å and 4629 FeII 4667 can distinguish a sinusoidal variation in some lines. The other three are not clear.

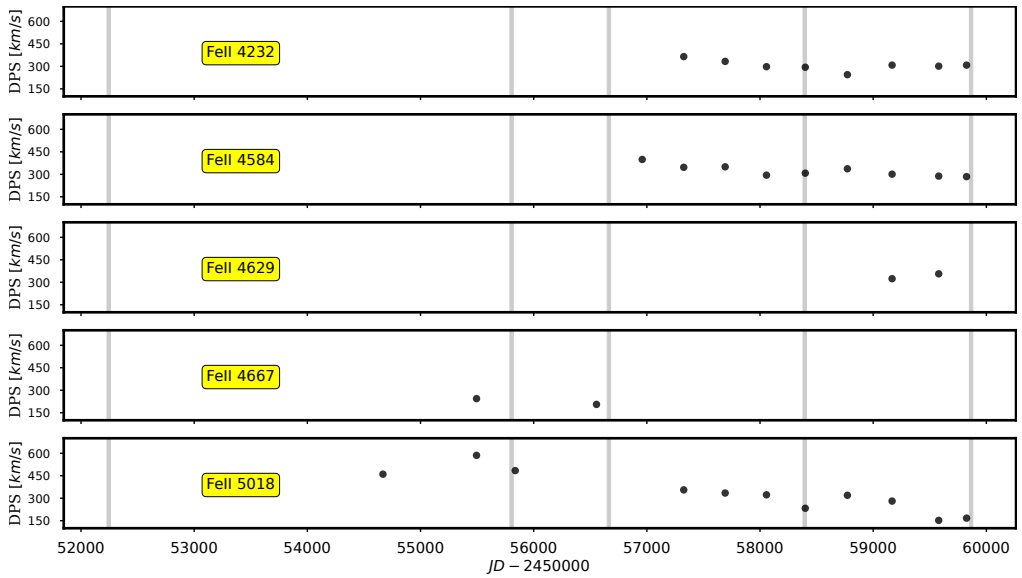

Figure 6.11: Evolution in time of the DPS for the first Iron lines. The yellow boxes indicate the wavelength of the analyzed line in Angstrom. Vertical gray lines represent the same dates studied with HDUST for the Balmer lines.

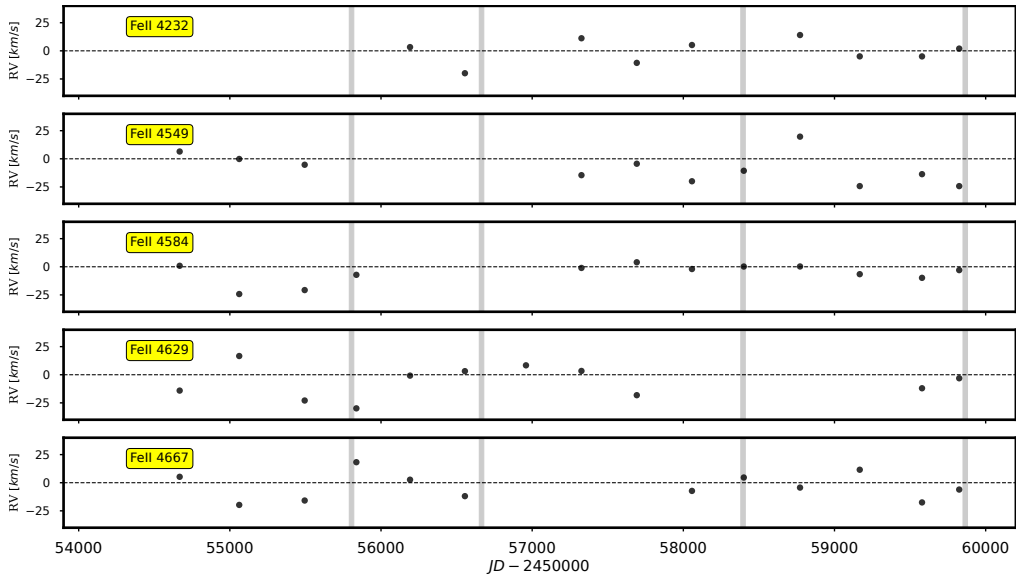

Figure 6.12: RV for the first group of Iron lines. The yellow boxes indicate the wavelength of the analyzed line in Angstrom. Vertical gray lines represent the same dates studied with HDUST for the Balmer lines, but from the second to the last date.

Second group

The evolution of the lines are displayed in Fig. D.17,D.18,D.19,D.20 and D.21. For the second group, the EW ranges from -0.42 to 0.32 Å, which is displayed in Fig. 6.13.

The more prominent emission is seen in FeII 5169 Å, reflected in the EW, getting the maximum of -0.39 Å among these lines. From the third phase, these lines form a double peak line in their profile, raising the value of EW.

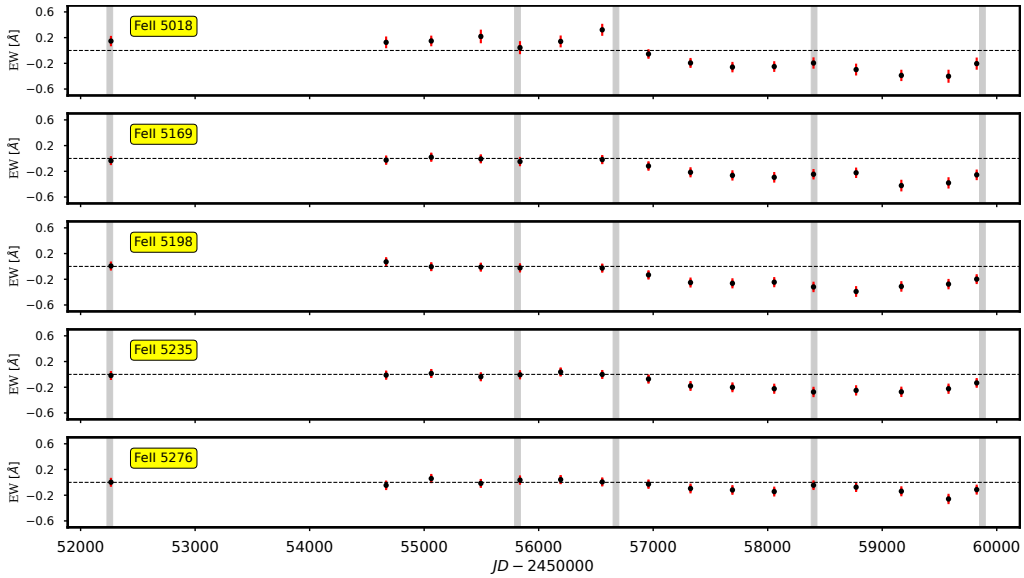

Figure 6.13: Same as Fig. 6.9

The V/R is shown in Fig. 6.14. The distribution of the V/R ratio is well established around 1, defining the symmetry of the lines. This changes in the last three observations, where between both vertical gray lines, the maximum V/R is obtained. For FeII 5235 Å, the highest V/R occurs in the first observation, unlike the other lines. Subsequently, the trend of the V/R changes to < 1, indicating a higher red peak in the DPS. The FeII 5316 Å has the lowest V/R ~ 0.95 at the last observation date.

The DPS of the second group is shown in Fig. 6.15. The only line that observed a continuously decreasing DPS is FeII 5198 Å, going from 372 to 204 km/s. All the other lines have variations between their maximum and minimum peaks. It can be remarked that the highest value for each line occurs in the first observation, with the highest DPS of 412 km/s for FeII 5276 Å. The smallest DPS happens on the last date for the first four lines, except in the last two Iron lines, where this is not appreciated. No line has a similar decrease in the DPS compared to Hα, except for the FeII 5198 Å.

Fig. 6.16 shows the RV of the second group. All lines present variations in the

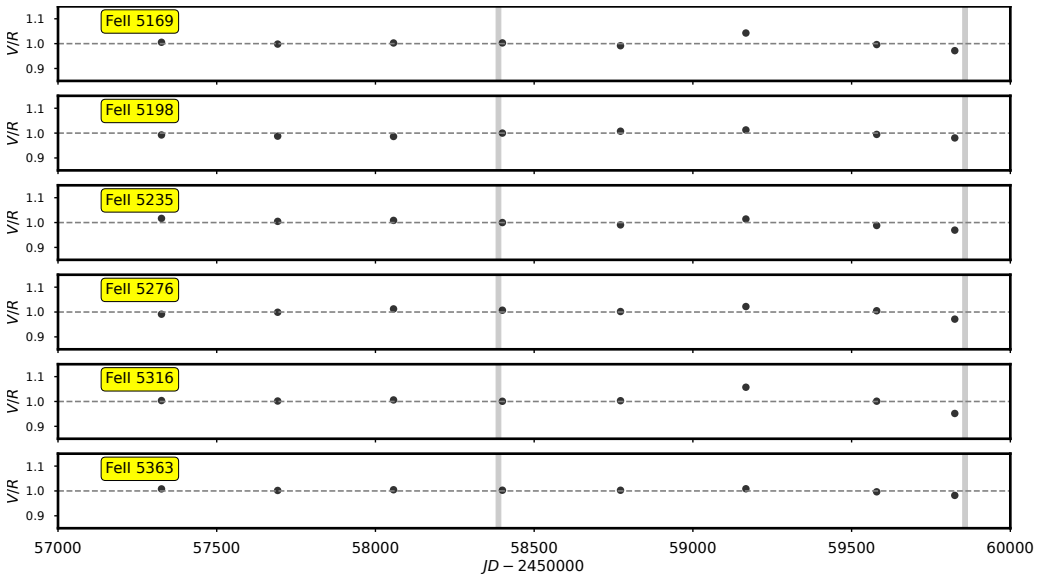

Figure 6.14: Same as Fig. 6.10, but only the last two disk phases are plotted as vertical gray lines.

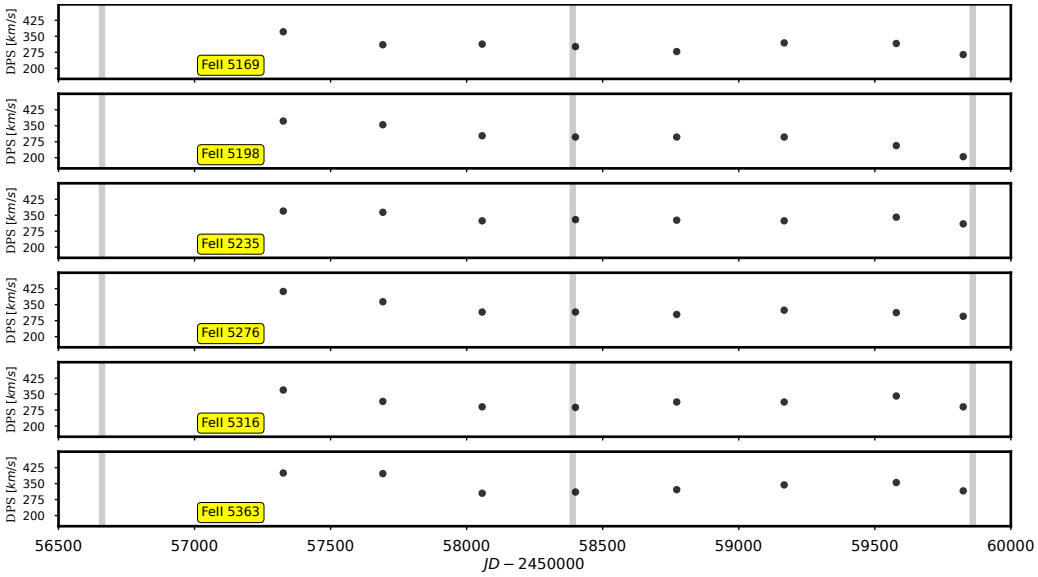

Figure 6.15: Same as Fig. 6.11, but only the last three disk phases are plotted as vertical gray lines.

amplitude of the RV. For FeII 5018 Å, the RV is almost always negative. For FeII 5169 Å, the RVs are very close to 0. FeII 5198 Å seems to have a sinusoidal variation, FeII 5235 Å is almost always positive and close to 0, and FeII 5276 Å varies between 0 and negatives values.

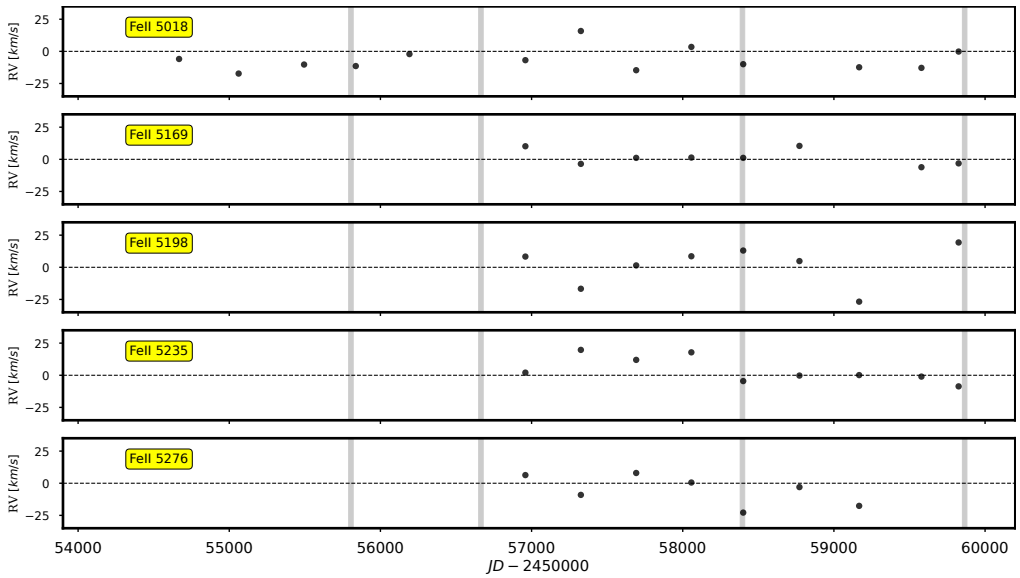

Figure 6.16: Same as Fig. 6.12.

Third group

Fig. 6.17 show the EW for the third set of Iron lines. The more prominent emission is for FeII 5316 Å, getting a maximum EW of -0.57 Å. This line presents a more significant emission than Iron lines from the third phase. The EW of this line and FeII 5363 Å follows the trend of the Balmer and other Iron lines previously discussed. FeII $\lambda\lambda$ 6249, 6369, and 6385 Å are very weak lines, but close to the last phase, a double emission is identified in their profile, where it is obtained the maximum EW for each of these lines.

Fig. 6.18 displayed the V/R ratio variation of the last three Iron lines. FeII 6249 Å have a V/R ratio average of 1, for FeII 6369 Å in both observations the V/R is < 1. Finally, FeII 6385 varies from 1.03 to 0.97 with the final V/R of 1.05.

The DPS is displayed in Fig. 6.19 for the final group. The lowest value is spotted for FeII 6385 Å with a value of 87 km/s. This is the smallest DPS for all the lines in π Aquarii. For FeII 6369 and 6385 Å, the DPS looks like is decaying similar to Hα, but with only two points is difficult to make any further conclusion.

Fig. 6.20 shows the RV for the third group, the amplitude is still between -25 and

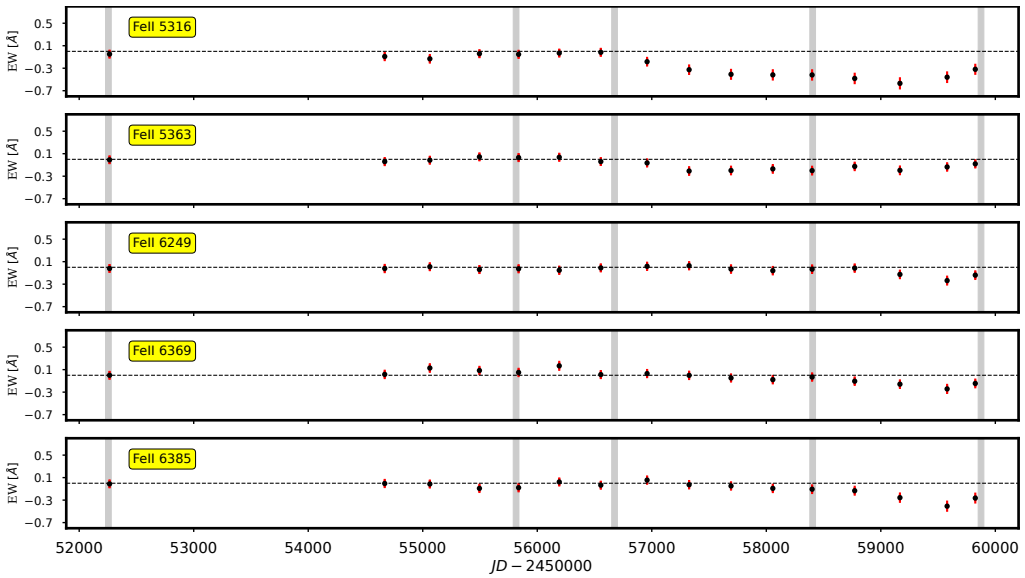

Figure 6.17: Same as Fig. 6.9

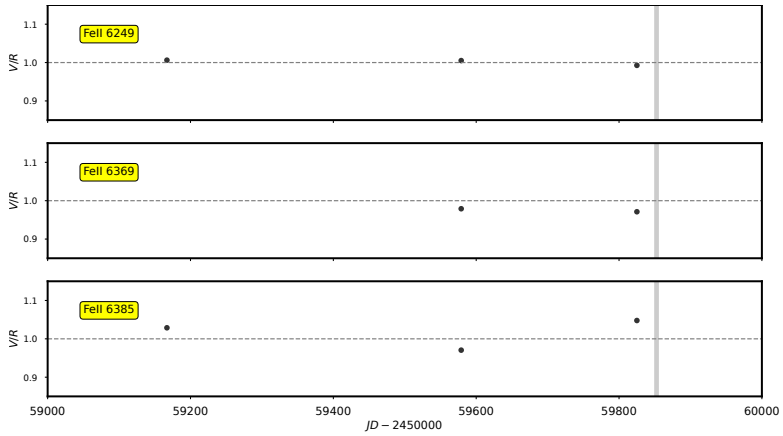

Figure 6.18: Same as Fig. 6.10, but only with the last disk phase indicated as a vertical gray line.

25 km/s. No line shows sinusoidal variation, except without certainty FeII 5276 Å and FeII 6385 Å, where a cyclic variation can be noted.

6.3.3 Helium lines

The EW and RV are displayed in two groups for the Helium lines, and the V/R ratio and DPS are shown in one group. These groups are intended to show the

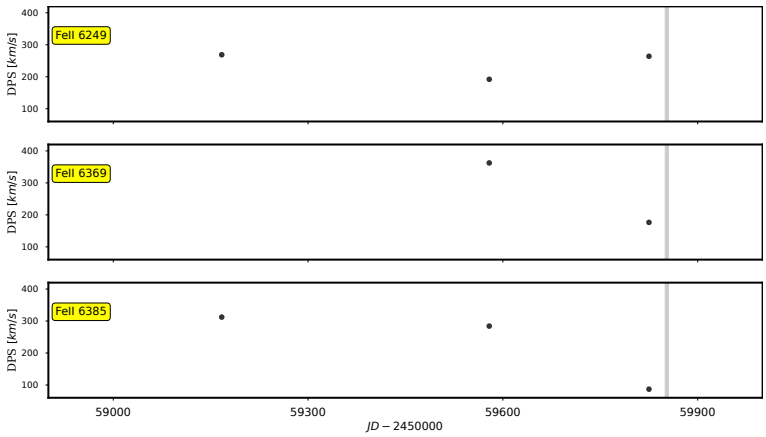

Figure 6.19: Same as Fig. 6.11, the vertical gray line represents the last disk phase of the study with HDUST.

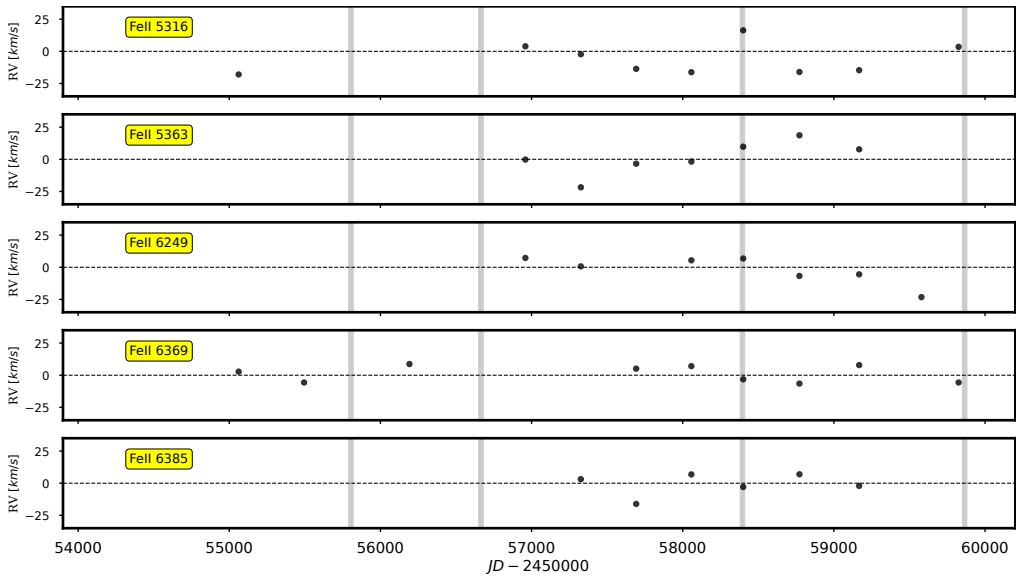

Figure 6.20: Same as Fig. 6.12.

results more clearly. The evolution of the Helium lines are displayed in Fig. D.4,D.5,D.6,D.7,D.8,D.9,D.10 and D.11. The spectral windows where the EW is computed for each spectral line are in Table E.3.

In the first group, almost all lines are in absorption. The EW of HeI 4388 Å is always positive due to absorption for all the dates. This aspect is adverted for the other three lines in Fig. 6.21. The HeI 4471 Å line has the greatest EW in the first

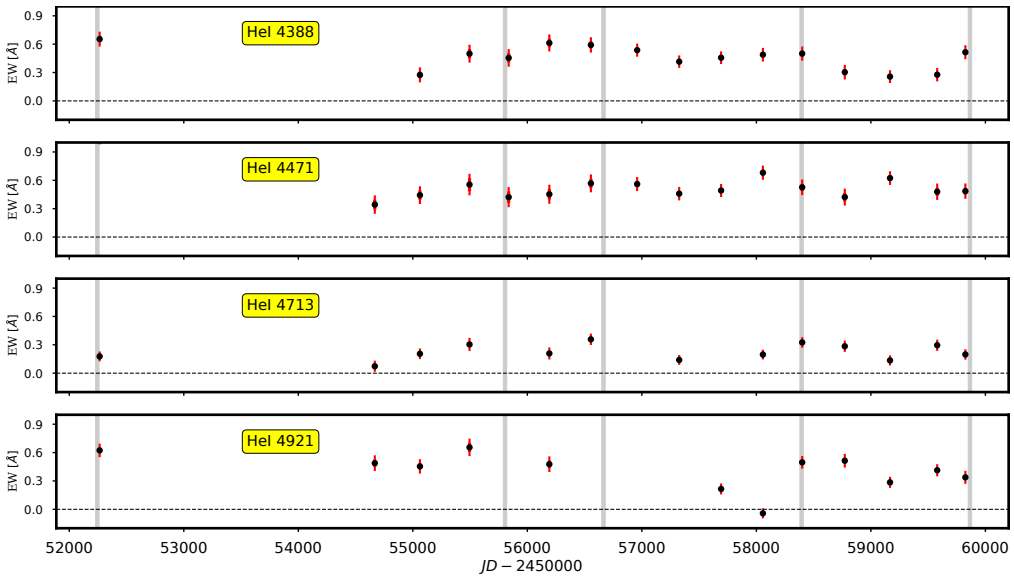

Figure 6.21: Evolution in time of the EW for the first set of Helium lines. The yellow boxes indicate the wavelength of the analyzed line in Angstrom. Vertical gray lines represent the same dates studied with HDUST for the Balmer lines.

vertical line $\sim$ 1Å. After this varies between 0.42 and 0.68 Å, it may be inferred from the figure that this line does not present any correlation with the phases of Hα. This comment is regarding that changes in the photosphere of the star maybe related to the mass-loss mechanism. HeI 4713 Å is a weak line with a relatively small EW. HeI 4921 Å has an EW of $\sim$ 0Å based on a continuum profile observed before the fourth vertical line. No line appears to have a direct correlation with Balmer lines.

The EW for the second group is displayed in Fig. 6.22. This group displays emission in their profiles, and the biggest emission is observed in HeI 7065 Å in his last observation with an EW of -0.73 Å. HeI 5047 Å is always in absorption, and its EW ranges from 0.1 to 0.3 Å. HeI 5875 Å shows cyclical variation in the EW, decreasing from the second to the third phase and increasing the emission from the fourth to the last phase. The EW of HeI 6678 Å has increased since the second vertical line.

Fig 6.23 and 6.24 show the RV for all Helium lines, several lines present variability between -25 and 25 km/s. Again, it is important to remark that RV for lines with a continuum profile is not computed.

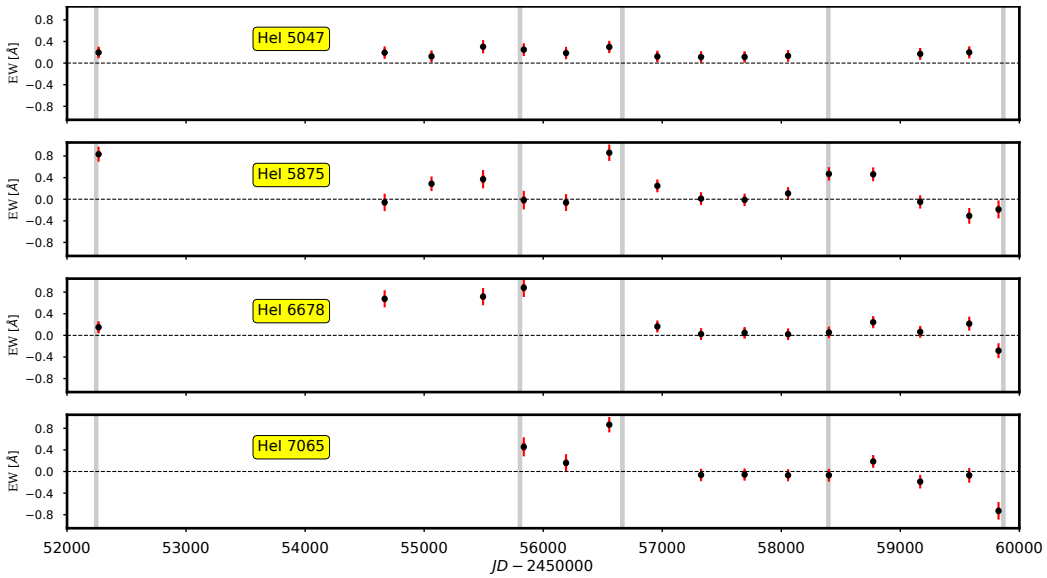

Figure 6.22: Same as Fig. 6.21

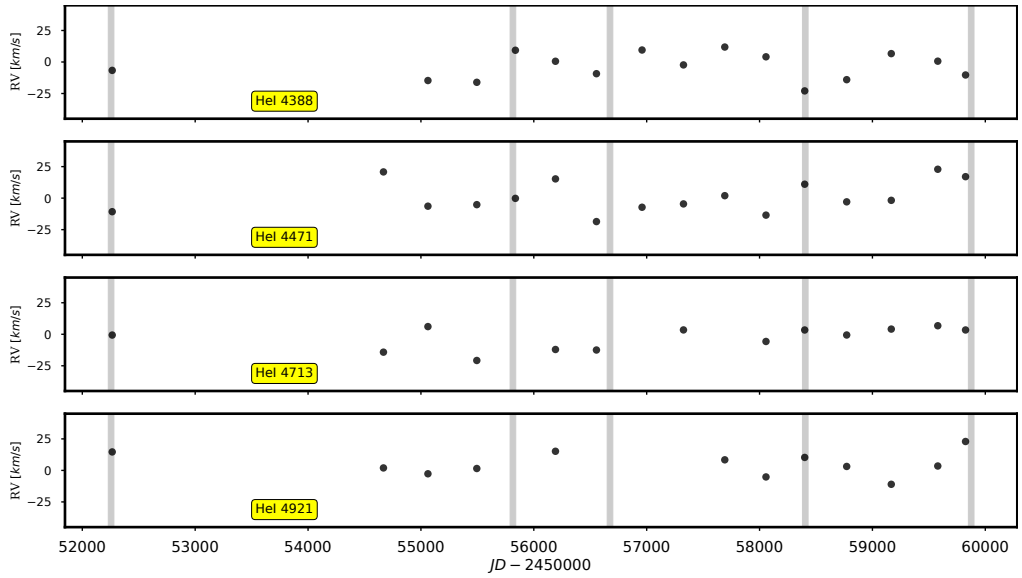

Figure 6.23: RV for the first group of Helium lines. The yellow boxes indicate the wavelength of the analyzed line in Angstrom. Vertical gray lines represent the same dates studied with HDUST for the Balmer lines, but from the second to the last date.

As the majority of Helium lines are in absorption, it was possible to identify a DPS and V/R ratio for a few of them. Fig 6.25 shows the DPS for five Helium lines. HeI 4388 Å has the highest DPS, all above 700 km/s, indicating that the emitting region

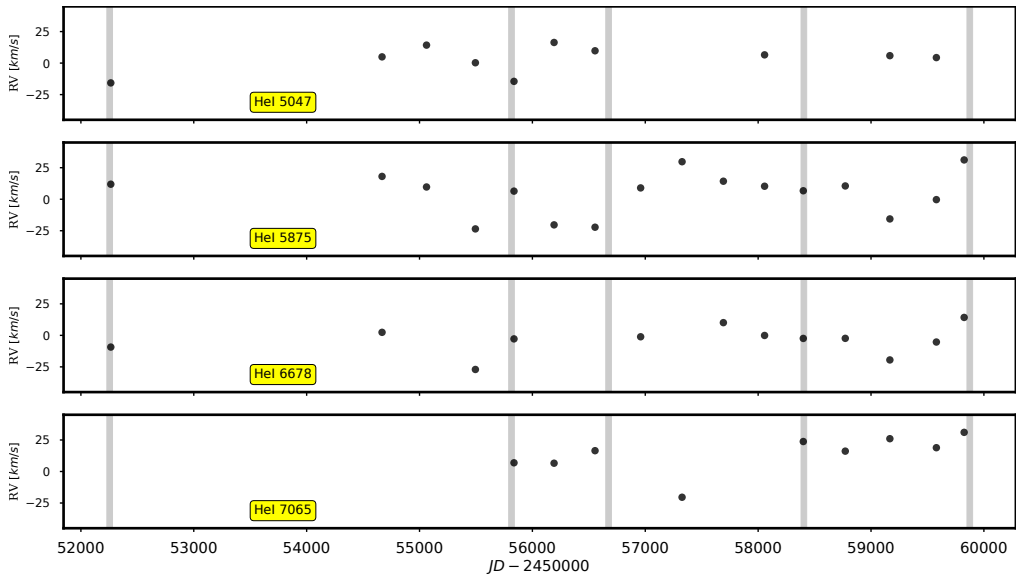

Figure 6.24: Same as Fig. 6.23

of this line may be located in the inner part of the disk. Other Helium lines also have high DPS, for instance, HeI 4713 Å. The V/R variation is seen in Fig. 6.26. All lines manifest a periodical change from a $V/R > 1$ to $V/R < 1$. HeI 5875 Å shows this variation from the first vertical line, which agrees with the Balmer and the Iron lines.

6.3.4 Other lines

This final section presents the calculations on the other possible lines detected in π Aquarii. The EW and RV are presented in two groups for more clarity. The spectral windows where the EW is computed for each spectral line are in Table E.4. The evolution of each line is displayed in Fig. D.27,D.28,D.29, D.30, D.31,D.32,D.33 and D.34..

Fig. 6.27 shows the EW for the first group. OII 4253 and 4416 Å are always in absorption, so the EW is positive in all the dates, with a maximum amplitude of 0.63 Å in the 56192 MJD for the 4253 line and a maximum of 0.49 Å for the OII 4416 Å line in the 55837 MJD. MgII 4481 Å presents an absorption profile in all the dates, with a lower intensity than the previous lines, with a maximum EW of 0.39 Å. Finally SiII? 4567 Å is a very weak line, with low intensity in their profile, and this is reflected in

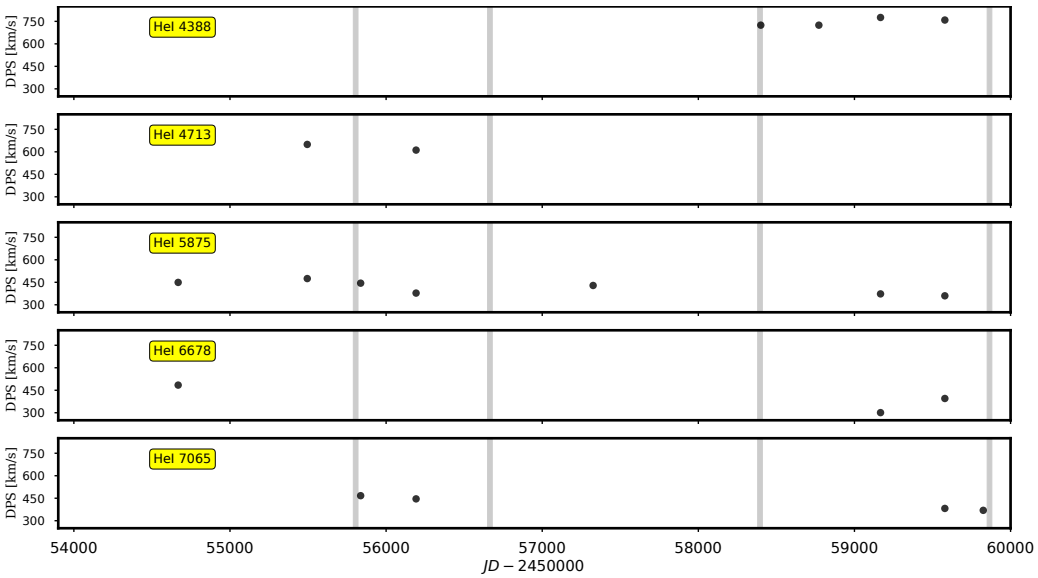

Figure 6.25: Evolution in time of the DPS for Helium lines. The yellow boxes indicate the wavelength of the analyzed line in Angstrom. Vertical gray lines represent the first to the fourth date studied with HDUST for the Balmer lines.

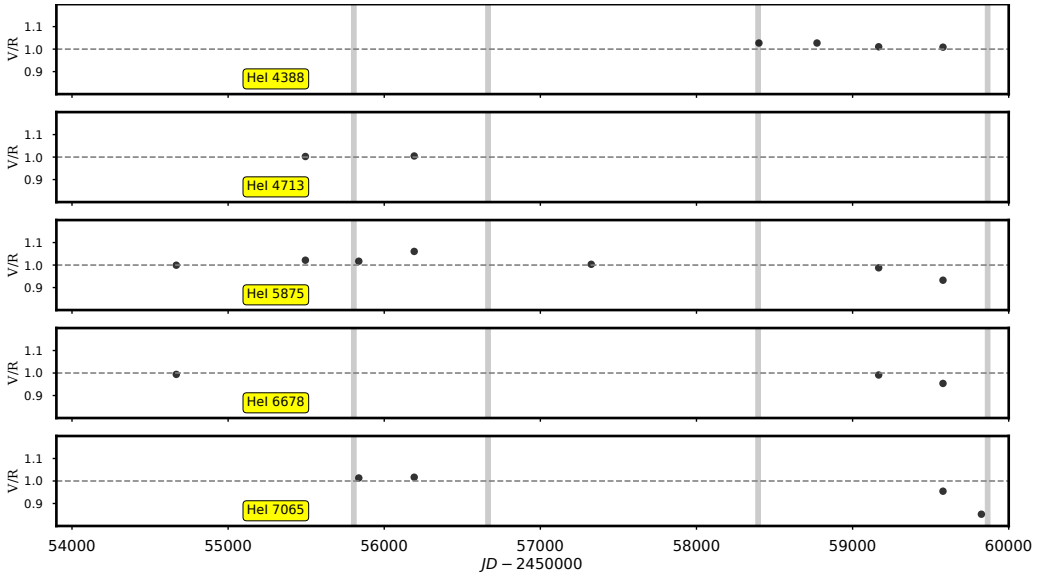

Figure 6.26: Evolution in time of the V/R ratio for Helium lines. The yellow boxes indicate the wavelength of the analyzed line in Angstrom. Vertical gray lines represent the first to the fourth date studied with HDUST for the Balmer lines.

the EW with the highest value of 0.3 Å. None of the lines show similarity with Hα.

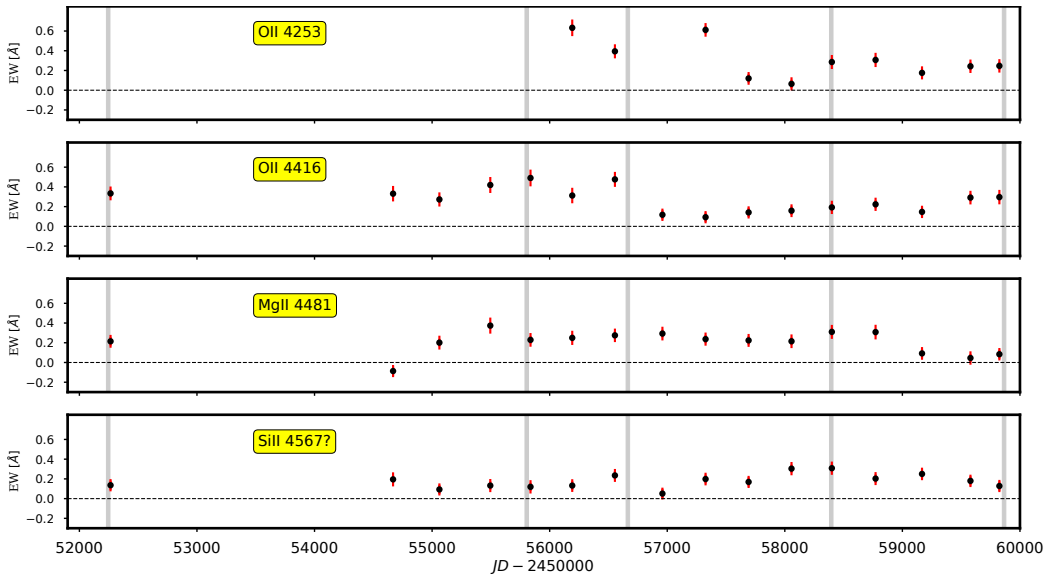

Figure 6.27: Evolution in time of the EW for the first group of other lines. The yellow boxes indicate the wavelength of the analyzed line in Angstrom. Vertical gray lines represent the same dates studied with HDUST for the Balmer lines.

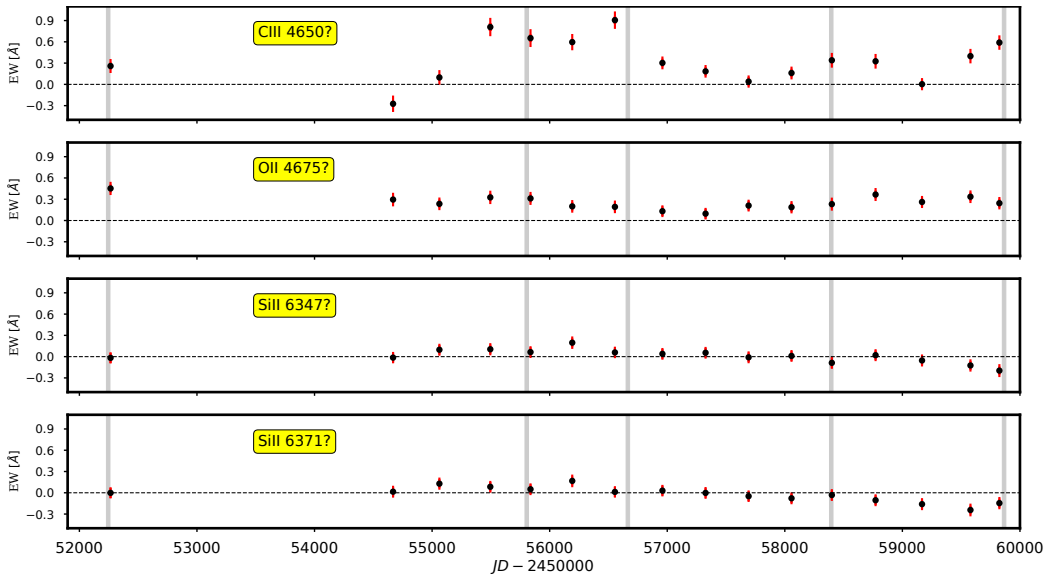

Figure 6.28: Same as Fig. 6.27

Fig. 6.28 shows the EW for the second group. CIII? 4650 Å is variable over the years. This is observed in their EW, where the greatest is 0.91 Å in the 56555 MJD. The EW begins to decrease from the third vertical line, similar to Hα. For OII 4675

Å, the EW remains positive for all the dates, and for both possible Silicium line, EW varies from -0.24 to 0.2 Å showing some weak double emission profile in the last observations.

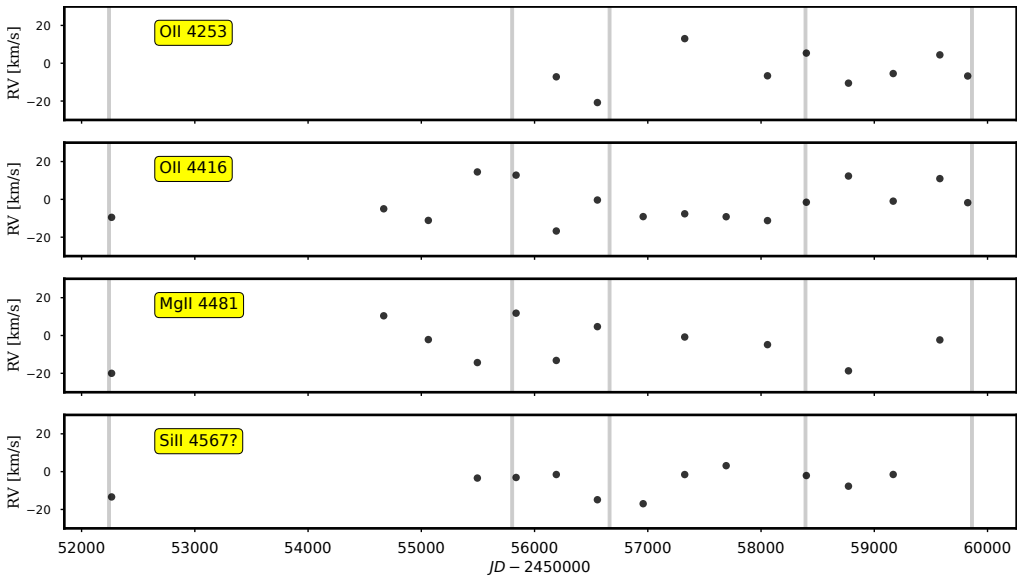

Figure 6.29: Evolution in time of the RV for the first group of other lines. The yellow boxes indicate the wavelength of the analyzed line in Angstrom. Vertical gray lines represent the same dates studied with `HDUST` for the Balmer lines.

RV for all other lines are displayed in Fig. 6.29 and 6.30. The RV varies between -20 and 20 km/s for all observations. At first sight, OII 4416 Å and MgII 4481 Å present more variability than other lines. None of these lines reach the values of the Balmer lines and present different behaviors with them.

It was only possible to compute the V/R ratio and DPS for SiII 6347 Å and SiII 6371 Å in their last two observations. This is shown in Fig. 6.31. Both lines have V/R < 1, similar to the Balmer and Iron lines. The DPS drops from 373 to 271 km/s for the 6347 line and the 6371 decays from 362 to 176 km/s.

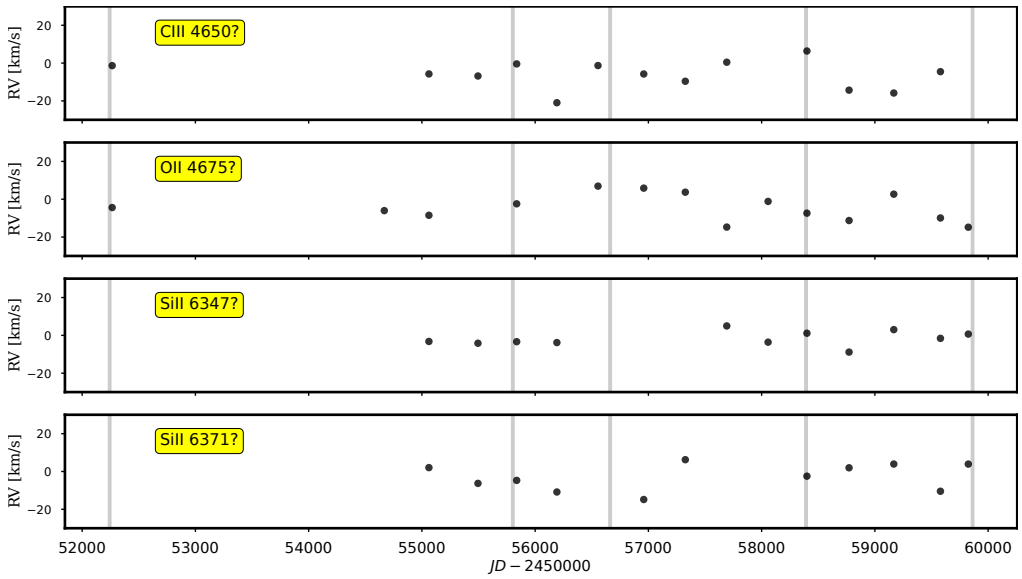

Figure 6.30: Same as Fig. 6.29

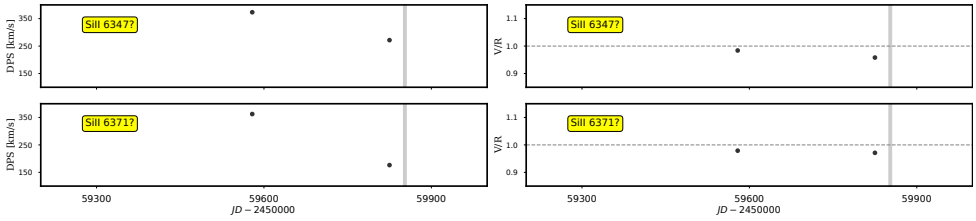

Figure 6.31: *Left Panel:* The DPS for both Silicium lines. The yellow boxes indicate the wavelength of the analyzed line in Angstrom. The last disk phase is indicated with a vertical gray line. *Rigth Panel:* V/R for both spectral lines. The yellow boxes indicate the wavelength of the analyzed line in Angstrom. The last disk phase is indicated with a vertical gray line.

6.4 Disk parameters of π Aquarii

A small grid of 700 models roughly was computed with `HDUST` where the SED and the profile of Hα, Hβ, Hγ, and Hδ are modeled, using the parameters in Table 5.1. Non-coherent electron scattering is not considered in `HDUST`. This process affects the form of the line widening the wings (Hummel & Dachs, 1992). To approximate this effect, a fraction f_e of the total flux computed with `HDUST` is scattered by electrons with thermal velocities v_e, and this new flux distribution has a Gaussian profile with the form.

$$F_{new}(\lambda) = (1 - f_e)F_{nc}\lambda + f_e \times F_c(\lambda), \tag{6.3}$$

where F_{nc} is the non-convolved line profile computed by `HDUST` and F_c is the

convolution between the non-convolved profile concerning a Gaussian profile with full-width half maximum (FWHM) of the velocity of electron (v_e). This effect is observed in our sample, especially on the last three dates chosen for comparison with HDUST , which as a reminder, are: Nov 27, 2001; Sep 02, 2011; Jan 01, 2014; Sep 29, 2018; and Oct 06, 2022.

We used the best parameters obtained with the code ZPKTER to compute the best models of HDUST for the five selected dates. The χ^2 test is used between the models, and the observations were performed to pick the best models, and then if necessary, the convolution using Eq. 6.3 is utilized where f_e ranged from 0.2 to 0.4, and v_e ranged from 250 to 650 km/s (Marr et al., 2021, 2022). When the best model is selected for each date for Hα, the same parameters as input of HDUST are used to run models for Hβ and Hγ.

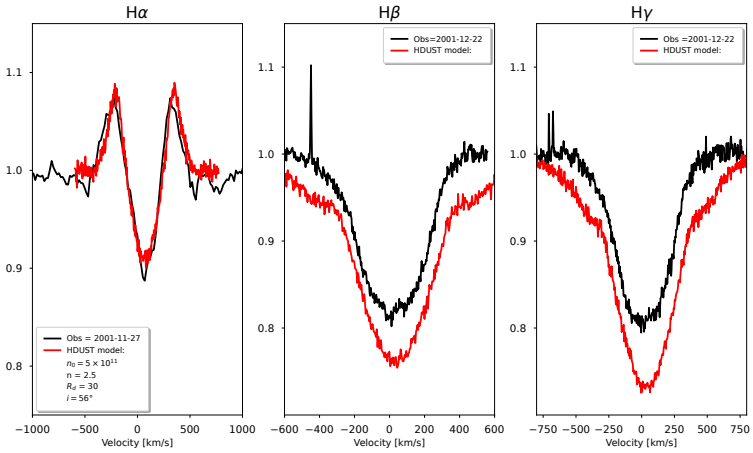

Figure 6.32: A comparison for the same date: Nov 27, 2001, representing the first phase for Hα. In black is the observation for Hα (*Left*), Hβ (*Center*) and Hγ (*Rigth*), in red the best-fit model spectra of HDUST .

For the first phase selected of Hα, the first 29 models have a $\chi^2 < 1$, with the best-fit model having a $\chi^2 = 0.09$ and an EW of -3.07 Å, 3.72 % greater than the Hα profile. The EW of the model is computed in the same way as the observation, subtracting the contribution of the stellar photosphere with the same ZPKETR model. This is displayed with the solid red line on the left panel in Fig. 6.32. For this date,

many of the models are very similar to each other, with the first ten models, ordered by χ^2, having a $\rho_0 = 5 \times 10^{-13}$ [gcm^{-3}], n is equal to 2.5, R_d is either 30 or 50 $R_\star$ and the inclination range is between 48-64°. For Hβ and Hγ, the best-fit models have a χ^2 of 0.46 and 0.72 with the same parameters used for Hα. This is shown in the center and right panels of the figure. These observations are 25 days apart from the Hα profile. No data is found in the sample between this time interval to illustrate how the Hα profile varies these days and how the disk parameters changed in this period. Consequently, the parameters found for this date are as follows: $n_0 = 5 \times 10^{11}$ [cm^3]; $\rho_0 = 5 \times 10^{-13}$ [gcm^{-3}]; $n = 2.5$; $R_d = 30\,R_\star$; $i = 56°$.

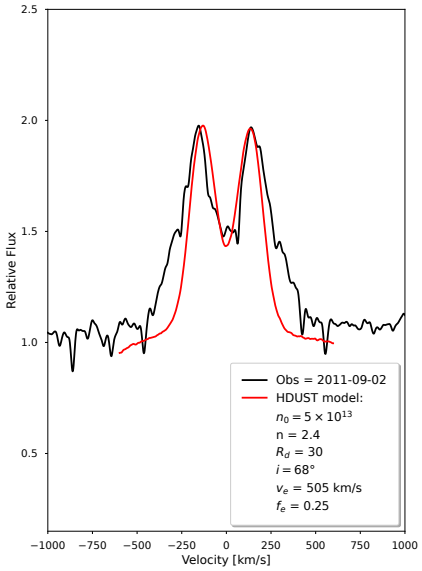

Figure 6.33: A comparison of the Sep 02, 2011 Hα observation in black with the best-fit model spectra of HDUST in red, a f_e of 0.2 of the flux was convolved with v_e of 350 km/s to broadened the profile computed by HDUST .

For the second phase (56650 MJD), the best-fit model of HDUST is shown in Fig. 6.33. It can not reproduce the wings of the Hα profile. Still, the double peak and the central absorption of the profile is well fitted with the model having a $\chi^2 = 23.39$, which is not the lowest, but compared with the other models, is the best reproducing the Hα observation. The EW of the model is -11.39 Å, which, compared to the observed line, is 21.8 % lower. The base density ρ_0 increases to a

higher value of 5×10^{-11} [gcm^{-3}] compared to the previous phase, n has a lower value of 2.4 and R_d is equals to 30 $R_\star$. The range of inclinations i is from 68 to 75°, with the best model having a i equals 68°. Using Eq. 6.3 to account for the non-coherent electron scattering in this model, a fraction of 0.25 of the final flux of the HDUST profile was convolved with a v_e of 505 km/s which was choose by a $\chi^2 = 17.03$.

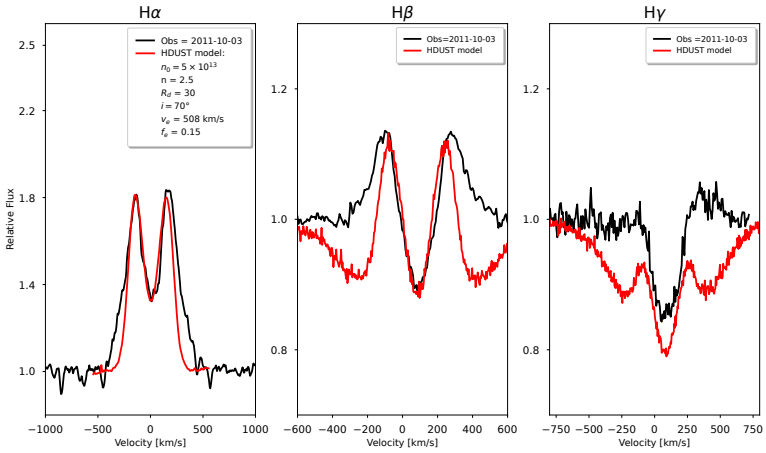

Figure 6.34: HDUST models for the observed spectrum on Oct 3, 2011 (in black) for Hα (*Left*), Hβ (*Center*) and Hγ (*Rigth*) with the best-fit model spectra of HDUST in red. For Hα, a f_e of 0.15 of the HDUST flux was convolved with v_e of 508 km/s to broaden the profile. Note: Hβ and Hγ have different y-axis range compared to Hα.

For Hβ and Hγ, the closest observations are one month apart approximately concerning Hα. In this period, the Hα emission intensity decreases, dropping the EW from -14.57 to -11.36 Å, so the same parameters for the disk are not used for these lines. Unlike the previous phase, there is an observation for Hα on the same day as Hβ and Hγ, shown in Fig. 6.34. This gives us information on how the parameters of the disk can change over a month. The parameter that did change was the n quantity, increasing from 2.4 to 2.5, and the i is very similar, switching from 68 to 70 °. The χ^2 for the best-fit models of Hα, Hβ, and Hγ are 11.36, 1.39, and 1.33 for this date. Suppose we compare the EW for each spectral line with the HDUST models, for Hα, the emission increases with the EW changing from -11.4 to -9.6 Å. For Hβ, the emission declines with an EW going from -3.3 to -3.0 Å, and finally, for Hγ, the EW drops from -2.7 to -2.5 Å, meaning that the emission is lower. Using Eq. 6.3 to account for the non-

coherent electron scattering in this model, a fraction f_e of 0.15 of the final flux of the HDUST profile was convolved with a v_e of 508 km/s which was chosen by a $\chi^2 = 10.01$.

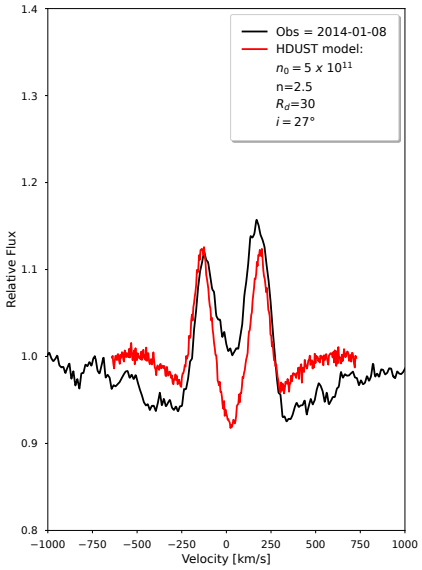

Figure 6.35: HDUST best model (in red) for the observed Hα emission line (in black) on Jan 01, 2014.

For the third phase, a Be-shell profile is observed for Hα, and the best-fit model is in red in Fig. 6.35. The model has a $\chi^2 = 1.12$ and EW equals -3.11 Å, which is 7% bigger compared to the EW of the Hα observation. For this date, it was unfeasible to fit the core of the double peak emission, also with the continuum of the observation below the model, while both wings are well fitted with a lower intensity of the model in the red peak, which is attributed to the asymmetry in the V/R ratio. Similar to the first phase, the models are very similar, and for the first ten models, the density is 5.01×10^{-13} [gcm^{-3}] and n is equal to 2.5, the inclination range varies from 27-43°, and the R_d is either 30 or 50 R$\star$. Over three years, the disk parameters have changed to n_0=5$\times$10^{11}, n=2.5, and i=27°, and the truncation disk radius remains the same.

As in the previous phase, for the Hα observation, there is no match with the day with both Hβ and Hγ spectral lines. We must advance nine months to obtain the three lines with one day of difference. Fig. 6.36 shows the observations and models

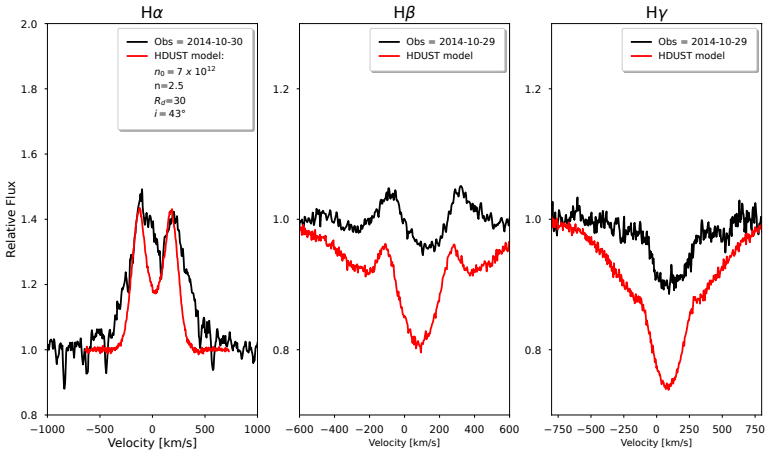

Figure 6.36: Best HDUST model for the observed spectrum on Oct 30, 2014 (in black) for Hα (*Left*), Hβ (*Center*) and Hγ (*Rigth*) with the best-fit model spectra of HDUST in red. Note: Hβ and Hγ have different y-axis range compared to Hα.

for the Balmer lines. Hα emission extends its double peak intensity, going from an EW of -2.9 to -8.7 Å with the best model having a $\chi^2 = 2.56$ and EW equals to -11.36 Å, which reproduces the intensity of the double peak emission. Still, the absorption and wings are difficult to fit with the model. The HDUST models for Hβ and Hγ have a χ^2 of 1.07 and 0.92, respectively, with an EW of -3.01 and -2.47 Å, which are 4.14 and 9.52 % lower in flux compared to the observations.

For the fourth and five phases, the emission intensity is much bigger than in the previous phases. The models are unreliable, reaching a maximum of 250 km/s when the observations reach velocities in 1000 km/s. For the fourth phase in Fig. 6.37, the best HDUST model has a $\chi^2 = 100.13$, which is very big compared to the last phases studied with this code. The model has an EW of -16.68Å, which is 41.6 % smaller concerning the observation. It was possible to match this model with the Hβ and Hγ profiles six days apart. The EW for Hβ and Hγ are -5.81 and -3.38 Å.

For the final phase of the study, as in the previous phase, the wings of the Hα profile are not fitted by the HDUST model, obtaining a high value for the $\chi^2 = 249.88$ and EW of -23.76 Å. In this occasion, Hβ, Hγ, and Hδ are also shown in Fig. 6.38. These observations are one month before the Hα observations in which there is no

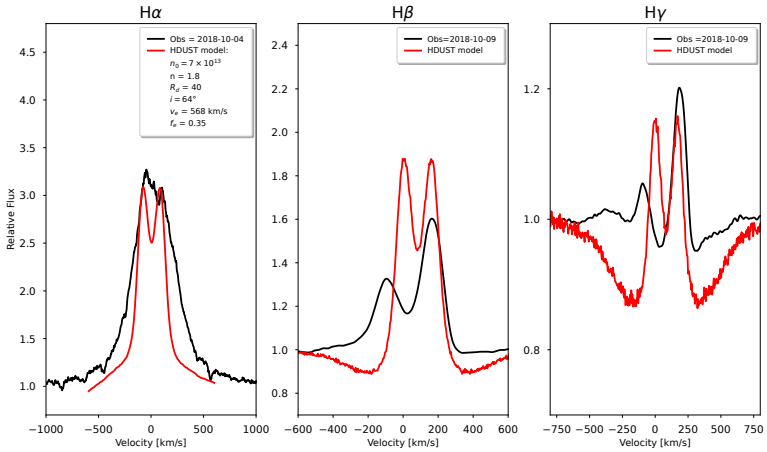

Figure 6.37: Best HDUST model (in red) for the observed spectrum on Oct 4, 2018 (in black) for Hα (*Left*), Hβ (*Center*) and Hγ (*Rigth*). For Hα, a f_e of 0.35 of the flux was convolved with v_e of 568 km/s to broaden the profile computed by HDUST. Note: Hβ and Hγ have different y-axis range compared to Hα.

data of Hα, but according to the behavior, the EW is increasing slowly. The EW of each model is -5.81, -3.37, and -3.47 Å, respectively.

Figure 6.39 shows the Hα, Hβ and Hγ, the disk temperature profiles, and the visible, IR, SEDs of the HDUST profiles for each phase of the study. Table 6.5 shows all the results obtained with HDUST in the phases of study and two more dates.

Date	ρ_0 [gcm^{-3}]	n	R_d [$R_\star$]	i°	χ^2
2001-12-22	5×10^{-13}	2.5	30	64	0.09
2011-09-02	5.01×10^{-11}	2.4	30	68	23.39
2011-10-03	5.01×10^{-11}	2.5	30	70	11.36
2014-01-08	5.01×10^{-11}	2.5	30	27	1.12
2014-10-30	7.01×10^{-12}	2.5	30	43	2.56
2018-09-29	7.01×10^{-11}	1.8	40	64	100.13
2022-10-06	5.01×10^{-11}	1.5	40	64	249.88

Table 6.5: Final results for the disk parameters of π Aquarii for each expected date (red) for the study with HDUST. In black are the dates that do not correspond to a phase but are selected to analyze the behavior of the other lines.

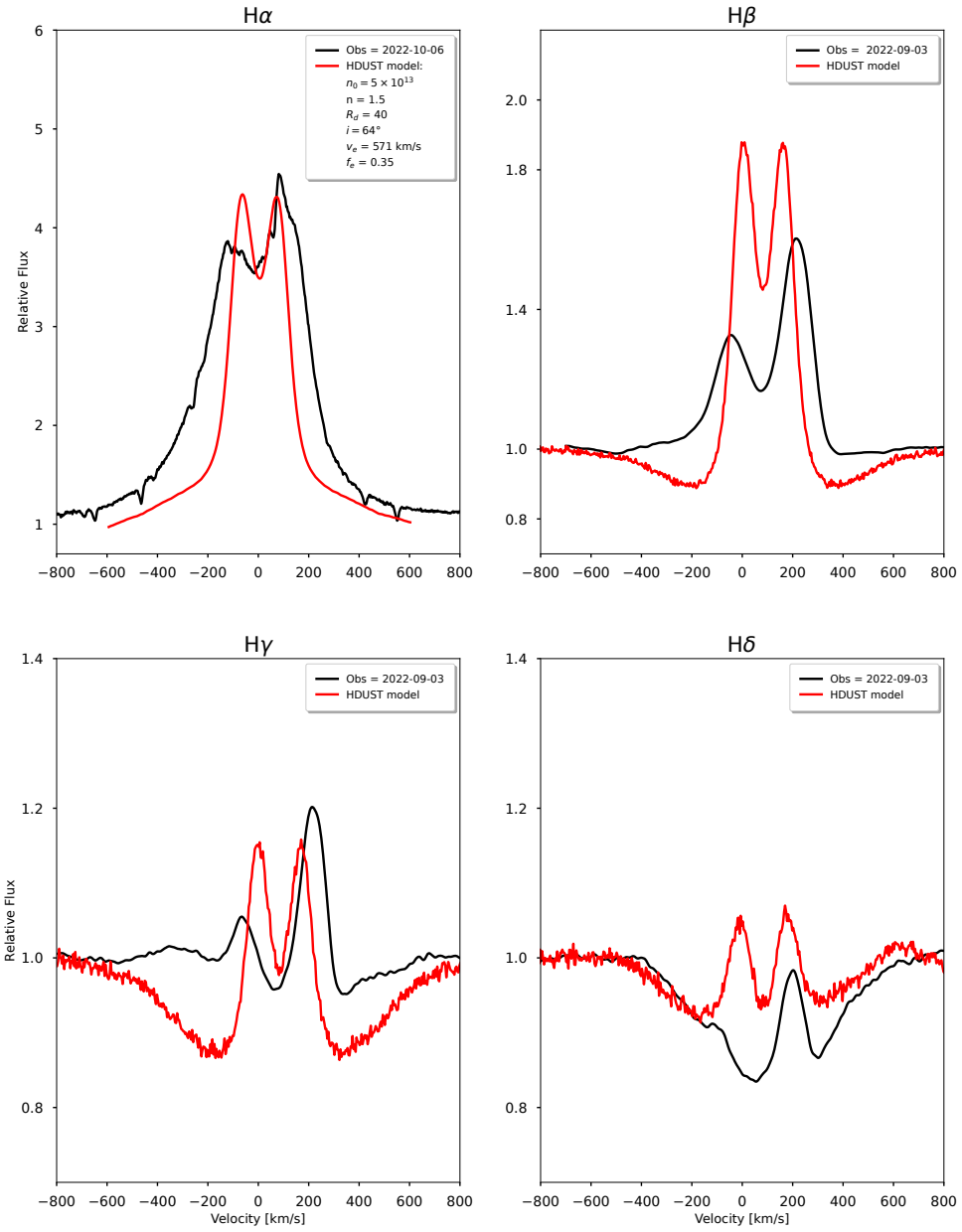

Figure 6.38: A comparison of the Oct 06, 2022, Hα observation in black with the best-fit model spectra of HDUST in red. A f_e 0.31 of the flux was convolved with v_e of 280 km/s to broaden the profile computed by HDUST. A Sep 03, 2022 comparison for Hβ, Hγ, and Hδ observations in solid black line and the HDUST model in red in the other panels. Note: The title of each figure indicate the corresponding Balmer lines, Hβ, Hγ, and Hδ have different y-axis limit.

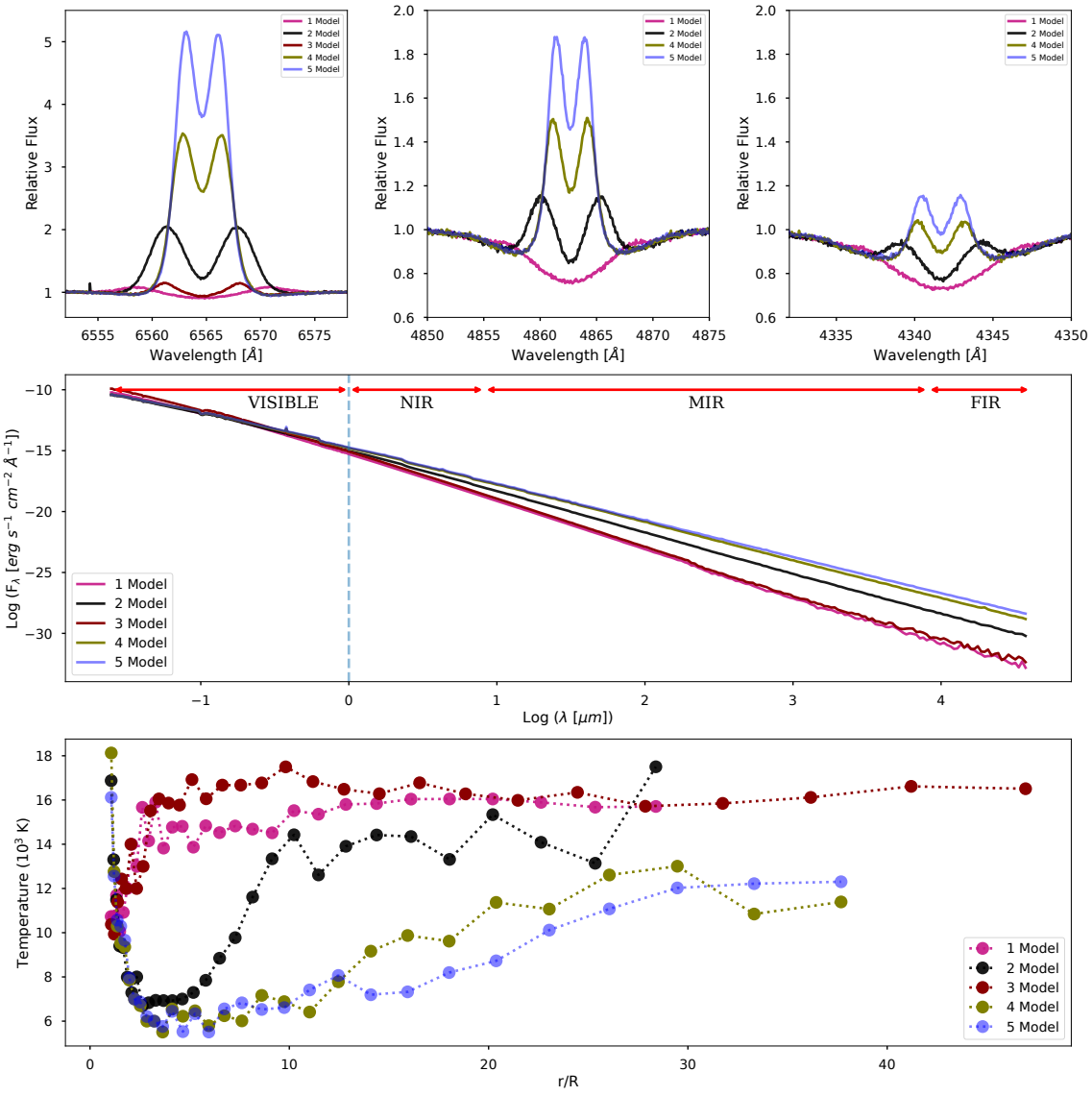

Figure 6.39: *Top Panels:* Evolution in time for the HDUST profiles for Hα (left), Hβ (center) and Hγ (rigth). *Center Panel:* The SED for the different profiles in logarithmic scale from the visible to the far-infrared (FIR). *Bottom Panel:* Disk temperature structure for the HDUST models. Note: The models are ordered by date. The 1 model indicates the first phase, and so on for the others.

CHAPTER 7

Discussion

This chapter presents the final discussion regarding the results obtained in this thesis. Sec. 7.1 examines how the variation of FeII, HeI, and other lines relates to the disk phases of the study of Hα. Sec. 7.2 follows the discussion of the evolutionary status and the stellar parameters of π Aquarii concerning the literature. Sec. 7.3 argues about the final parameters of the disk with the values found by other authors. Sec. 7.4 explains the new evidence of the binary status of π Aquarii.

7.1 Relation between Iron, Helium and other lines respect to the disk phases

Many Iron lines present emission since the third phase of Hα, for example, FeII 4232, 4584, 5018, 5169, 5198, 5235, 5276, 5316, and 5263. Several works in the literature are related to the study of Iron lines, e.g., Hanuschik (1987); Ballereau et al. (1995); Arias et al. (2006). The first work divides the line profile of FeII lines into two classes: Class 1 are double-peaked and symmetrical emission lines which describe the relationship between the width of the peaks concerning $v \sin i$; Class 2 line profiles exhibit single asymmetric sharp peaks in a complex, broad emission structure. The work concludes that the emitting region of FeII is inside Hα and Hβ formation region zone, close to the central star and that they are optically thin. It is possible to calculate the outer radius

emitting region for FeII lines using the Huang (1972) relation:

$$R_H = \left(\frac{2v \sin i}{DPS}\right)^2 R_\star, \tag{7.1}$$

where $v \sin i$ is the equatorial projected rotational velocity of the central star, $R_\star$ is the stellar radius and R_H Huang radius for the emission region. This relation was used to compute the Huang radius for the Balmer lines at 59579 MJD with $v \sin i$ = 282 km/s, taken from Table 6.2. This date was chosen because most of the lines present a double peak emission profile, therefore, a direct comparison can be made between them. We have for Hα: $R_H = 7.6R_\star$, Hβ: $R_H = 4.9R_\star$, Hγ: $R_H = 2.9R_\star$ and Hδ: $R_H = 2.5R_\star$. Looking at the FeII lines in Fig. 7.1, where the emitting regions are in a delimited area between the dashed lines, the only ones that are outside the emitting region of Hα and Hβ are FeII 5018 and 6249, with R_H, equals to 13.7 and 8.6 $R_\star$, respectively. All other Iron lines, including Helium and others (Si, O, etc.), are inside the emitting region of these two Balmer lines, being the closest to the central star, HeI 4388, with R_H = 0.55 $R_\star$.

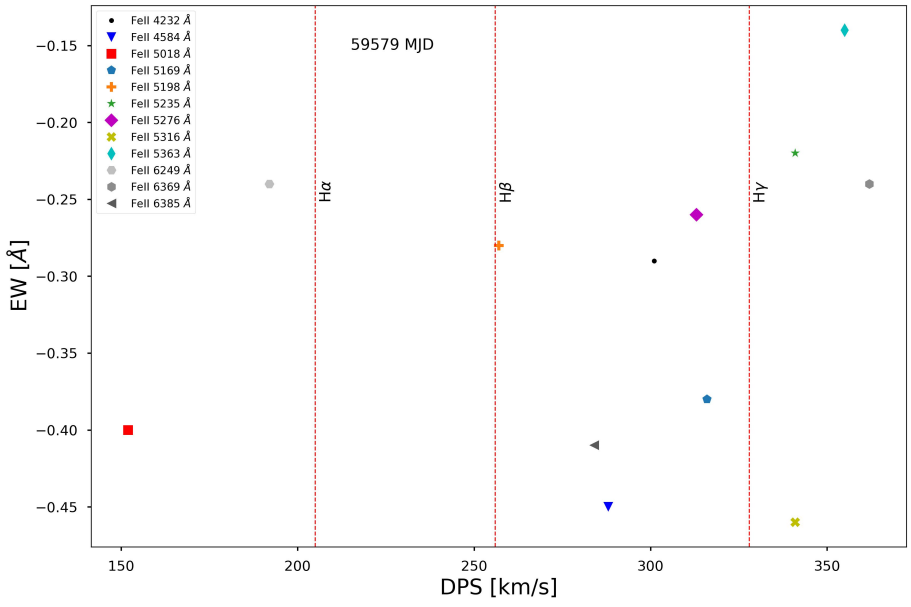

Figure 7.1: DPS of Iron lines compared to their EW for the 59579 MJD.

Ballereau et al. (1995) assert that Iron lines must be optically thick, which can change the location of the formation region where FeII lines are emitting. Arias et al.

(2006) studied the optical depth regime of FeII 5198, 5235, 5265, 5276, 5317, and 5365 lines and the degree of expansion of their formation region simultaneously, finding out that these lines are optically thick. They are formed in circumstellar regions close to the central star. This is also backed by the fact that the source function of FeII lines rapidly decreases with radii, preventing the formation in the outer part of the disk. They calculated the extent of emission region of FeII lines using the self-absorption-curve method (SAC)(Friedjung & Muratorio, 1987), which allows the opacity effect to be explicit on the emitted radiation intensity in contrast to Huang relations which is only for optically thin lines resulting in uncertainty in the outcome presented before.

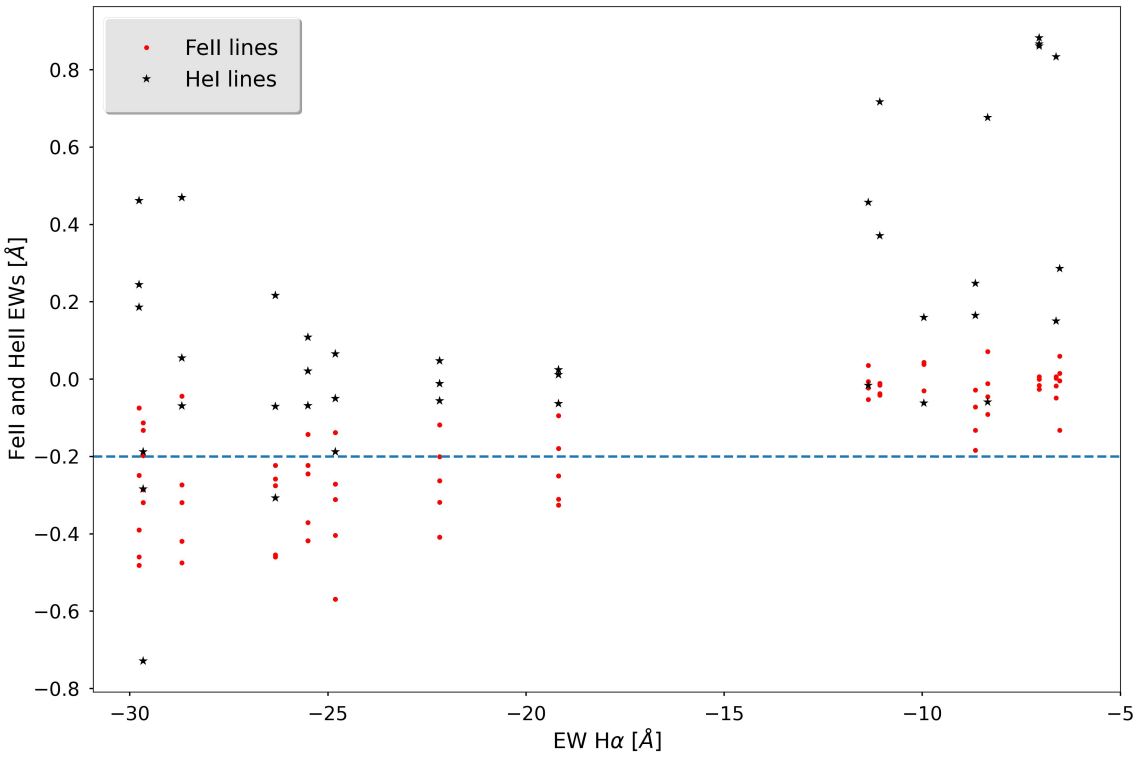

Figure 7.2: EW of Helium and Iron lines for all the dates compared to the EW of Hα for the same observation dates

After the third phase, it is observed that a notorious change in the emission of Hα constrains the emission in the Iron lines, as it can be observed in Fig. 7.2. In this period, the EW of Hα increases roughly from -10 to -20 Å. Most of the Iron lines present a double emission profile, meaning that the formation of these lines occurs in

the circumstellar envelope of the star and is sensible to a big mass-loss enhancement event in the disk, so an emission profile with great intensity from Hα over an EW of -20 Å can be a test-bed to measure the appearance of Iron lines in the spectra of Be stars. On the other side, Helium lines are unaffected compared to Iron lines, which may mean that these lines are not formed in the circumstellar disk, but rather close to the polar region of the central star, where the wind plays an important role. This is observed in the He 7065 Å line for the last observation date, where a kind of P-Cygni profile is seen.

7.2 Evolutionary status of π Aquarii

We study the evolutionary state of π Aquarii with the results obtained with the code `ZPEKTR`, using the evolutionary tracks from Georgy et al. (2013); Granada et al. (2013). Figure 7.3 shows the HR diagram for stars with $\omega = 0.95$, where the solid lines indicate the evolution tracks with the corresponding initial mass. This grid made by these authors has a range of masses between 0.75 to 15 $M_\odot$, separated in 270 evolutionary tracks, for rotating stars at Z = 0.014, 0.006, and 0.002. The interpolated models were obtained from `https://www.unige.ch/sciences/astro/evolution/fr/base-de-donnees/syclist//index/`. Zharikov et al. (2013) computed the mass using the stellar parameters; they calculated the M_V with system brightness V equals 4.85 mag, A_V=0.15 mag and HIPPARCOS distance of 340 pc, and using a $T_{eff} = 24000K$ with a bolometric correction BC of -2.36 mag, they finally obtained a luminosity equals to $\log L/L_\odot = 4.02$ that leads to an initial mass of 10.5 $M_\odot$. Using a shorter distance of 240 pc (van Leeuwen, 2007), the initial mass changes to 9.5 $M_\odot$ with the models from Ekström et al. (2012).

Our results correspond to the initial mass of 11.5 $M_\odot$ and its located inside the main sequence (hereafter MS), approximately half of the MS band. The dynamical mass found by Bjorkman et al. (2002) is 12.5-17 $M_\odot$ computed in a disk-less phase with a range of i of 65-85 °. Our stellar parameters were computed in 2013, where the EW of Hα dropped to a minimum, with a range of i between 25-45 °. With these new models, the initial mass of Zharikov et al. (2013) would change from 10 to 11 $M_\odot$.

Several authors have calculated $\log g$ and $v \sin i$ of π Aquarii. Chauville et al. (2001) studying the HeI 4471 line determined T_{eff} and log g of 116 Be stars. For π

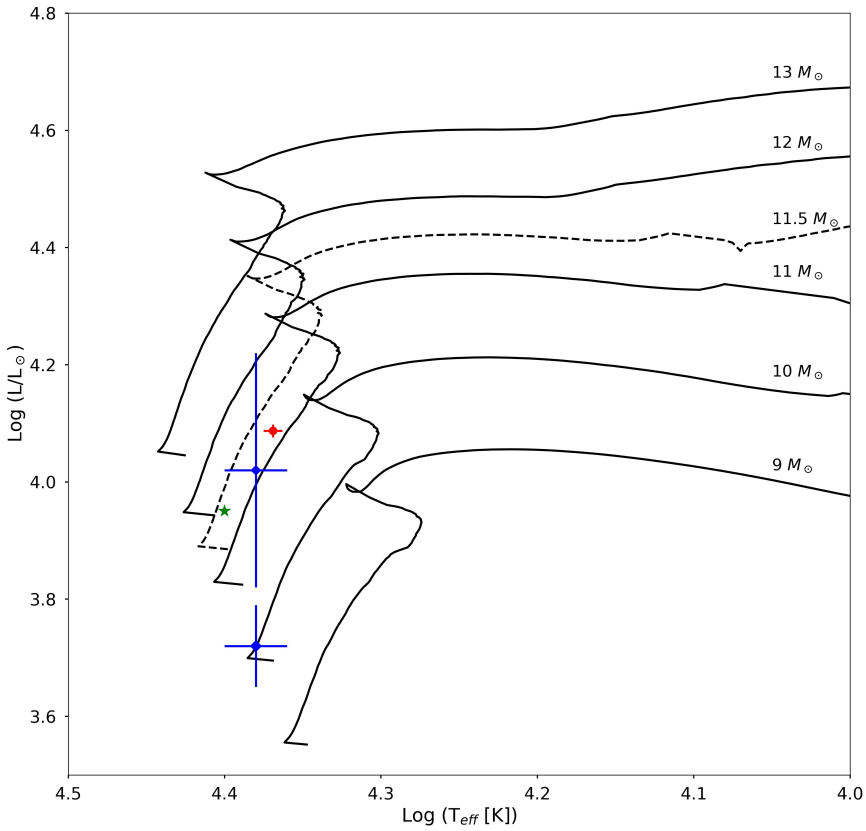

Figure 7.3: HR diagram for π Aquarii. The solid lines indicate the evolutionary tracks of stars with rotation from Georgy et al. (2013); Granada et al. (2013). The dashed line represents an initial mass of 11.5 $M_\odot$. The filled red circle shows the result of this thesis. The filled blue diamonds show the luminosity and temperature calculated from Zharikov et al. (2013), and the star symbol (in green) is from Hohle et al. (2010).

Aquarii they found T_{eff} = 26668 K and $\log g$ =3.95. Frémat et al. (2005), utilizing a code that considers the fast rotation of stars as rigid rotators and gravity darkening, found for T_{eff} and $\log g$: 26061 $\pm$ 736 K and 3.92 $\pm$ 0.09, respectively. Arcos et al. (2018) used photometry data fitted with Kurucz (Kurucz, 1979) and TLUSTY (Hubeny & Lanz, 1995b) stellar atmosphere models, together with spectroscopy data to find the parameters of a Be star sample. For our star the results are: T_{eff} =24500 $\pm$ 245, $\log g$ = 3.4 $\pm$ 0.03 and $v \sin i$ =215 $\pm$ 4. Ahmed & Sigut (2017) using photospheric nitrogen

abundances, computed T_{eff} = 26061.0 K and $\log g$ = 3.7. We note that different authors' temperatures are similar, but the effective gravities in all works are always lower than 4.

Rivinius et al. (2013) summarized the key properties of the rotation of Be stars, deriving an average value of $\bar{W} = 0.8$, based on spectroscopic (Frémat et al., 2005) and interferometric (Meilland et al., 2012) analyses. They note that this value doesn't depend on the temperature or the effective gravity; more relevant, the lowest W value for a B star to become a Be star is approximately 0.7. The W calculated in our work agrees with these values. Looking at other works, Zorec et al. (2016) computed the true velocities of 233 Be stars, fixed by the effects of gravitational darkening, binarity, and macroturbulence, finding that the mode of γ is equal to 0.65. The value of γ of π Aquarii in Table 6.2 falls within this range and is greater than the mode. If it is compared with the work of Cochetti et al. (2019), where they derived the mean values of $\gamma = 0.75$ and $\omega = 0.9$ of 18 Be stars, using interferometric observations, it is found that the values computed by `ZPEKTR` of π Aquarii of $\gamma = 0.79$ and $\omega = 0.93$ are in agreement with the previously mentioned values.

7.3 Parameters of the disk of π Aquarii

The second part consisted of modeling representative disk phases chosen through the changes observed in Hα. Five dates were considered as disk phases. We found the disk parameters by using `HDUST`. Other works that have monitored long-term spectroscopy are Suffak et al. (2020); Ghoreyshi et al. (2021); Marr et al. (2021, 2022) .

Up to the third phase, the `HDUST` best-fit models reproduce well the observations of Hα, with ρ_0 varying between 5×10^{-13} and 5×10^{-11} [gcm^{-3}]. The disk truncation radius R_d is 30 $R_\star$, which is below the value found by Zharikov et al. (2013) of 65 $R_\star$ estimated assuming Keplerian motion of a particle in a circular orbit at the outer part of the disk, in a period between 2004-2013. They do not specify to what year exactly represents this value. As explained in Sec. 5.2.2, changes in the truncation disk radius barely affect the final flux of the model in `HDUST`. This is observed in Fig. 5.7, where the solid blue line represents a model with 50 $R_\star$. The increment in the emission is almost despicable compared to the solid gray line with an R_d of 30 $R_\star$; therefore, there may be an underestimation of the radius. Also, the χ^2 obtained for models with different radii do not vary significantly. Maybe, it is necessary to consider a lower

truncation disk to analyze up to what radius there is a contribution of Hα in this code.

From the fourth phase, it isn't easy to make a statement regarding the parameters of the disk due to the high value of the χ^2 test and the fact that the wings of the observations are not reproduced with HDUST . However, ρ_0 and n values obtained are expected values since as the disk is growing, the base density needs to be higher as the mass-loss enhancement from the central star provides more mass to the envelope, and with a lower value n the curve at which it decays the base density it is slow, which coincides with a growing disk .

The inclination range found by Bjorkman et al. (2002) is 50-75° in the quasi-normal phase between 1996-2001, which agrees with the value found in this work of 64° for the first phase. Silaj et al. (2010) modeled the Hα double-peaked emission using a non-LTE radiative transfer code with solar-type chemical composition named BEDISK (Sigut & Jones, 2007) for the date Dic 19, 2007. They used a B0-type model for the central star with $\rho_0 = 10^{-11}[gcm^{-3}]$ and $n = 3.5$ observed an i equals to 45°. Arcos et al. (2017) derived the disk parameters for three different epochs. For Nov 14, 2012, and Oct 24, 2015: $\rho_0 = 1 \times 10^{-11}[gcm^{-3}$, $n = 2.5$ and i=60°, for July 24, 2013, $\rho_0 = 7.5 \times 10^{-12}[gcm^{-3}$, $n = 2.5$ and i=60°, all the model have $R_d = 12.5\ R_\star$. Vieira et al. (2017) using the SED obtained $\log \rho_0 = -12.1$ and $n = 3.5$. Finally, Cochetti et al. (2019), using two interferometric measurements from October 28 to 31, 2014, found an inclination of 34° among other geometrical and kinematical parameters for the circumstellar envelope.

Compared with this work, there is a discrepancy with the model of Silaj et al. (2010) (hereafter BEDISK model). Fig. 7.4 shows the closet observation of Hα in our sample on Oct 6, 2007, which is two months before the observation of the BEDISK model with a lower intensity of around 0.1. The parameters for the disk are extremely opposed between both models. In our model of HDUST with $\chi^2 = 1.05$, ρ_0 is equal to $5 \times 10^{-13}[gcm^{-3}]$, which is the half of the BEDISK model, n is 1.8, also almost half compared to n equals to 3.5, and the inclination is 56° which falls in the range of possible inclinations for the system. The main difference that can be noted between both codes to give these contrasting results is that the radiative transfer problem is not treated in the same way. The composition, while HDUST only uses hydrogen, BEDISK uses solar composition for the level population. Hence, the lack of electrons

from metals in the gas disk alters the cooling processes, overestimating the disk flux.

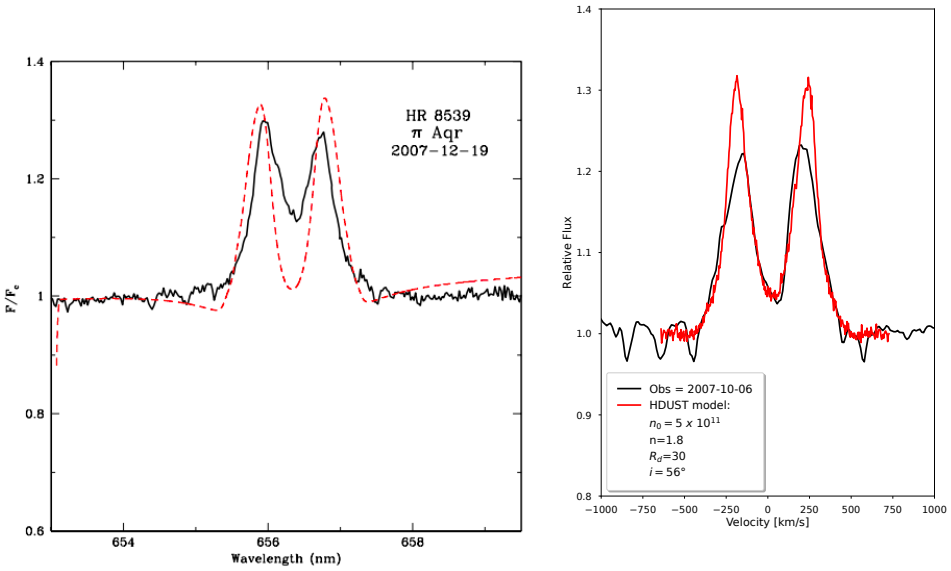

Figure 7.4: Comparison between Silaj et al. (2010) for the date Dic 19, 2007 (left), and our work for the date Oct 6, 2007 (right).

Moving to the parameters obtained by Arcos et al. (2017), where they use an updated version of the `BEDISK` code, named `BEDISK & BERAY` Sigut (2011). The three observations are the same occupied in this work, selected from the BeSOS sample. For the first date, our best model with $\chi^2 = 9.01$ have the same base density, n equals 2, and $i = 63°$. For the observation of 2013, our best model with a $\chi^2 = 3.67$ has a similar base density of $7 \times 10^{-12}[gcm^{-3}$, the same n and i equals 56°. Finally, for the last observation of 2015, our best model with a $\chi^2 = 25.6$ have a $\rho_0 = 3 \times 10^{-11}[gcm^{-3}]$, n=2, i=63° and $R_d = 40R_\star$, the first two models have $R_d = 30R_\star$. Comparing both works, the inclinations angles are very similar. The base density for the first two observations are in agreement, but for the last, our result is three times larger with a lower n value of 2.

Finally, we can compare the inclination angle of 34° with the interferometric work of Cochetti et al. (2019), which is a more accurate measurement of the geometric shape of the system. Our result for i is equal to 43°.

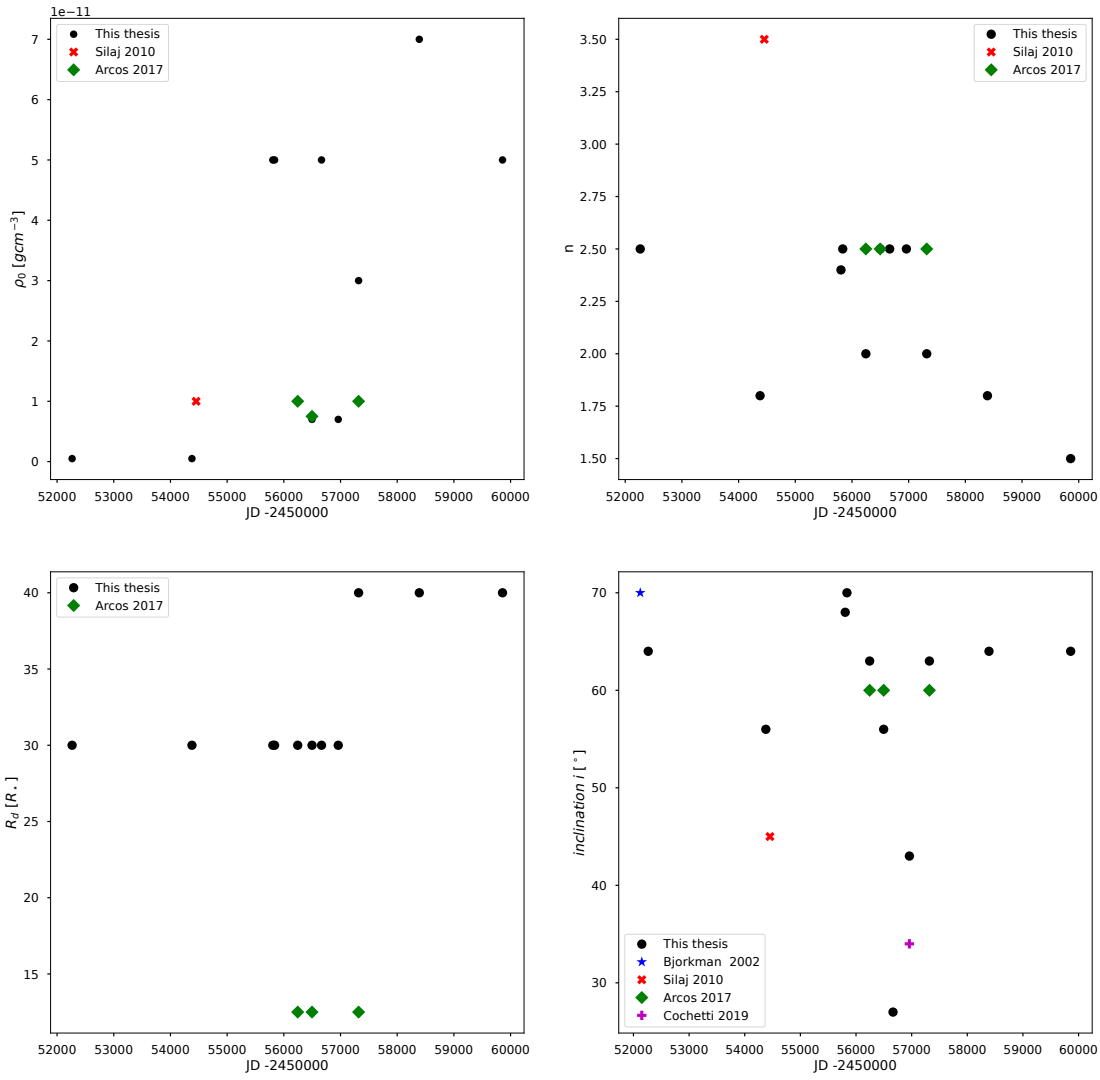

Figure 7.5: Final results for ρ_0, n, R_d, and i with our results (filled black circle) and other authors shown in the legend.

Regarding Hβ, Hγ, and Hδ (only for the last phase), the HDUST models computed for these lines with the parameters fitted for Hα demonstrate that is not achievable

fit simultaneously all four lines with a single power law for the radial component as is shown in the four profile lines in Fig. 6.38. This is also observed in the work of Klement et al. (2015), where it is explained that steeper falloff (higher n) is needed in the inner parts of the disk where Hβ, Hγ, and near-IR continuum are originated. In the emitting region of Hα, a shallower density profile is needed to increase the size of the optically thick emitting area to enhance the line EW. This observation further supports that a uniform power law across the entire disk does not adequately describe the density profile.

7.4 New evidences of binarity

Hα has been changing dramatically from a Shell-type profile to a clear double-peaked emission profile. Around 2018, the shape changed, with a higher intensity in the 229 emission, forming a single emission line, and sometimes a third-like peak appears in the 230 emission, which can be attributed to the binary companion. Table 7.1 describes the behavior of the profile of Hα over time for the five phases of the disk. One possible explanation for this behavior is that the extent of the disk is very close to the companion at a distance of 0.96 AU (Bjorkman et al., 2002). Therefore, it is affected by its emission or can be truncated. This last could be confirmed/discarded through radio wavelength observations of the SED as proposed by Klement et al. (2019).

From the last two phases, for the higher resolution profiles of Hα, it can be noted a third weak peak in the center of the line, which is not appreciated in the previous phases . As not all the profiles have the same resolution, is not possible to observe this peak in the lower ones and therefore we can derive a period. Figure 7.6 collect 4-period orbital cycles. Each color represents a cyclic where each profile is separated by approximately 81 days (more or less). In the upper two profiles of 2019, a variation in this peak to the right can signify a half period of the binary passing.

Date	i[°]	Description of Hα
2001-12-22	56	Shell-type profile with clear DPS, the maximum intensity reaches 1.07 and the minimum 0.88.
2011-09-02	68	Double-peaked emission profile with symmetric V/R, the maximum intensity is around 2.
2014-01-08	27	Similar to phase 1, Shell-type profile with asymmetric DPS, being the red peak greater, maximum intensity at 1.15 and minimum at 0.92.
2018-09-29	64	Sharp emission profile with no clear DPS, a third peak manifest in the center of the line, V/R $>$ 1, maximum intensity around 3.3.
2022-10-06	64	Similar to the previous phase, sharp emission profile, a small emission occurs in the center of the line, sharp read peak V/R $<$ 1, the location of the violet peak is not very clear.

Table 7.1: Relation between the inclination of the phases and the shape of the Hα emission line.

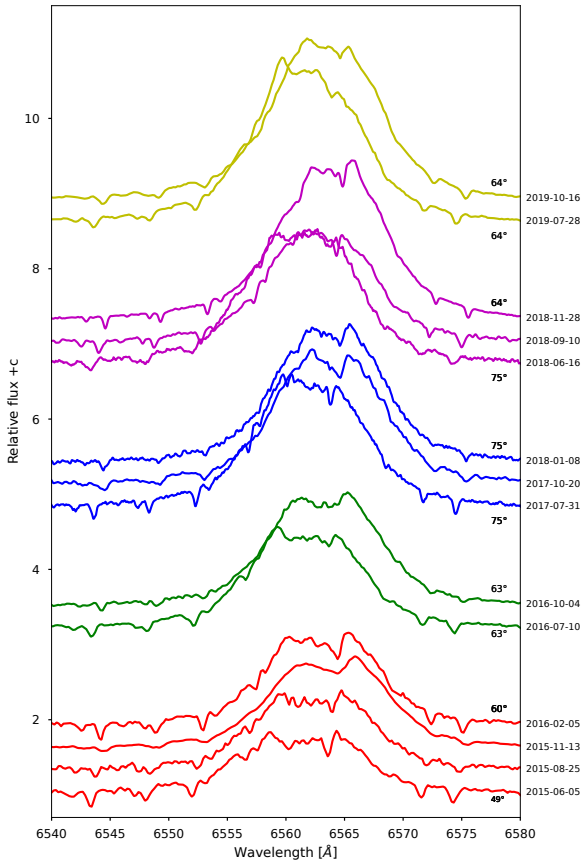

Figure 7.6: Different orbital cycles of π Aquarii from the third phase of Hα. Each color represents where it was possible to have at least two observations separated for approximately 81 days. In the first and final observation is the inclination computed with `HDUST`.

CHAPTER 8

Conclusion

π Aquarii is a rapid rotator Be star in a binary system that has been studied over a long time, since the 30s, due to its great variability. This thesis aims to reveal new information about this star, characterizing its behavior with new observations from star catalogs such as BeSOS and BeSS, and analyze how the changes in the central star are related to the circumstellar envelope. It also studied the phases of activity of the disk with the variation of Hα over the years, modeling the parameters of the disk using a VDD model, which is a successful model in agreement with observations of Be stars. This model tells us that the density distribution falls off as a power law radially (r) and a Gaussian distribution in hydrostatic equilibrium axisymmetric respect to the disk's mid-plane in the vertical direction. This distribution is used as input in the `HDUST` 3D NLTE Montecarlo radiative transfer code that computes the theoretical line profiles, the spectral energy distribution, and the disk temperature distribution, given first the stellar and disk parameters and the rotation rate W.

We modeled the observed Hα line profiles divided into five specific dates over 21 years, chosen by a notable change in their EW. Computing a small grid with `HDUST`, we found the disk parameters for the first three phases with low uncertainty. For the first, second, four, and fifth phases, the range of inclination is between 50-70 °. Still, for the third phase, the inclination is lower, around 25-45° which can be the reason for the sudden apparition of FeII emission lines. Some Helium and Other lines are also in

emission in different epochs of the star.

The range of ρ_0 is in the range of 5×10^{-13} and 5×10^{-11} [gcm^{-3}], n varies between 1.8 and 2.5, and the R_d is 30 $R_\star$ for the first three phases and the last two, 40 $R_\star$. We note that the HDUST models are not sensitive to the truncation disk; therefore, a higher value can also be possible.

New observations of Hα confirm the phase-locked V/R variation of 81.14 days, which is the period of the binary star found by Bjorkman et al. (2002). For the RV after two harmonic frequencies, it was found a frequency of 81.14 days, which is similar to the period of V/R.

8.1 Future Work

- This work only used visible range spectroscopy data. Hence, it is useful to use other ranges of wavelength, for example, the IR and the radio part of the spectrum, where other series of hydrogen can be studied and compute the parameters of the disk. It is also possible to calculate the excess in the SED of the star to compare it with the HDUST models.

- It is essential to find a better or more efficient way to compute the errors of each measurement from different instruments. For example, in the work of Vollmann & Eversberg (2006), they show a way to compute the error of the EW concerning pure photon noise statistic, but the signal is needed to noise for the profile. Therefore, this mechanism can be tested to consider the errors better. For the other measurements, it is possible to test other methods that are less sensitive to the resolution of the line profile.

- We need to obtain the light curve from photometric data to study the relationship between the star's photosphere, where Non-Radial Pulsation can be revealed, and the formation of the disk; this can be complemented with the spectroscopic data.

- Use the SAC method utilized in Arias et al. (2006) to compute the emitting region of the emission lines and compare them with Huang's relation.

- Use another code to reproduce the last two phases of the Hα, where the maximum extent of the HDUST models is approximately 200 km/s, and the wings of the observations cannot be fitted with this code.

Appendix A

Sample from BeSS

Table A.1: Instruments from BeSS for optical range

Spectrograph	Date	Resolution	Range [$\AA$]	Orders
ELODIE	2001-12-22	45000	3900 - 6810	67
eShel	2008-07-21	10000	4380 - 7000	19
eshel101	2009-08-19	10000	4360-6700	18
eShel	2010-10-26	10000	4300-7100	21
eShel_T_Garrel	2011-10-03	11000	4300-7300	22
eShel_T_Garrel	2012-09-22	11000	4140-8100	27
Eshel	2013-09-20	11000	4200-7300	23
eshel-5	2014-10-29	11000	4280-7100	21
Eshel	2015-10-31	11000	4200-7200	23
Eshel	2016-10-31	11000	4200-7200	23
Eshel	2017-10-31	11000	4200-7200	23
eShel101	2018-10-09	11000	4200-7200	23
eShel101	2019-10-16	11000	4200-7200	23
Eshel + ESP	2020-10-30	30000	3750-7550	31
NOU_T	2021-12-31	8500	3700-8100	33
NOU_T2	2022-09-03	8500	3700-8800	35

Table A.2: Instruments from BeSS and spectra of Hα

Spectrograph	Numbers of spectra	Resolution
Bardin	1	8000
LHIRES1	4	6000
Lhires3-76	5	17000
Slitless-Grating	5	14000
eShel	25	10000
Slit-Grating	6	16000
LHIRES-A12t	3	6000
LHIRES3	71	6000
LHIRES-B	99	7000
LIHRES III -1800	19	11000
LIHRES III	97	20000
Classical 23um slit 1800lpm grating	9	8000
Lhires 3	23	17000
Lhires3-2400-76	5	15000
L200_1800	12	7819
eshel-5	1	11000
Lhires III 2400 t/mm	5	17000
L-200	7	5800
eShel101	58	11000
LINX	33	9000
MUSSOL	8	9000
LHIRES C11	7	14000
NOU_T	10	9000

Appendix B

Evolution of Hα in the time

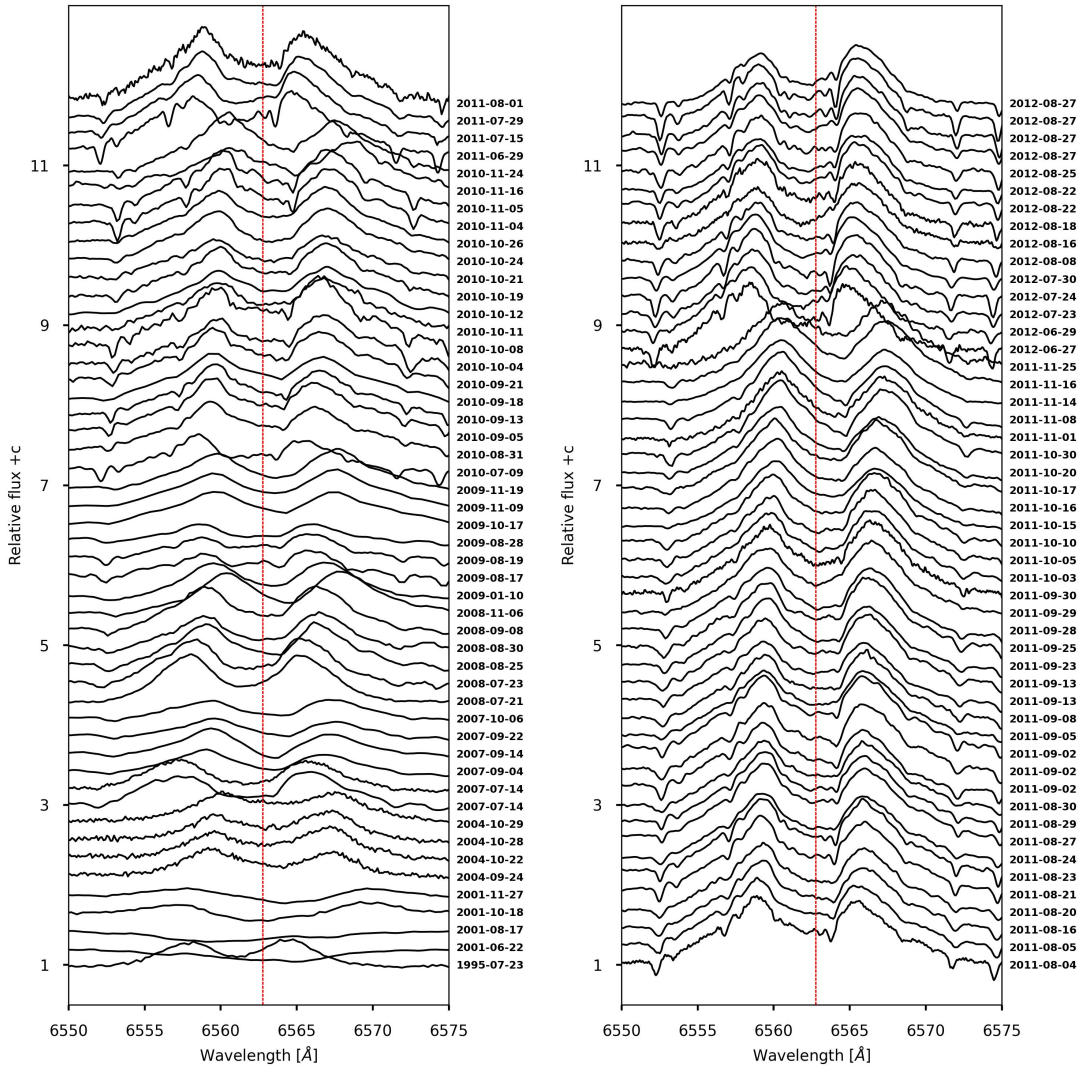

Figure B.1: *Left panel:* Evolution of Hα in time, from the Initial value up to 2011, is plotted. *Right panel:* Continuation from 2011 to 2012. Note: A constant c is added to each data to observe more clearly the evolution of Hα, and the vertical black line corresponds to the theoretical value of Hα.

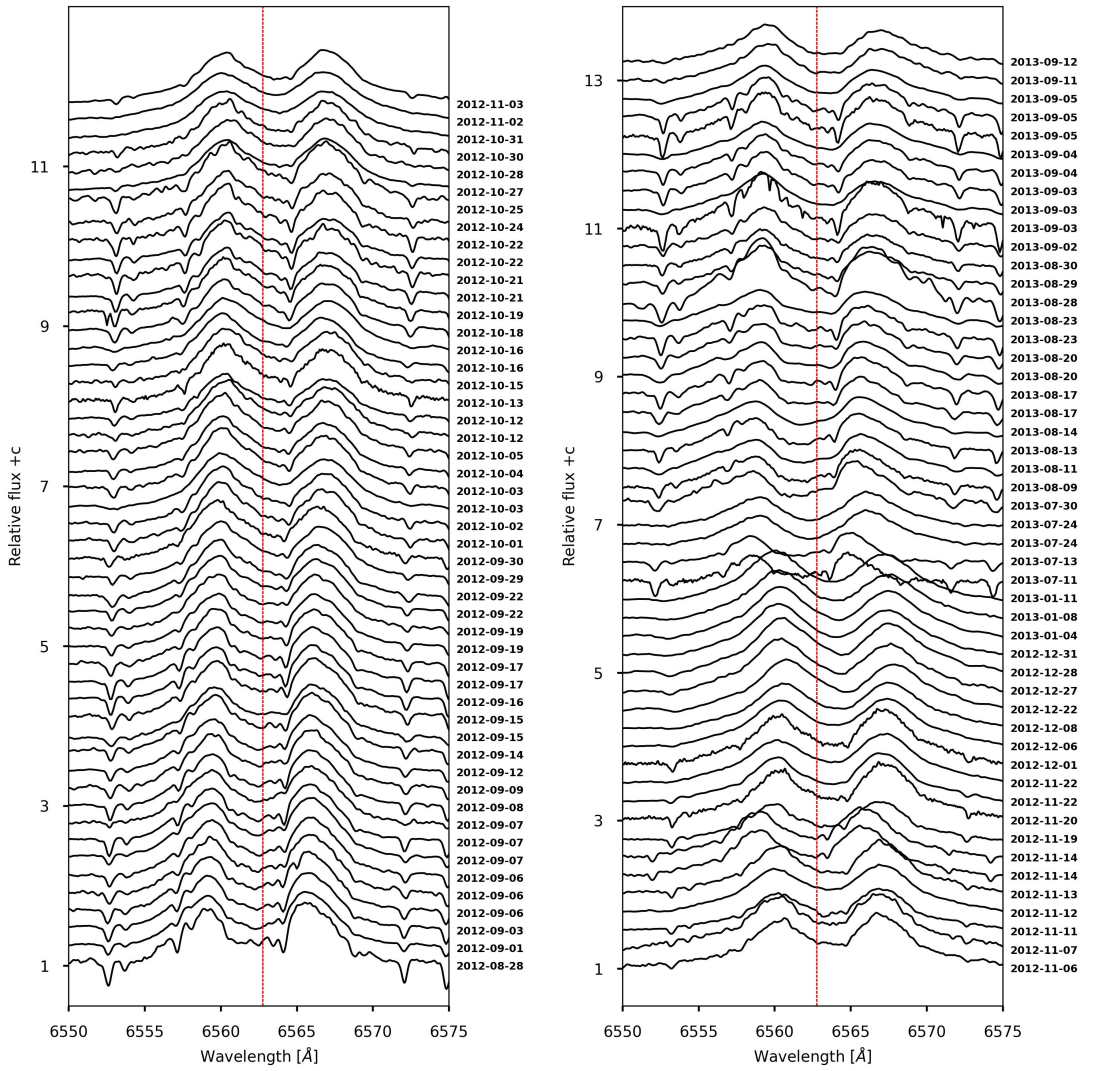

Figure B.2: *Left panel:* Same as Fig. B.1, the evolution of the Hα is from 2012-09 up to 2012-11. *Right panel:* Evolution in time ranging from 2012-11 to 2013-09

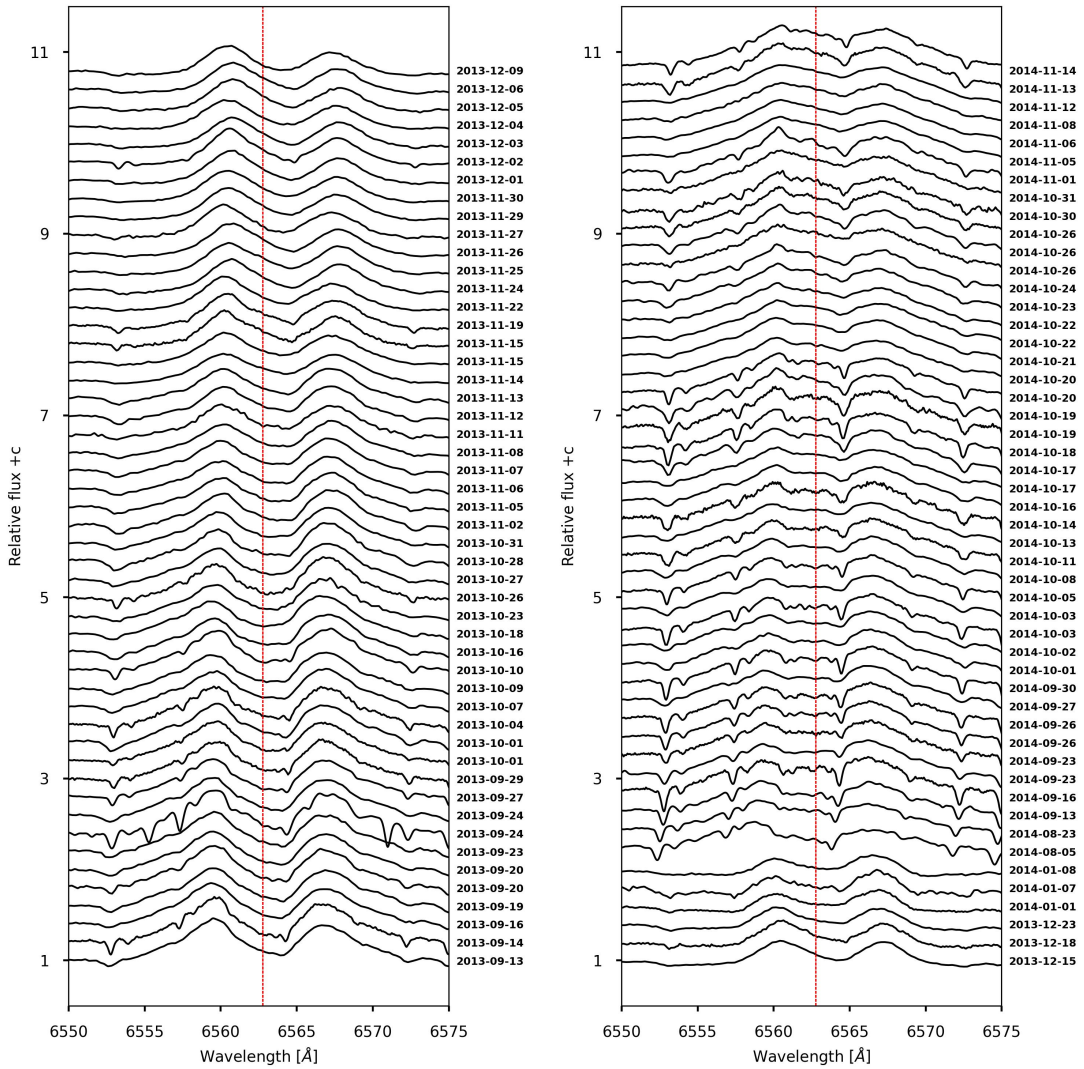

Figure B.3: *Left panel:* Same as Fig. B.1, the period of evolution: 2013-09, 2014-01. *Right panel:* Evolution from 2014-01 to 2014-11.

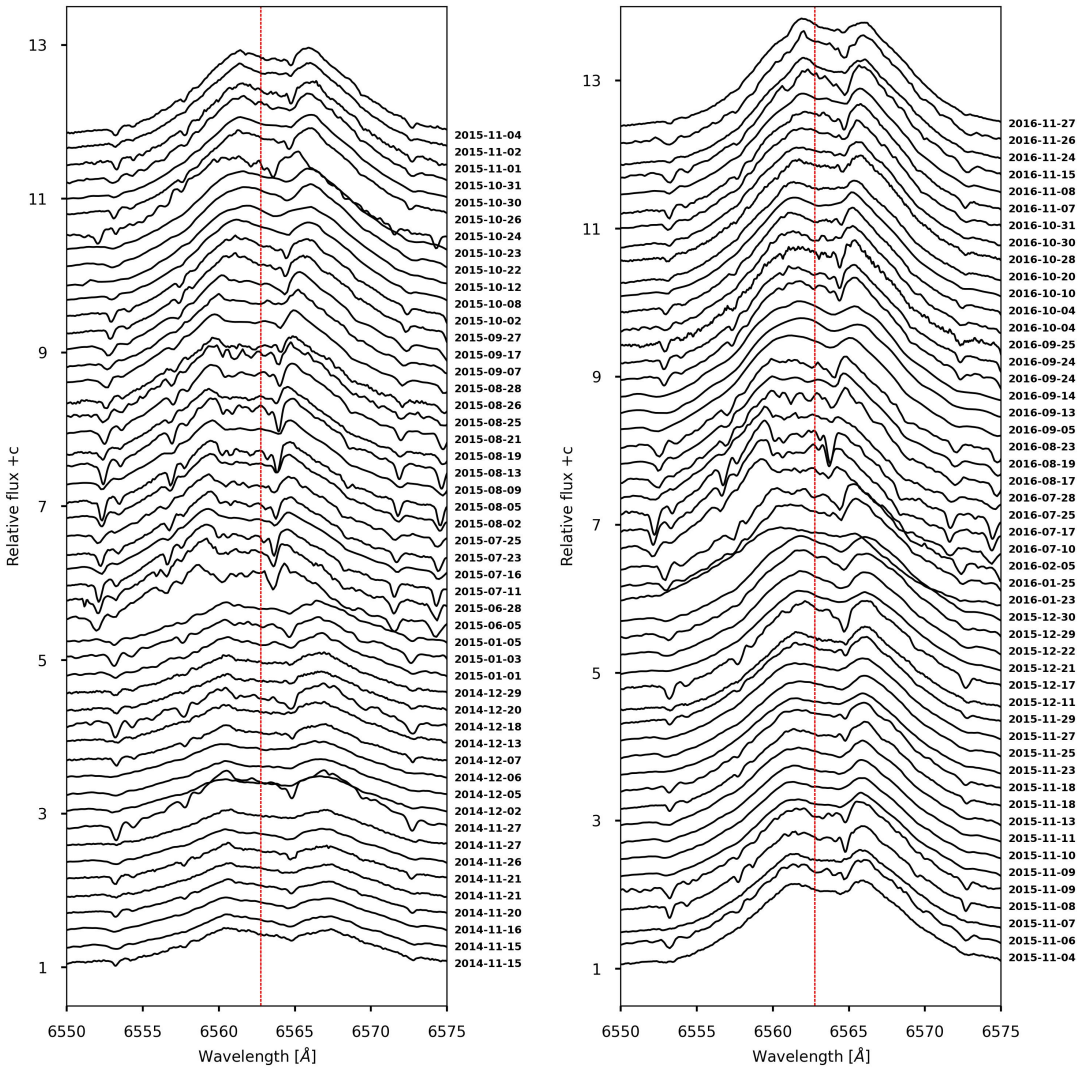

Figure B.4: *Left panel:* Same as Fig. B.1, time evolution of Hα from 2014-11 to 2015-11. *Rigth panel:* 2015-11 to 2017-09.

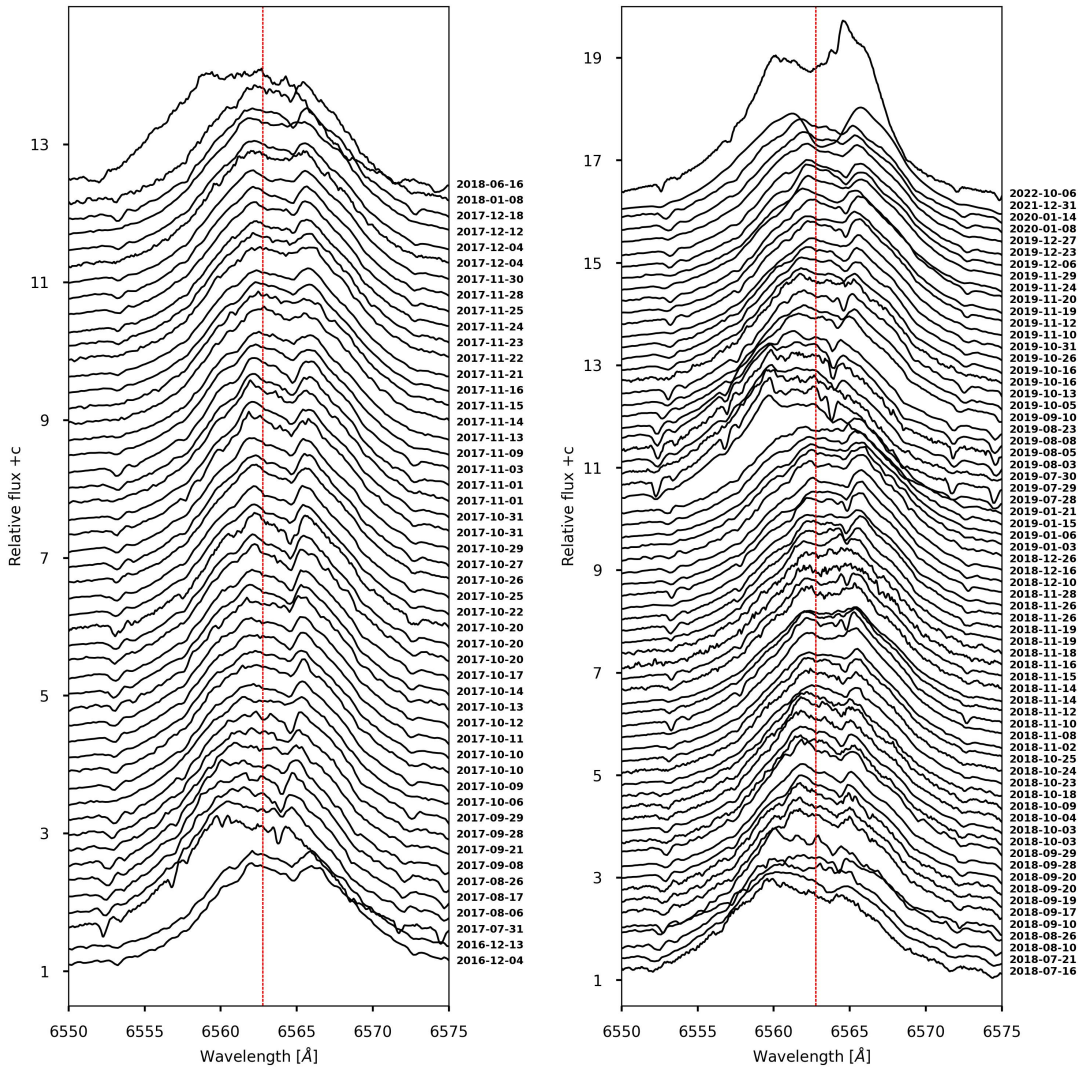

Figure B.5: *Left panel:* Same as Fig. B.1, 2017-09-2018-09. *Right panel:* 2018-09-2021-12

Appendix C

Theoretical lines to calculate radial velocity

Table C.1: Observed spectral lines and their variation in π Aquarii

HeI		FeII		Balmer Lines		Other lines	
Line	Theoretical value	Line	Theoretical value	Line	Theoretical value	Line	Theoretical value
4388	4 387.92	4233	4 233.16	Hδ	4 101.73	O II	4 253.89
4471	4 471.48	4549	4 549.47	Hγ	4 340.47	O II	4 416.97
4713	4 713.15	4584	4 583.83	Hβ	4 861.35	Mg II	4 481.13
4922	4 921.93	4629	4 629.33	Hα	6562.78	Si III	4 552.62
5015	5 015.68	4667	4 666.75			Si III	4 567.82
5047	5 047.74	5018	5 018.44			C III/ O II	4650.12
5875	5 875.62	5169	5 169.03			Ti I/O II	4675.12
6678	6 678.15	5198	5 197.57			Si II	6 347.10
7065	7 065.19	5235	5 23462			Si II	6 371.36
		5276	5 275.99				
		5316	5 316.21				
		5363	5 362.97				
		6249	6 248.91				
		6369	6 369.02				
		6385	6 385.46				

Theoretical rest wavelength for each line presented in π Aquarii taken from the NIST database

Appendix D

Evolution of all lines in time

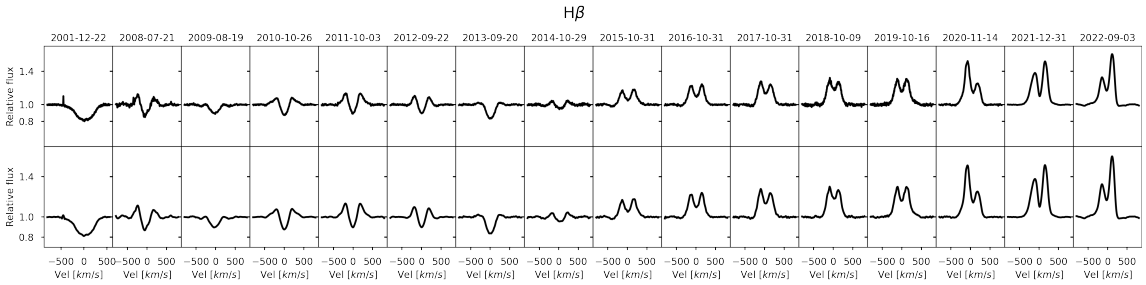

Figure D.1: Evolution of the Hβ line over the years, Top panel the spectrum without filtering.

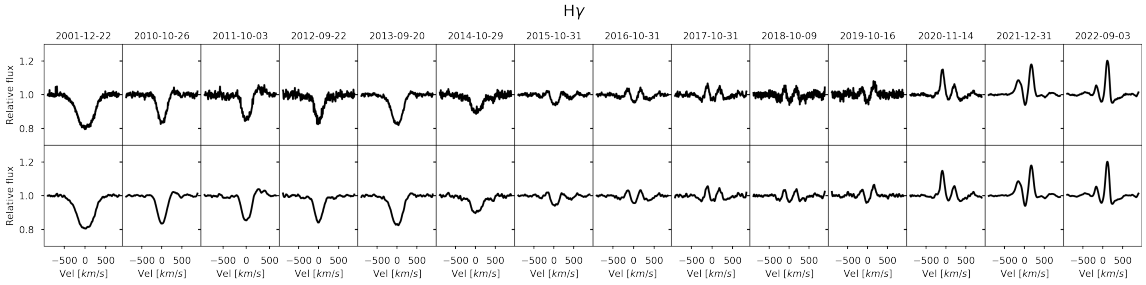

Figure D.2: Evolution of the Hγ line over the years, Top panel the spectrum without filtering.

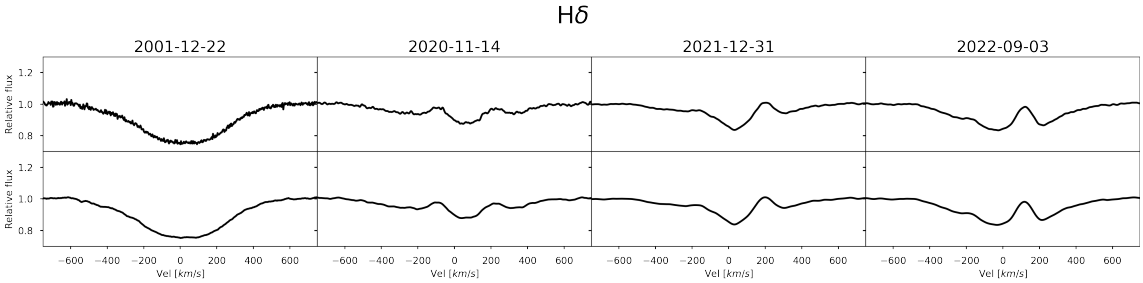

Figure D.3: Evolution of the Hδ line over the years, Top panel the spectrum without filtering.

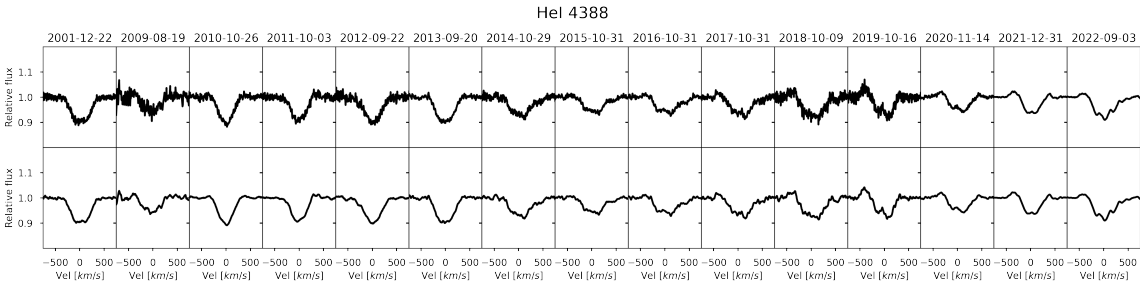

Figure D.4: Evolution of HeII 4388 over the years, Top panel the spectrum without filtering.

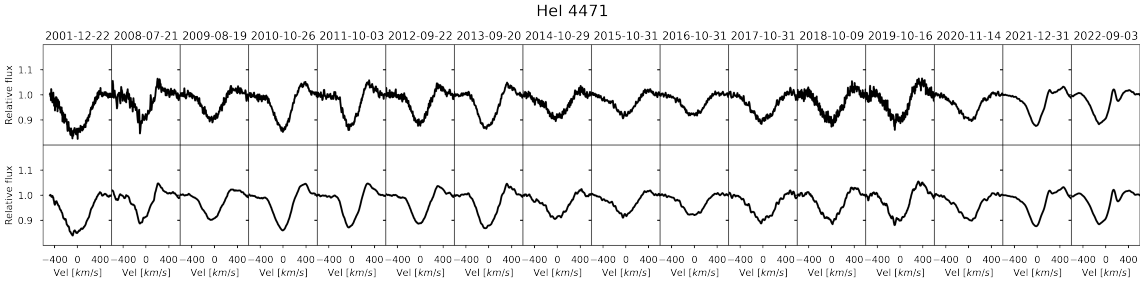

Figure D.5: Evolution of HeII 4471 over the years, Top panel the spectrum without filtering.

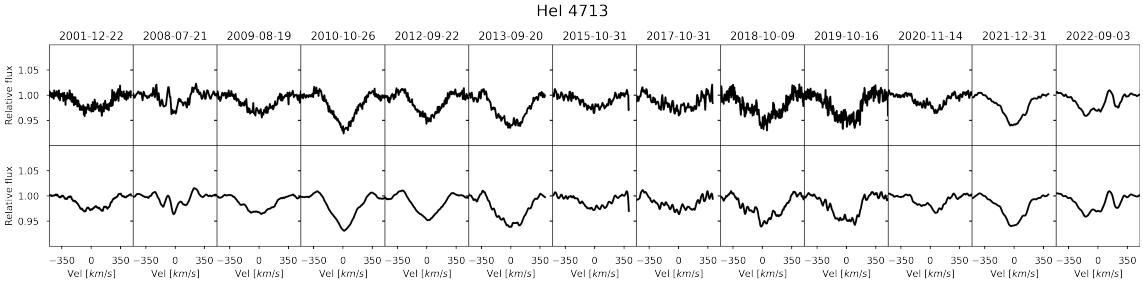

Figure D.6: Evolution of HeII 4713 over the years, Top panel the spectrum without filtering.

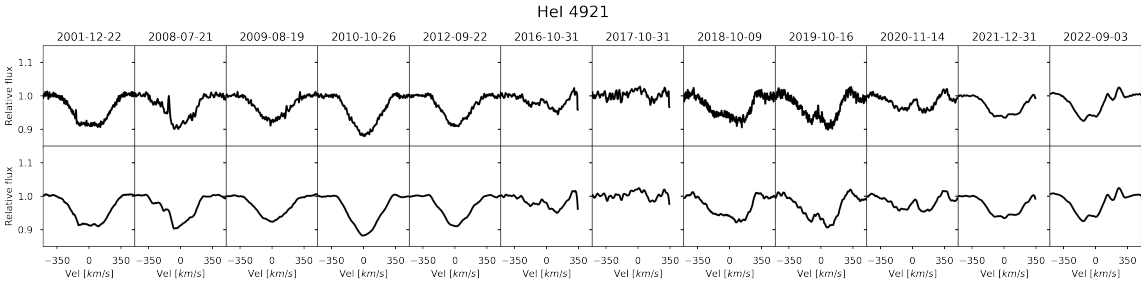

Figure D.7: Evolution of HeII 4921 over the years, Top panel the spectrum without filtering.

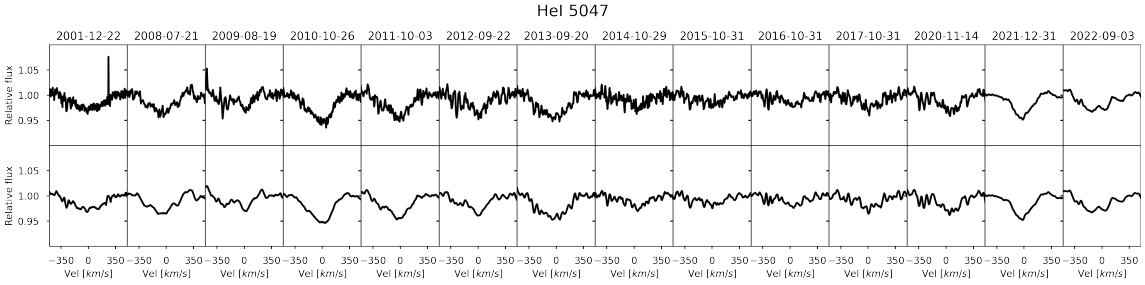

Figure D.8: Evolution of HeII 5047 over the years, Top panel the spectrum without filtering.

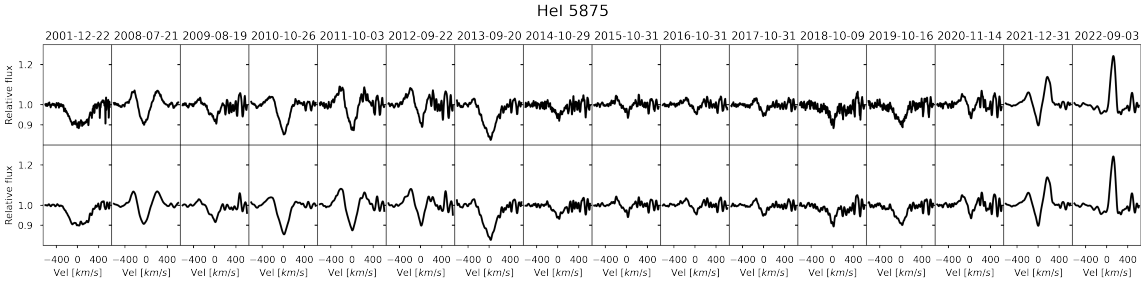

Figure D.9: Evolution of HeII 5875 over the years, Top panel the spectrum without filtering.

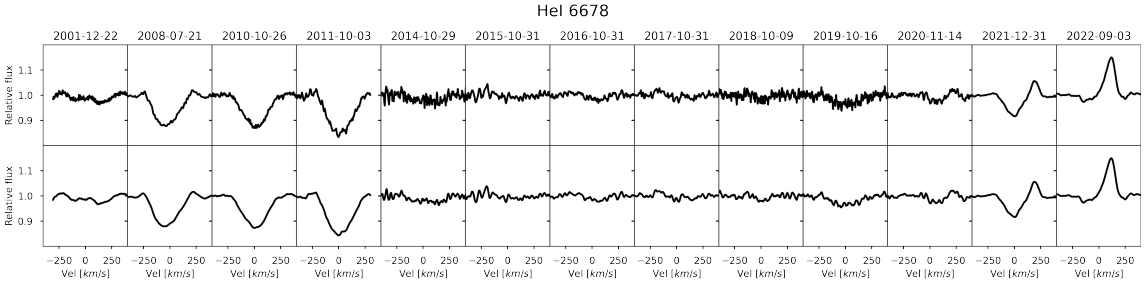

Figure D.10: Evolution of HeII 6678 over the years, Top panel the spectrum without filtering.

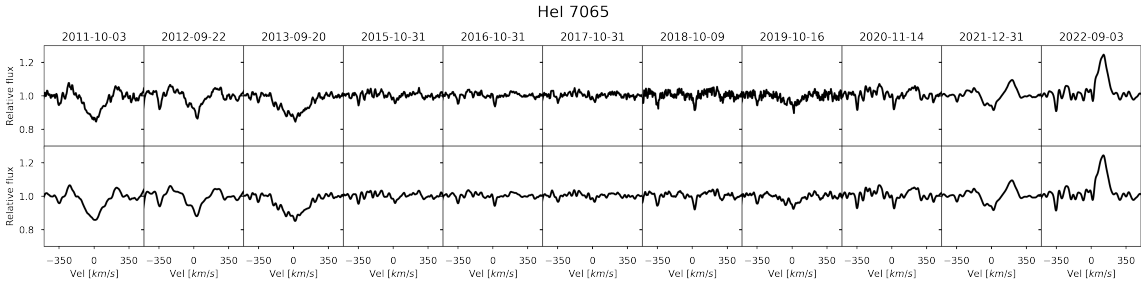

Figure D.11: Evolution of HeII 7065 over the years, Top panel the spectrum without filtering.

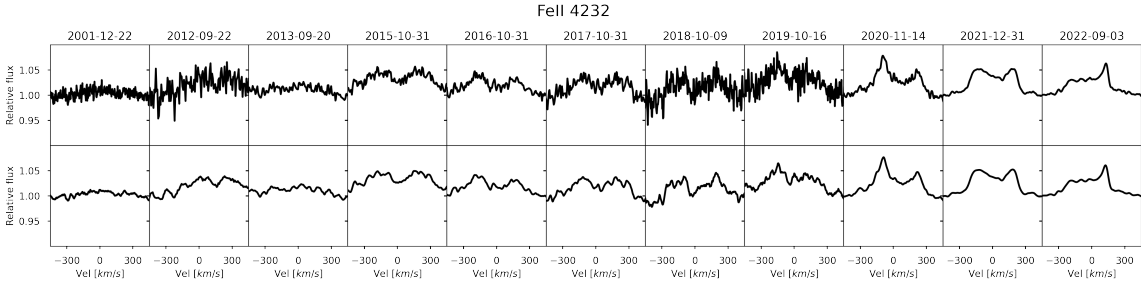

Figure D.12: Evolution of FeII 4233 over the years, Top panel the spectrum without filtering.

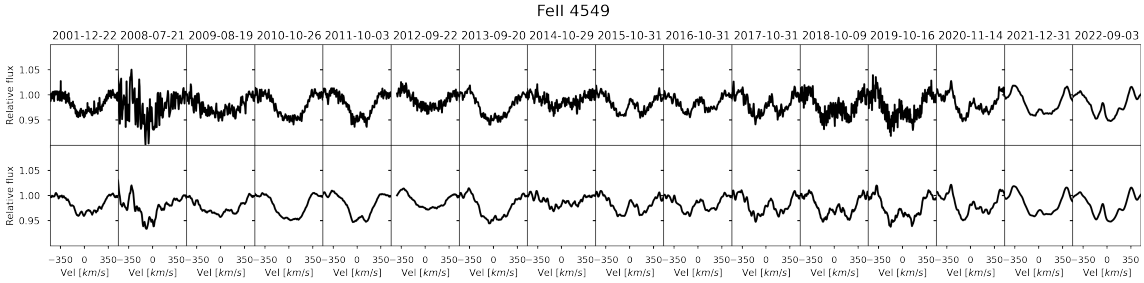

Figure D.13: Evolution of FeII 4549 over the years, Top panel the spectrum without filtering.

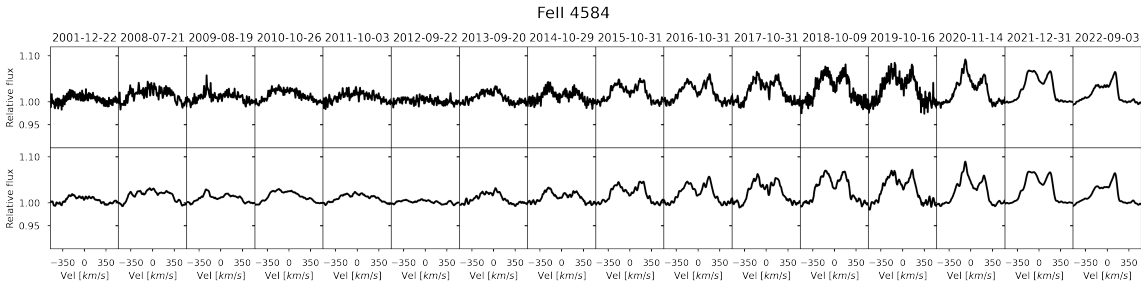

Figure D.14: Evolution of FeII 4584 over the years, Top panel the spectrum without filtering.

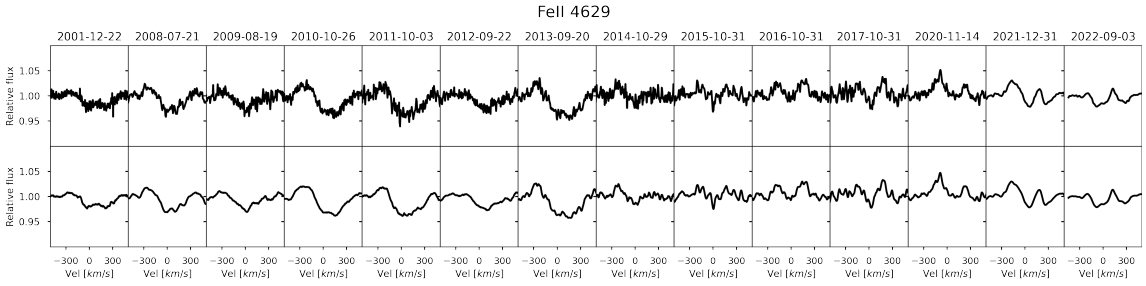

Figure D.15: Evolution of FeII 4629 over the years, Top panel the spectrum without filtering.

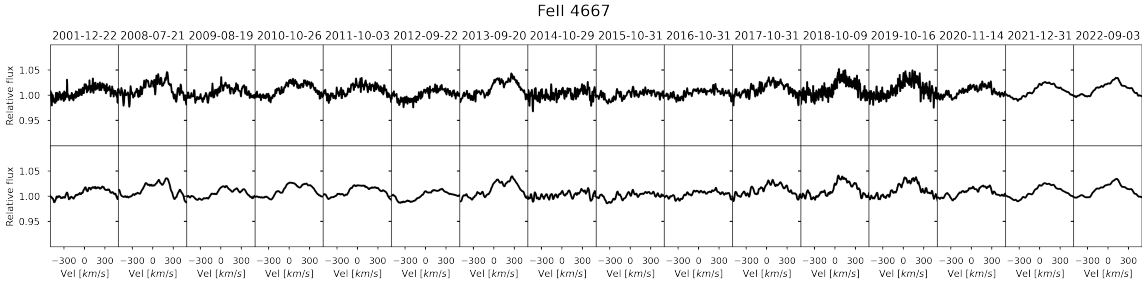

Figure D.16: Evolution of FeII 4667 over the years, Top panel the spectrum without filtering.

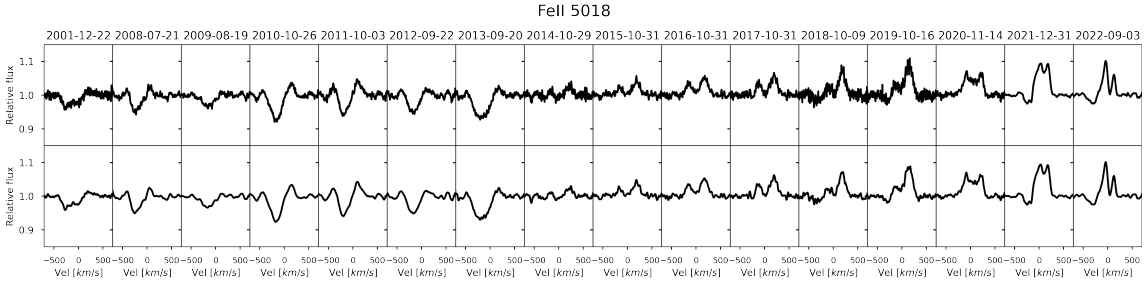

Figure D.17: Evolution of FeII 5018 over the years, Top panel the spectrum without filtering.

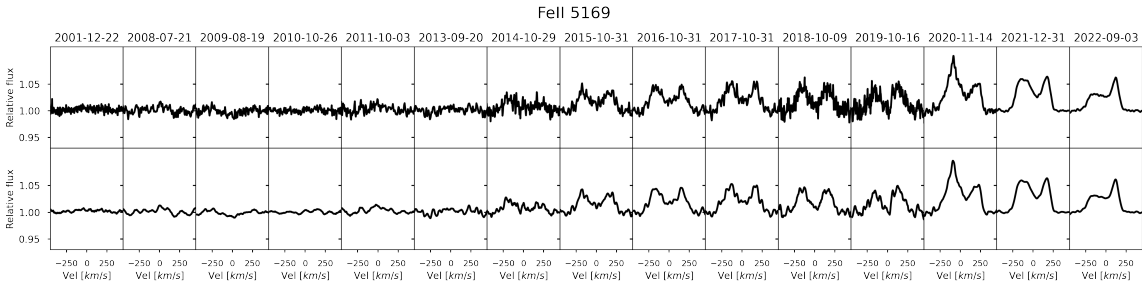

Figure D.18: Evolution of FeII 5169 over the years, Top panel the spectrum without filtering.

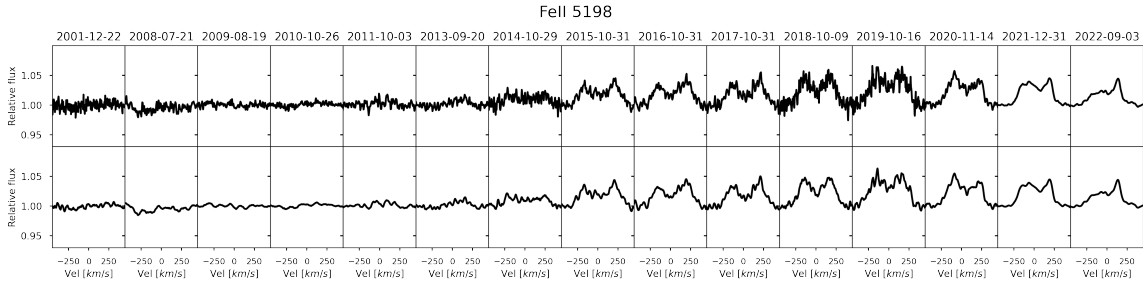

Figure D.19: Evolution of FeII 5198 over the years, Top panel the spectrum without filtering.

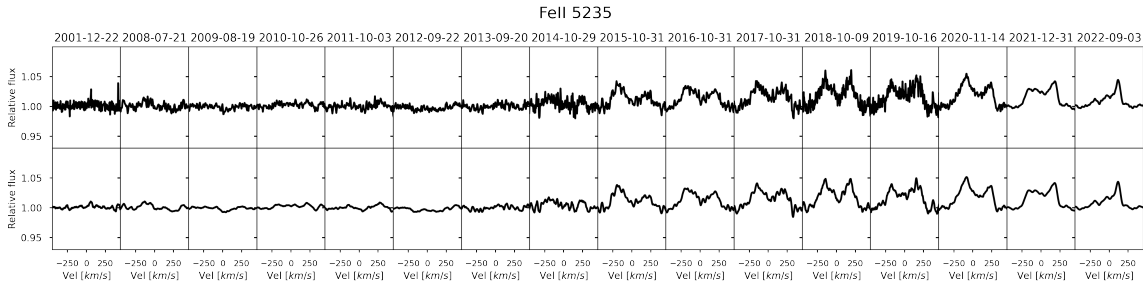

Figure D.20: Evolution of FeII 5235 over the years, Top panel the spectrum without filtering.

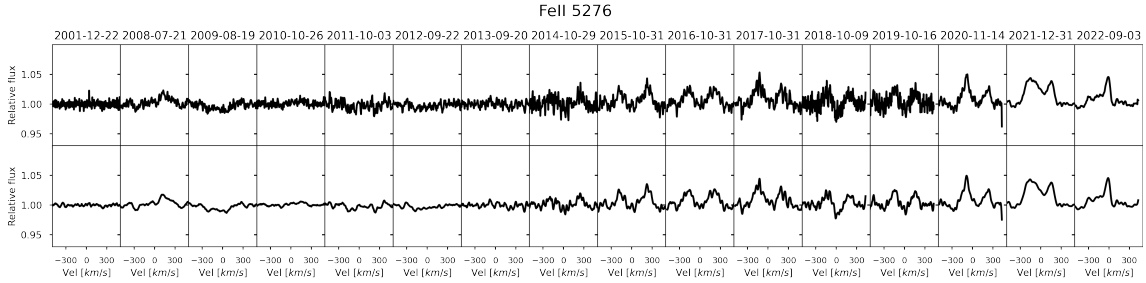

Figure D.21: Evolution of FeII 5276 over the years, Top panel the spectrum without filtering.

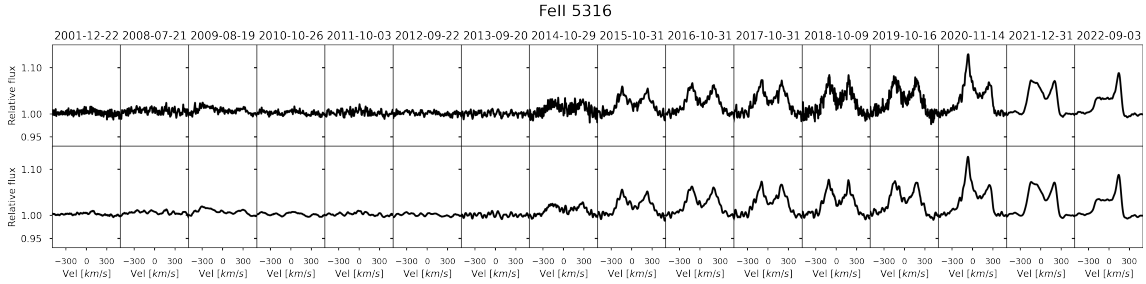

Figure D.22: Evolution of FeII 5316 over the years, Top panel the spectrum without filtering.

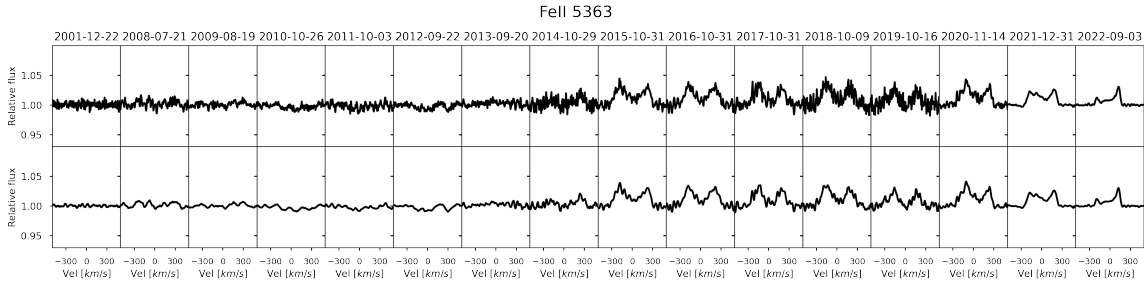

Figure D.23: Evolution of FeIi 5363 over the years, Top panel the spectrum without filtering.

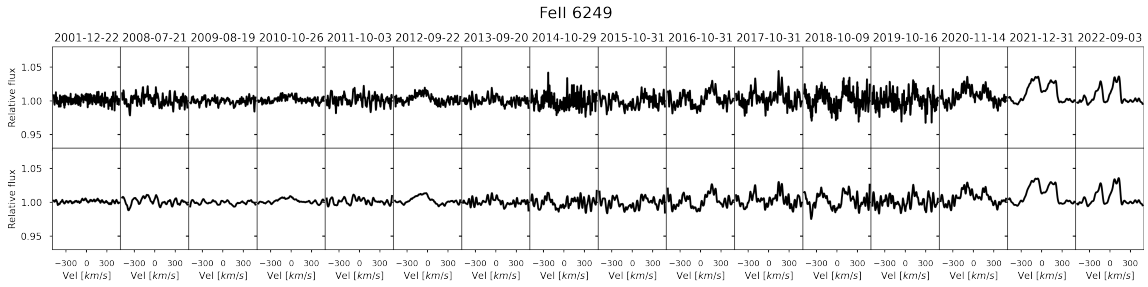

Figure D.24: Evolution of FeII 6249 over the years, Top panel the spectrum without filtering.

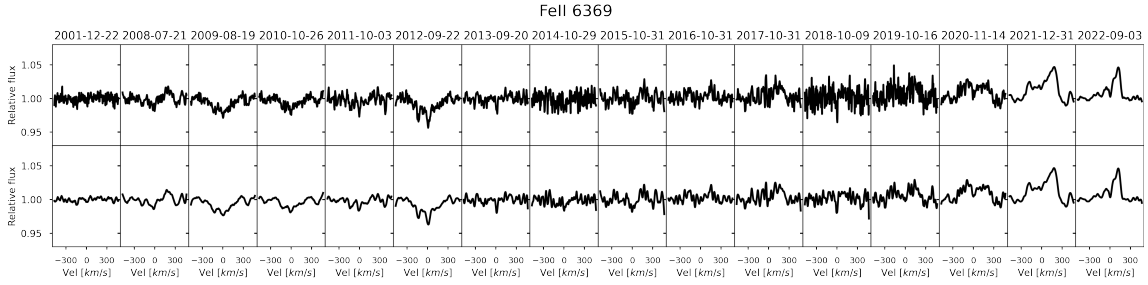

Figure D.25: Evolution of FeII 6369 over the years, Top panel the spectrum without filtering.

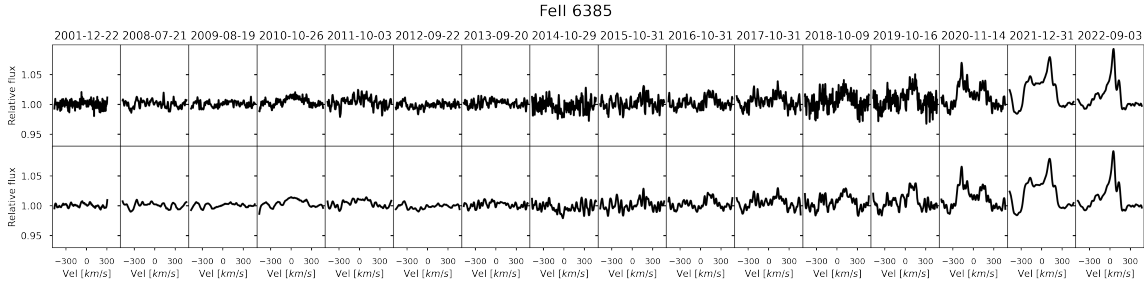

Figure D.26: Evolution of FeII 6385 over the years, Top panel the spectrum without filtering.

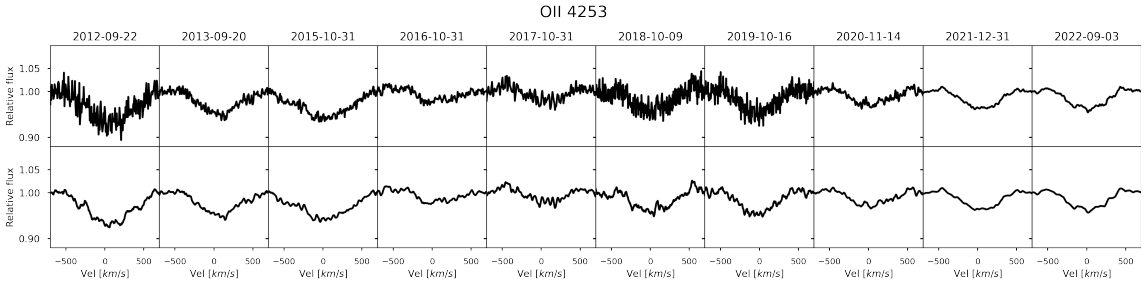

Figure D.27: Evolution of OII 4253 over the years, Top panel the spectrum without filtering.

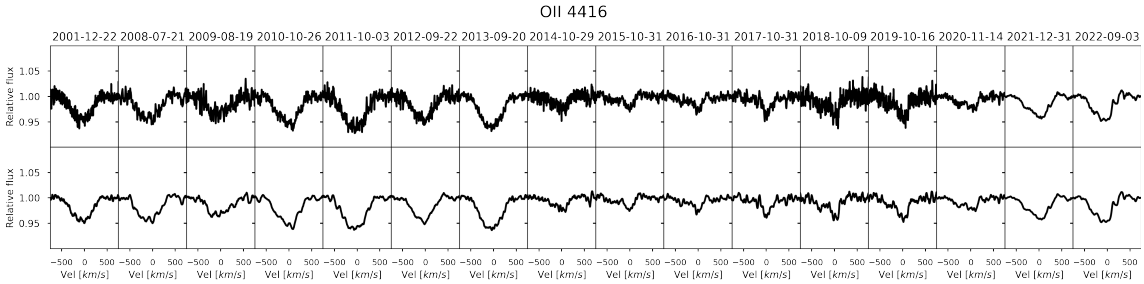

Figure D.28: Evolution of OII 4416 over the years, Top panel the spectrum without filtering.

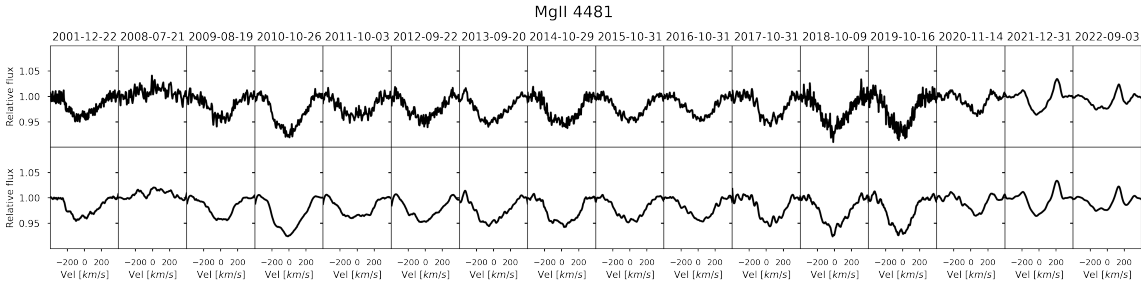

Figure D.29: Evolution of MgII 4481 over the years, Top panel the spectrum without filtering.

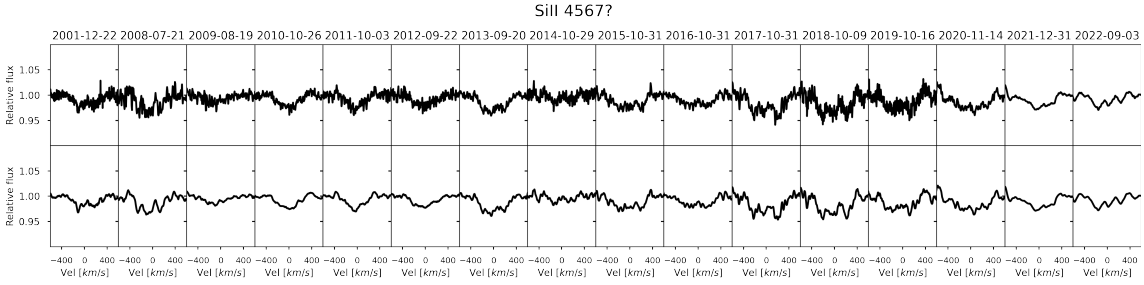

Figure D.30: Evolution of SiII 4567? Over the years, the Top panel has the spectrum without filtering.

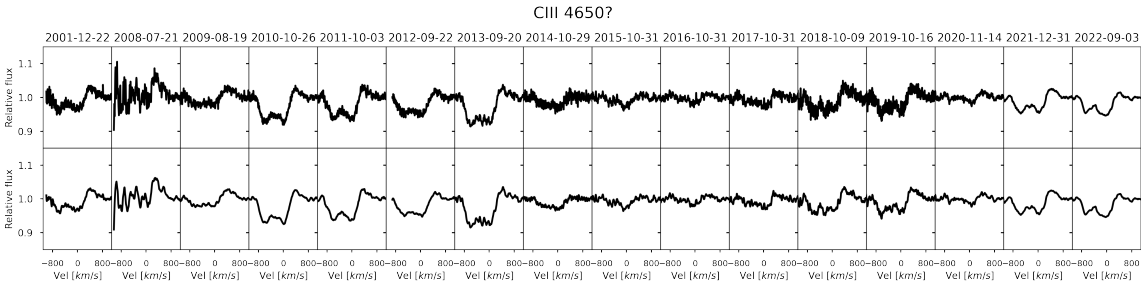

Figure D.31: Evolution of CIII? 4650 over the years, the Top panel of the spectrum without filtering.

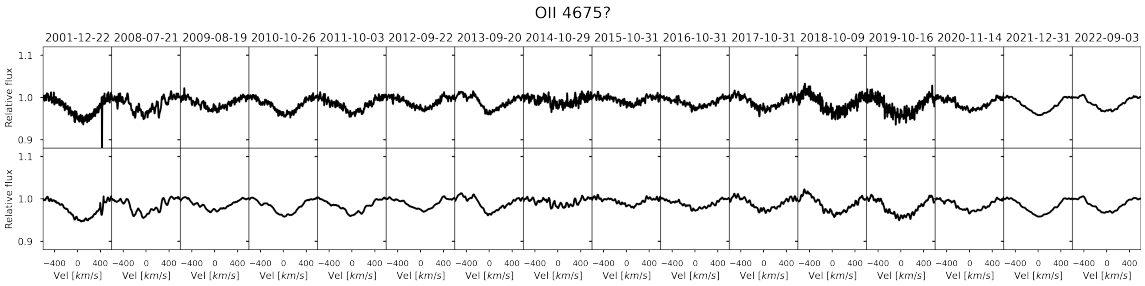

Figure D.32: Evolution of OII 4675 over the years, Top panel the spectrum without filtering.

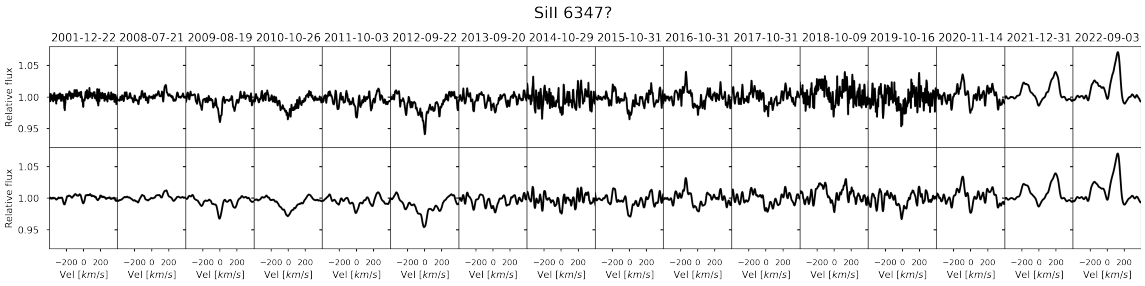

Figure D.33: Evolution of SiII 6347 over the years, Top panel the spectrum without filtering.

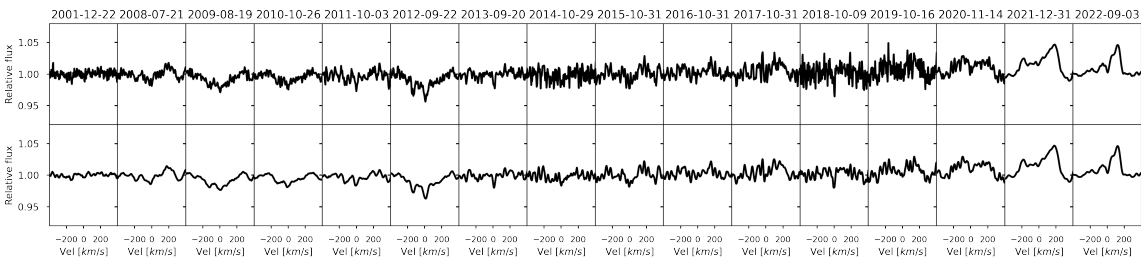

Figure D.34: Evolution of SiII 6371 over the years, Top panel the spectrum without filtering.

Appendix E

Spectral window where EW is calculated

Table E.1: Spectral window where the EW is computed for Balmer lines

Spectral line	Spectral window [km/s]
Hα	–776 to 776
Hβ	-700 to 700
Hγ	-750 to 750
Hδ	-850 to -850

Table E.2: Spectral window where the EW is computed for Iron lines

Spectral line [Å]	Spectral window [km/s]
FeII 4232	-580 to 580
FeII 4549	-480 to 480
FeII 4584	-480 to 480
FeII 4629	-480 to 480
FeII 4667	-500 to 500
FeII 5018	-500 to 500
FeII 5169	-480 to 480
FeII 5198	-480 to 480
FeII 5235	-480 to 480
FeII 5276	-480 to 480
FeII 5326	-650 to 650
FeII 5363	-500 to 500
FeII 6249	-400 to 400
FeII 6369	-400 to 400
FeII 6385	-400 to 400

Table E.3: Spectral window where the EW is computed for Helium lines

Spectral line [Å]	Spectral window [km/s]
HeI 4388	-550 to 550
HeI 4471	-450 to 450
HeI 4713	-330 to 330
HeI 4921	-380 - 380
HeI 5047	-450 to 450
HeI 5875	-450 to 450
HeI 6678	-350 to 350
HeI 7065	-350 to 350

Table E.4: Spectral window where the EW is computed for Other lines

Spectral line [Å]	Spectral window [km/s]
OII 4253	–600 to 600
OII 4416	-600 to 600
MgI 4481	350 to 350
SiII? 4567	-500 to 500
CIII/OII? 4650	-900 to 900
OII 4675	-300 to 300
SiII 6349	-400 to 400

Appendix F

Average values for the parameters obtained on the several spectral lines

	EW [Å]	σ [Å]	RV [km/s]	σ [km/s]	DPS [km/s]	σ [km/s]	V/R	σ
FeII 4232 Å	-0.23	0.11	-0.6	9.6	223	34	1.00	0.02
FeII 4549/SiII 4552 Å	0.27	0.06	-6.1	11.6	-	-	-	-
FeII 4584 Å	-0.28	0.13	-4.5	7.8	323	38	1.00	0.01
FeII 4629 Å	0.03	0.10	-4.2	13.1	340	23	1.03	0.01
FeII 4667 Å	-0.13	0.07	-1.8	10.9	225	27	1.00	0.01
FeII 5018/HeI 5015 Å	-0.07	0.23	-5.3	8.8	336	133	0.98	0.03
FeII 5198 Å	-0.17	0.14	1.2	5.7	309	32	1.00	0.02
FeII 5235 Å	-0.12	0.11	4.1	10.0	336	21	1.00	0.02
FeII 5276 Å	-0.06	0.08	-5.4	11.7	330	39	1.00	0.02
FeII 5316 Å	-0.25	0.19	-6.4	12.1	315	28	1.00	0.03
FeII 5363 Å	-0.09	0.09	1.3	12.8	344	38	1.00	0.01
FeII 6249 Å	-0.05	0.07	-2.7	11.8	242	43	1.00	0.01
FeII 6369/SiII 6371 Å	-0.02	0.11	1.2	6.4	269	131	0.98	0.01
FeII 6385 Å	-0.09	0.12	-0.7	8.7	228	123	1.02	0.04
< Total Average >	-0.09	0.12	-2.1	10.1	294	55	1.00	0.02

Table F.1: Averaged and dispersion values for each measurement on several spectral lines

	EW [Å]	σ [Å]	RV [km/s]	σ [km/s]	DPS [km/s]	σ [km/s]	V/R	σ
HeI 4388 Å	0.46	0.13	-3.6	10.8	746	26	1.02	0.01
HeI 4471 Å	0.54	0.16	1.1	12.6	-	-	-	-
HeI 4713 Å	0.22	0.08	-3.0	9.1	630	27	1.00	0.01
HeI 5015/FeII 5018 Å	-0.07	0.23	-5.3	8.8	336	133	0.98	0.03
HeI 5047 Å	0.19	0.06	1.6	9.7	-	-	-	-
HeI 5875 Å	0.18	0.34	-5.3	8.8	415	45	1.00	0.04
HeI 6678 Å	0.23	0.33	1.2	5.7	393	92	0.98	0.02
HeI 7065 Å	0.04	0.40	4.1	10.0	416	48	0.96	0.08
< Total Average >	0.22	0.22	-1.2	9.4	489	62	0.99	0.03

Table F.2: Averaged and dispersion values for each measurement on several spectral lines

	EW [Å]	σ [Å]	RV [km/s]	σ [km/s]	DPS [km/s]	σ [km/s]	V/R	σ
OII 4253 Å	0.31	0.19	-3.8	10.0	-	-	-	-
OII 4416 Å	0.27	0.12	-2.1	9.8	-	-	-	-
MgI 4481 Å	0.20	0.12	-4.5	11.0	-	-	-	-
SiII 4552/SiII 4549 Å	0.27	0.06	-6.1	11.6	-	-	-	-
SiII $4567^{?}$ Å	0.18	0.07	-5.7	6.6	-	-	-	-
CIII/OII 4650 Å	0.34	0.31	-6.1	7.5	-	-	-	-
OII 4675 Å	0.26	0.09	-4.1	7.1	-	-	-	-
SiII 6349 Å	0.01	0.1	-1.7	3.9	322	72	0.97	0.02
SiII 6371/FeII 6369 Å	-0.02	0.11	1.2	6.4	269	131	0.98	0.01
$<$ Total Average $>$	0.20	0.13	-3.7	8.2	296	102	0.98	0.02

Table F.3: Averaged and dispersion values for each measurement on several spectral lines

Bibliography

Ahmed A., Sigut T. A. A., 2017, MNRAS, 471, 3398

Araya I., Jones C. E., Curé M., Silaj J., Cidale L., Granada A., Jiménez A., 2017, ApJ, 846, 2

Arcos C., Jones C. E., Sigut T. A. A., Kanaan S., Curé M., 2017, ApJ, 842, 48

Arcos C., Kanaan S., Chávez J., Vanzi L., Araya I., Curé M., 2018, MNRAS, 474, 5287

Arias M. L., Zorec J., Cidale L., Ringuelet A. E., Morrell N. I., Ballereau D., 2006, A&A, 460, 821

Augustson K. C., 2020, in Wade G., Alecian E., Bohlender D., Sigut A., eds, Stellar Magnetism: A Workshop in Honour of the Career and Contributions of John D. Landstreet, Vol. 11, p. 105

Baade D. et al., 2016, A&A, 588, A56

Ballereau D., Chauville J., Zorec J., 1995, A&AS, 111, 457

Bastian N. et al., 2017, MNRAS, 465, 4795

Bjorkman J. E., 1997, in De Greve J. P., Blomme R., Hensberge H., eds, Stellar Atmospheres: Theory and Observations, Vol. 497. p. 239

Bjorkman J. E., Carciofi A. C., 2005, in Astronomical Society of the Pacific Conference Series, Vol. 337, Ignace R., Gayley K. G., eds, The Nature and Evolution of Disks Around Hot Stars, p. 75

Bjorkman K. S., Miroshnichenko A. S., McDavid D., Pogrosheva T. M., 2002, ApJ, 573, 812

Carciofi A. C., Bjorkman J. E., 2006, The Astrophysical Journal, 639, 1081

Carciofi A. C., Bjorkman J. E., 2008, ApJ, 684, 1374

Carciofi A. C., Okazaki A. T., Le Bouquin J. B., Štefl S., Rivinius T., Baade D., Bjorkman J. E., Hummel C. A., 2009, A&A, 504, 915

Castor J. I., Abbott D. C., Klein R. I., 1975, ApJ, 195, 157

Chauville J., Zorec J., Ballereau D., Morrell N., Cidale L., Garcia A., 2001, A&A, 378, 861

Chini R., Hoffmeister V. H., Nasseri A., Stahl O., Zinnecker H., 2012, MNRAS, 424, 1925

Claret A., 2000, A&A, 363, 1081

Cochetti Y. R., Arcos C., Kanaan S., Meilland A., Cidale L. S., Curé M., 2019, A&A, 621, A123

Cochetti Y. R., Arias M. L., Cidale L. S., Granada A., Torres A. F., 2022, A&A, 665, A115

Correia Mota B., 2019, Ph.D. thesis, University of Sao Paulo, Institute for Astronomy, Geophysics, and Atmospheric Sciences

Cranmer S. R., 2005, ApJ, 634, 585

Curé M., 2004, ApJ, 614, 929

Curé M., Meneses R., Araya I., Arcos C., Peña G., Machuca N., Rodriguez A., 2022, A&A, 664, A185

Cyr R. P., Jones C. E., Tycner C., 2015, ApJ, 799, 33

de Araujo F. X., 1995, A&A, 298, 179

Domiciano de Souza A. et al., 2014, A&A, 569, A10

Dunstall P. R. et al., 2015, A&A, 580, A93

Efron B., 1979, The Annals of Statistics, 7, 1

Ekström S. et al., 2012, A&A, 537, A146

Ekström S., Meynet G., Maeder A., Barblan F., 2008, A&A, 478, 467

Esa ., 1997, VizieR Online Data Catalog, I/239

Espinosa Lara F., Rieutord M., 2011, A&A, 533, A43

Fabregat J., Reglero V., 1990, MNRAS, 247, 407

Frémat Y., Zorec J., Hubert A. M., Floquet M., 2005, A&A, 440, 305

Friedjung M., Muratorio G., 1987, A&A, 188, 100

Friend D. B., Abbott D. C., 1986, ApJ, 311, 701

Gayley K. G., Ignace R., Owocki S. P., 2001, ApJ, 558, 802

Gehrz R. D., Hackwell J. A., Jones T. W., 1974, ApJ, 191, 675

Georgy C., Ekström S., Granada A., Meynet G., Mowlavi N., Eggenberger P., Maeder A., 2013, A&A, 553, A24

Ghoreyshi M. R., Carciofi A. C., Jones C. E., Faes D. M., Baade D., Rivinius T., 2021, ApJ, 909, 149

Goraya P. S., 1985, MNRAS, 215, 265

Granada A., Ekström S., Georgy C., Krtička J., Owocki S., Meynet G., Maeder A., 2013, A&A, 553, A25

Hanuschik R. W., 1987, A&A, 173, 299

Hanuschik R. W., Hummel W., Sutorius E., Dietle O., Thimm G., 1996, A&AS, 116, 309

Haubois X., Carciofi A. C., Rivinius T., Okazaki A. T., Bjorkman J. E., 2012, ApJ, 756, 156

Hohle M. M., Neuhäuser R., Schutz B. F., 2010, Astronomische Nachrichten, 331, 349

Huang S.-S., 1972, ApJ, 171, 549

Hubeny I., Lanz T., 1995a, ApJ, 439, 875

Hubeny I., Lanz T., 1995b, ApJ, 439, 875

Hummel W., Dachs J., 1992, A&A, 262, L17

Kippenhahn R., Weigert A., 1990, S&T, 80, 504

Klement R. et al., 2019, The Astrophysical Journal, 885, 147, arXiv:1909.12413 [astro-ph]

Klement R. et al., 2017, A&A, 601, A74

Klement R. et al., 2015, A&A, 584, A85

Kurucz R., 1994, Solar abundance model atmospheres for 0, 19

Kurucz R. L., 1979, ApJS, 40, 1

Labadie-Bartz J., Carciofi A. C., de Amorim T. H., Rubio A., Luiz A., Ticiani dos Santos P., Thomson-Paressant K., 2020, arXiv e-prints, arXiv:2010.13905

Labadie-Bartz J., Carciofi A. C., Henrique de Amorim T., Rubio A., Luiz Figueiredo A., Ticiani dos Santos P., Thomson-Paressant K., 2022, AJ, 163, 226

Lee U., Osaki Y., Saio H., 1991, MNRAS, 250, 432

Levenhagen R. S., 2014, ApJ, 797, 29

Lomb N. R., 1976, Ap&SS, 39, 447

Maeder A., 2009, Physics, Formation and Evolution of Rotating Stars

Maeder A., Meynet G., 2000, ARA&A, 38, 143

Marr K. C., Jones C. E., Carciofi A. C., Rubio A. C., Mota B. C., Ghoreyshi M. R., Hatfield D. W., Rímulo L. R., 2021, ApJ, 912, 76

Marr K. C., Jones C. E., Tycner C., Carciofi A. C., Silva A. C. F., 2022, ApJ, 928, 145

McDavid D., 1986, PASP, 98, 572

McLaughlin D. B., 1962, ApJS, 7, 65

McLean I. S., Brown J. C., 1978, A&A, 69, 291

Meilland A., Millour F., Kanaan S., Stee P., Petrov R., Hofmann K. H., Natta A., Perraut K., 2012, A&A, 538, A110

Meilland A. et al., 2007, A&A, 464, 59

Mennickent R. E., Sabogal B., Granada A., Cidale L., 2009, PASP, 121, 125

Nazé Y. et al., 2019, New Astronomy, 73, 101279

Neiner C., 2018, in Di Matteo P., Billebaud F., Herpin F., Lagarde N., Marquette J. B., Robin A., Venot O., eds, SF2A-2018: Proceedings of the Annual meeting of the French Society of Astronomy and Astrophysics, p. Di

Neiner C., de Batz B., Cochard F., Floquet M., Mekkas A., Desnoux V., 2011, AJ, 142, 149

Nikutta A., R., 2021, Time-series analysis of a RR Lyrae star

Nordh H. L., Olofsson S. G., 1974, A&A, 31, 343

Oey M. S., Massey P., 1995, ApJ, 452, 210

Okazaki A. T., 1991a, PASJ, 43, 75

Okazaki A. T., 1991b, PASJ, 43, 75

Okazaki A. T., 1997, A&A, 318, 548

Okazaki A. T., 2001, PASJ, 53, 119

Okazaki A. T., 2007, in Astronomical Society of the Pacific Conference Series, Vol. 361, Okazaki A. T., Owocki S. P., Stefl S., eds, Active OB-Stars: Laboratories for Stellare and Circumstellar Physics, p. 230

Panoglou D., Faes D. M., Carciofi A. C., Okazaki A. T., Baade D., Rivinius T., Borges Fernandes M., 2018, MNRAS, 473, 3039

Papaloizou J. C., Savonije G. J., Henrichs H. F., 1992a, A&A, 265, L45

Papaloizou J. C., Savonije G. J., Henrichs H. F., 1992b, A&A, 265, L45

Peters G. J., Wang L., Gies D. R., Grundstrom E. D., 2016, ApJ, 828, 47

Pollmann E., 2018, Information Bulletin on Variable Stars, 6239, 1

Pols O. R., Cote J., Waters L. B. F. M., Heise J., 1991, A&A, 241, 419

Press W. H., Rybicki G. B., 1989, ApJ, 338, 277

Prinja R. K., 1989, MNRAS, 241, 721

Quirrenbach A. et al., 1997, ApJ, 479, 477

Quirrenbach A., Buscher D. F., Mozurkewich D., Hummel C. A., Armstrong J. T., 1994, A&A, 283, L13

Reig P., Fabregat J., Coe M. J., Roche P., Chakrabarty D., Negueruela I., Steele I., 1997, A&A, 322, 183

Rímulo L. R. et al., 2018, MNRAS, 476, 3555

Rivinius T., Baade D., Štefl S., 2003, A&A, 411, 229

Rivinius T., Carciofi A. C., Martayan C., 2013, A&A Rev., 21, 69

Rubio A. C., 2019, in Thesis semantic scholar

Sana H., 2017, in Eldridge J. J., Bray J. C., McClelland L. A. S., Xiao L., eds, The Lives and Death-Throes of Massive Stars, Vol. 329, p. 110

Savitzky A., Golay M. J. E., 1964, Analytical Chemistry, 36, 1627

Scargle J. D., 1982, ApJ, 263, 835

Schaerer D., Charbonnel C., Meynet G., Maeder A., Schaller G., 1993, A&AS, 102, 339

Secchi A., 1866, Astronomische Nachrichten, 68, 63

Shakura N. I., Sunyaev R. A., 1973, A&A, 24, 337

Shapley H., Curtis H. D., 1921, Bulletin of the National Research Council, 2, 171

Sigut T. A. A., 2011, in Neiner C., Wade G., Meynet G., Peters G., eds, Active OB Stars: Structure, Evolution, Mass Loss, and Critical Limits, Vol. 272, p. 426

Sigut T. A. A., Jones C. E., 2007, ApJ, 668, 481

Silaj J., Jones C. E., Tycner C., Sigut T. A. A., Smith A. D., 2010, ApJS, 187, 228

Snow J., T. P., 1981, ApJ, 251, 139

Suffak M. W., Jones C. E., Tycner C., Henry G. W., Carciofi A. C., Mota B. C., Rubio A. C., 2020, ApJ, 890, 86

Theodossiou E., 1985, MNRAS, 214, 327

Trypsteen M. F. M., Walker R., 2017, Spectroscopy for amateur astronomers: recording, processing, analysis and interpretation

Underhill A. B., Divan L., Prevot-Burnichon M. L., Doazan V., 1979, MNRAS, 189, 601

Urquhart J. S., Figura C. C., Moore T. J. T., Hoare M. G., Lumsden S. L., Mottram J. C., Thompson M. A., Oudmaijer R. D., 2014, MNRAS, 437, 1791

van Bever J., Vanbeveren D., 1997, A&A, 322, 116

van Leeuwen F., 2007, A&A, 474, 653

Vanzi L. et al., 2012, Monthly Notices of the Royal Astronomical Society, 424, 2770

Vieira R. G., Carciofi A. C., Bjorkman J. E., Rivinius T., Baade D., Rímulo L. R., 2017, MNRAS, 464, 3071

Vink J. S., 2000, Ph.D. thesis, University of Utrecht, Netherlands

Vio R., Diaz-Trigo M., Andreani P., 2013, Astronomy and Computing, 1, 5

Vollmann K., Eversberg T., 2006, Astronomische Nachrichten, 327, 862

von Zeipel H., 1924, MNRAS, 84, 665

Wade G. A. et al., 2009, in Strassmeier K. G., Kosovichev A. G., Beckman J. E., eds, Cosmic Magnetic Fields: From Planets, to Stars and Galaxies, Vol. 259, p. 333

Wade G. A., Grunhut J. H., MiMeS Collaboration , 2012, in Astronomical Society of the Pacific Conference Series, Vol. 464, Carciofi A. C., Rivinius T., eds, Circumstellar Dynamics at High Resolution, p. 405

Waters L. B. F. M., Cote J., Lamers H. J. G. L. M., 1987, A&A, 185, 206

Wisniewski J. P., Bjorkman K. S., 2006, ApJ, 652, 458

Wood K., Bjorkman K. S., Bjorkman J. E., 1997, ApJ, 477, 926

Yudin R. V., Hubrig S., Pogodin M. A., Schoeller M., 2011, in Neiner C., Wade G., Meynet G., Peters G., eds, Active OB Stars: Structure, Evolution, Mass Loss, and Critical Limits, Vol. 272, p. 222

Zharikov S. V. et al., 2013, A&A, 560, A30

Zorec J., Briot D., 1991, A&A, 245, 150

Zorec J., Briot D., 1997a, A&A, 318, 443

Zorec J., Briot D., 1997b, A&A, 318, 443

Zorec J. et al., 2016, A&A, 595, A132